UNIVERSIDAD DEL PAÍS VASCO
EUSKAL HERRIKO UNIBERTSITATEA

Design and Topological Characterization of 2D Photonic Crystals

Author:
María BLANCO DE PAZ

Supervisors:
Dr. Aitzol GARCÍA-ETXARRI
Dr. Dario BERCIOUX

Doctoral program in
Physics of Nanostructures and Advanced Materials.

(2021)

"Don't let anyone rob you of your imagination, your creativity, or your curiosity. It's your place in the world; it's your life. Go on and do all you can with it, and make it the life you want to live."

Mae Jemison

UNIVERSIDAD DEL PAÍS VASCO
EUSKAL HERRIKO UNIBERTSITATEA

Abstract

Design and Topological Characterization of 2D Photonic Crystals

by María BLANCO DE PAZ

This thesis provides a complete guide for the topological characterization of 2D photonic crystals. It gives a general description of topological materials and applies most of the concepts used in condense matter physics to bosonic systems. Therefore, the methodology described in the thesis can be extended or adapted to any non-interacting periodic system. Besides, the thesis presents several examples of 2D photonic crystals with different topological characters, analyzing the main features of their topological invariant quantities.Finally, the thesis includes several design examples of 2D photonic crystals with different topological properties based on adiabatic transformations. In particular the thesis includes design examples for lattices with obstructed atomic limit (OAL) character and the first 2D photonic crystal model which posses fragile topology.

UNIVERSIDAD DEL PAÍS VASCO
EUSKAL HERRIKO UNIBERTSITATEA

Resumen

Diseño y Caracterización de Cristales Fotónicos Bidimensionales.

por María BLANCO DE PAZ

La historia de la humanidad puede clasificarse en épocas en función de la principal tecnología material desarrollada en cada período. Así, solemos referirnos a diferentes épocas humanas como la edad de piedra, la edad de bronce o la edad de hierro. Nuestra época está dominada por las tecnologías basadas en el silicio y, por lo tanto, podríamos referirnos a esta era como la *edad del silicio*.

Desde el punto de vista de una física (o un físico), la era del silicio comenzó con el descubrimiento de los semiconductores. Estos materiales se conocían desde finales del siglo XIX. Sin embargo, la explicación de su extraño comportamiento conductor en términos de ideas de llenado de bandas no se introdujo hasta principios de la década de 1930. Por aquel entonces, las bandas electrónicas eran un concepto bien conocido, pero los mecanismos físicos que rigen la conducción de electrones en los semiconductores aún no se comprendían del todo. Alrededor de 1930, Alan Wilson propuso la siguiente explicación: si la banda de valencia está completamente llena, los electrones de un material sólo pueden conducir la electricidad si son excitados a otra banda a través de la brecha de energía. Sin embargo, si la banda de valencia no está llena, los electrones pueden dispersarse a estados cercanos y conducir así la electricidad. Wilson y sus contemporáneos ya sabían que la separación entre bandas estaba controlada por las impurezas dentro del cristal, impulsando así el desarrollo de técnicas para purificar y controlar la concentración de dopantes en los semiconductores de silicio y germanio [1, 2]. En la física moderna, la caracterización de un material se basa en los conceptos de simetría y cantidades conservadas. La clasificación de las diferentes fases de la materia en términos de simetrías y su ruptura se conoce comúnmente como el paradigma de Landau [3–5]. Aunque proporciona un marco exitoso para describir las transiciones de fase, tanto a nivel clásico como cuántico,

no logra captar algunos fenómenos novedosos en la física del estado sólido: las fases topológicas. La razón es que la conductividad de los materiales topológicos no depende de la simetría local, sino de otras propiedades no locales denominadas invariantes topológicas. Como estas propiedades no pueden definirse localmente, los fenómenos topológicos sólo pueden captarse considerando el conjunto de modos en las bandas de energía de un material. La principal implicación de este carácter no local de los efectos topológicos es que las impurezas o los defectos locales no les afectan. Por lo tanto, estos prometedores materiales presentan propiedades poco convencionales y robustas que pueden dar lugar a una nueva revolución en la tecnología de materiales, abriendo la puerta a la *edad topológica*.

El concepto de invariante topológico procede del área de topología dentro de las matemáticas, que se enfoca en el estudio de las propiedades que se conservan bajo deformaciones continuas [6]. El ejemplo más conocido para ilustrar este concepto consiste en clasificar geometrías como la esfera y el donut a través de su "género" g. Esta propiedad, cuenta el número de agujeros de un objeto: la esfera tiene $g = 0$ y el donut tiene $g = 1$. Como no es posible deformar una en otra, el "género" es un invariante topológico. Esta cantidad, al igual que otros invariantes topológicos, suelen ser números enteros que, por definición, no pueden cambiar continuamente, lo que implica que las propiedades físicas topológicamente invariantes serían robustas frente a perturbaciones locales.

La primera manifestación física de la topología fue el efecto Hall cuántico (QHE) descubierto por Klaus von Klitzing en gases de electrones bidimensionales bajo un fuerte campo magnético [7]. En 1985, von Klitzing recibió el Premio Nobel de física por demostrar la cuantificación y la excepcional robustez de la conductividad de Hall en estos sistemas. En 1982, Thouless *et al.* [8] propuso la primera caracterización topológica de este comportamiento en términos de un invariante topológico conocido como el número Chern, que está directamente relacionado con la conductividad de Hall. Esta contribución al campo de los materiales topológicos fue reconocida con el Premio Nobel de física en 2016.

Aunque la mayoría de los conceptos clave de la topología de sistemas de bandas se desarrollaron originalmente en física de la materia condensada, muchos de ellos se aplicaron rápidamente a la propagación de ondas electromagnéticas en cristales fotónicos [9]. Dado que la mayoría de las magnitudes fundamentales en el campo de los materiales topológicos, como la fase de

Berry, la curvatura de Berry y el espectro del operador *Wilson loop*, se basan en la propagación de ondas a través de un potencial periódico, la mayoría de las características topológicas pueden trasladarse a la propagación de ondas en sistemas periódicos clásicos [10].

El primer capítulo introductorio de esta tesis, explica como comenzó el estudio de los efectos topológicos tanto en sistemas electrónicos como bosónicos. Incluyendo también los ejemplos más relevantes de fases topológicas, enfatizando en sistemas clásicos, ya que esta tesis se centra en la realización y análisis de aislantes topológicos en cristales fotónicos bidimensionales. Esto significa que consideramos sistemas en los que la constante dieléctrica es periódica a lo largo de dos direcciones espaciales, y la constante de red es comparable al orden de la longitud de onda incidente. Dicha periodicidad del sistema limita la frecuencia a la que se propagan las ondas de luz, al igual que los electrones en física de la materia condensada [11]. Por lo tanto, los modos del sistema pueden ser descritos con la estructura fotónica de bandas — de manera similar a la estructura de bandas electrónica [12]. En el capítulo 2 se incluye la descripción teórica de la propagación de la luz en un cristal fotónico a partir de las ecuaciones macroscópicas de Maxwell, así como los supuestos necesarios para obtener un problema periódico de valores propios formalmente comparable a la ecuación de Schrödinger.

Además, en los capítulos 2 y 3 de esta tesis se incluye la descripción teórica de los conceptos fundamentales en el campo de los materiales topológicos, revisando las expresiones utilizadas para definir invariantes topológicos en sistemas periódicos bidimensionales. Dichas cantidades topológicamente invariantes son la curvatura, la fase y la conexión de Berry, así como el número Chern y el número Chern de valle. También se explica el procedimiento para obtener los valores propios del operador *Wilson loop* y su relación con la posición de las funciones de Wannier en la celda unidad del cristal. Todas estas expresiones en el límite continuo son explicadas en el capítulo 2. Mientras que la discretización de dichas cantidades en el espacio recíproco se muestran en el capítulo 3, proporcionando un enfoque práctico para aplicar dichos conceptos teóricos a la clasificación topológica de cristales fotónicos.

Para la caracterización completa de dichos cristales, también se presenta en el capítulo 2 una descripción básica de la teoría de *Topological Quantum Chemistry* (TQC), basada en la relación entre la simetría de los modos propios del sistema y la de las funciones de Wannier, obteniendo información sobre la posición de estas funciones en la celda unidad. Además, en el capítulo 3

se incluye una descripción práctica detallada sobre cómo aplicar TQC en la respuesta óptica de los cristales fotónicos para obtener la topología de cada estructura de bandas.

Como se explica a lo largo de esta tesis, la forma y posición de las funciones de Wannier en la celda unidad real están estrechamente relacionadas con el carácter topológico del cristal. La posición predicha por TQC de las funciones de Wannier exponencialmente localizadas, son comparadas con la localización de los máximos de densidad local de estados, integrada sobre grupos de bandas aisladas.

Por tanto, la tesis incluye la descripción del cálculo de la densidad de estados y la densidad local de estados en cristales fotónicos, cuyo formalismo matemático empieza en el límite continuo explicado en el capítulo 2, y acaba proporcionando una guía paso a paso para calcular numéricamente dichas magnitudes en el capítulo 3.

Mientras los capítulos 2 y 3 están dedicados a la descripción teórica y a la metodología utilizada, respectivamente. Los capítulos de resultados se centran en la implementación práctica de dicha meodología para la caracterización topológica de cristales fotónicos bidimensionales.

En el capítulo 4 de esta tesis se presentan varios ejemplos de fases con diferente topología, incluyendo una caracterización detallada de las características distintivas de cada una de las diferentes fases. Concretamente, se presenta el análisis para un aislante topológico de tipo Chern, un sistema con grado de libertad de valle, un sistema de límite atómico obstruido (OAL) y un sistema que alberga bandas con topología frágil. Aunque la fase frágil y el OAL se introducen por primera vez en el capítulo 4, ambas fases se explican en profundidad en los capítulos sucesivos.

En el capítulo 5 de esta tesis se presenta el primer caso conocido de un cristal fotónico con bandas topologicamente frágiles. Además, se explica cómo se puede diseñar un cristal fotónico con topología frágil. En este capítulo se hace especial hincapié en cómo se puede aplicar TQC a cristales fotónicos. Comenzando por la descripción del grupo de simetría de las redes hexagonales bidimensionales ($p6mm$), se detallan los pasos necesarios para realizar una evaluación topológica mediante TQC. Además, esta caracterización se combina con el análisis espectral del operador *Wilson loop*. Para explorar la

manifestación topológica de las bandas frágiles en un sistema finito, se emulan las propiedades de los modos finitos mediante la construción de una supercelda que combina sistemas fotónicos triviales y frágiles a lo largo de una dirección.

Por último, el capítulo 6 está dedicado a explorar la relación entre la concentración de carga en el espacio real, calculada mediante la densidad de estados local para conjuntos de bandas conectadas, y la posición de las funciones de Wannier exponencialmente localizadas predichas por TQC en diferentes redes hexagonales. Además, el análisis se complementa con los espectros del operador *Wilson loop*. En este capítulo, se explica en profundidad la naturaleza de la fase OAL y por qué puede confundirse fácilmente con una fase topológica $\mathbb{Z}_2$.

En general, esta tesis introduce una forma sistemática de caracterizar la topología de los cristales fotónicos bidimensionales, que puede ser extendida a otras redes bosónicas bidimensionales. Contiene estrategias prácticas para calcular invariantes topológicos como el número Chern, el número Chern de valle y los valores propios del operador *Wilson loop*. Además, se introduce por primera vez la aplicación de TQC a cristales fotónicos mostrando su utilidad para una eficiente caracterización topológica de las estructuras de bandas fotónicas.Finalmente, se muestra la correspondencia entre la distribución de densidad local de estados de conjuntos de bandas conectadas y la posición de los centros de Wannier predichos por TQC y los espectros del operador *Wilson loop*. Todos estos instrumentos permiten analizar en profundidad el carácter topológico de las estructuras fotónicas. El conjunto de estas herramientas ha permitido diseñar la primera implementación física conocida hasta la fecha de un sistema con topología frágil.

Acknowledgements

Now that this journey is ending, I would like to start by expressing my sincere gratitude to the first person who received me at the DIPC, Dr. Juan José Saenz (Mole). I consider myself lucky for having the opportunity to learn so many things from him, who was one of my "non-official" advisors, an extraordinary scientist and most importantly, an extraordinary person. Sin ninguna duda, para mí eres un ejemplo a seguir, alguien a quién siempre recordaré y estaré profundamente agradecida. ¡Gracias Mole!

Of course, this thesis would not have been possible without my two official PhD advisors, Dr. Aitzol García Etxarri and Dr. Dario Bercioux. I would like to acknowledge them for their continuous support, patience, motivation, and immense knowledge that they shared with me. Their guidance helped me in all the time of research and writing of this thesis. I could not have imagined having better advisors and mentors for my PhD. Mila esker denagatik Aitzol! Grazie mille per tutto Dario! Besides my official advisors, I would like to thank my second "non-official" advisor Dr. Geza Giedke for his encouragement, his insightful discussions and his hard questions which motivated me to widen my research.

Also, I would like to thank Dr. Paloma Arroyo Huidobro who directed my international stay, held virtually due to the COVID-19 pandemic. I have learned so many things working with you (academic and not) and I will always be thankful to you for your patience, support and motivation. I want to extend my gratitude to Dr. Matthew Proctor who always helped me, not only with his codes but with his kind explanations as well.

One of the most important things in science is being able to feel comfortable working with other people. In my case, I feel lucky to have ended up collaborating with such amazing people. So I want to thank Dr. Maia G. Vergniory, Dr. Barry Bradlyn, Dr. Hadiseh Alaein and Dr. Alejandro González Tudela for their insightful help, suggestions, comments and overall nice discussions. Also, I would like to thank my university tutor Dr. Nerea Zabala for your kind help and guidance during these years. Apart, I want to acknowledge Dr. Giandomenico Palumbo and Dr. Barry Bradlyn for helping me as international experts and last, but not least, I want to specially thank my thesis committee Dr. Juan Luis Mañes, Dr. Fernando de Juan and Dr. Maia G. Vergniory.

Next, I want thank the DIPC and all the people that helped me -in some way- during my stay. From helping out with bureaucratic paperwork to having some personal talk in a bad day, there was always someone. Pursuing a PhD is not always an easy journey. Specially, as a women, I would like to thank the DIPC for their efforts in equality, being an inclusive and safe place for all. I want to thank the direction, administrative and outreach personal, as well as the (sometimes forgotten) wonderful people who work in maintenance, security and cleaning services. ¡Muchas gracias por vuestro trabajo y apoyo durante todos estos años! I also want to thank all the people that works in the computer services from the DIPC, for their help and kindness (even when I collapsed the system). ¡Gracias!

After spending more than four years in a place, you get to meet a lot (I mean A LOT) of people. Although it doesn't necessarily means that you have a strong relationship with all of them, as some of them come as they go, all the moments that we shared are not meaningless to me. So, I want to take this space to thank everyone who played even the smallest role in my journey. I will of course not be able to name you all (specially with my memory for the names), but all of you were very important during these years. The people of my group, people of theoretical chemistry, DIPC and CFM students, and all the people that I shared a coffee with or just a conversation, thank you for being part of my journey! Especialmente, gracias a todos mis compis más cercanos por todos los momentos y risas compartidas.

No puedo olvidar dar las gracias a aquellos que siempre han estado acompañándome en estos años con pandemia incluida (como mi bro El Dani al que prometí nombrar). Gracias por haber estado siempre tan presentes (a veces cerca y otras no tanto) durante estos años (e igual hasta muchos más antes), ¡gracias por ser parte de mi vida! Al igual que mi familia, que aún en la distancia siempre han estado ahí. Especialmente gracias a mi tía y a la Sa por siempre haber creído en mí y apoyarme incondicionalmente. Y a mis padres, creo que no hay palabras suficientes que expresen mi agradecimiento hacia ellos. Simplemente, sin ellos no sería la persona que soy hoy. Gracias por todo lo que hacéis por mí, y aunque suene un poco *cliché*, sois los mejores padres que alguien pudiera tener. Por último, me gustaría agradecer a la persona más importante que he conocido en esta aventura, Alejandro o Dr. Pena, que poco a poco se convirtió en mi persona favorita, en mi mejor amigo, mi compañero, mi socio, mi cómplice, alguien que siempre está incondicionalmente. ¡Grasias pieza de puzzle picuda!

Contents

List of Figures

List of Tables

List of Abbreviations

1D	One-**D**imensional
2D	Two-**D**imensional
BR	**B**and **R**epresentation
EBR	**E**lementary **B**and **R**epresentation
irrep	***Irrep***: **Irr**educible **Rep**resentation
BZ	(1st) **B**rillouin **Z**one
YIG	**Y**ttrium-**I**ron-**G**garnet
BCS	**B**ilbao **C**rystallographic **S**erver
DOS	**D**ensity **O**f **S**tates
EM	**E**lectro-**M**agnetic
LDOS	**L**ocal **D**ensity **O**f **S**tates
MPB	**M**IT **P**hotonic **B**ands
SSH	**S**u-**S**chrieffer–**H**eeger
OAL	**O**bstructed **A**tomic **L**imit
PhC	**Ph**otonic **C**rystal
TE	**T**ransverse **E**lectric
TM	**T**ransverse **M**agnetic
TMD	**T**ransition **M**etal **D**ichalcogenideime
TQC	**T**opological **Q**uantum **C**hemistry
TRS	**T**ime-**R**eversal **S**ymmetry
UC	**U**nit **C**ell
QHE	**Q**uantum **H**all **E**ffect
QSHE	**Q**uantum **S**pin **H**all **E**ffect

To Tara...

1 Introduction

1.1 Introduction to topology

Human history can be categorized into eras depending on the leading material technology developed at each period. Thus, we commonly refer to different human epochs as the stone age, the bronze age or the iron age. Our times are dominated by Silicon-based technologies, and thus, we could refer to this era as the *silicon age*. From the point of view of a physicist, the silicon age started with the discovery of semiconductors. These materials were known since the late 1800s. Nevertheless, an explanation to their strange conductive behaviour in terms of band filling ideas was not introduced until the early 1930s. Back then electronic bands were a well known concept, but the physical mechanisms governing electron conduction in semiconductors were not yet fully understood. Around 1930 Alan Wilson proposed the following explanation: if the valance band is fully filled, electrons in a gapped material can only conduct electricity if they are excited to another band across the energy band-gap. Nevertheless, if the valence band is not filled, electrons can be scattered to nearby states and thus conduct electricity. Wilson and his contemporaries already knew that band gaps were controlled by impurities within the crystal and this idea boosted the development of techniques to purify and control the concentration of dopants in silicon and germanium semiconductors [1, 2].

In modern physics, the characterization of a material is based on the concepts of symmetry and conserved quantities. The classification of the different phases of matter in terms of symmetries and their breaking is commonly known as the Landau paradigm [3–5]. Although this structure provides a successful framework for describing phase transitions —classical and quantum— it fails to capture some novel phenomena in solid-state physics: topological phases. The reason behind this is that the conductivity of topological materials does not depend on local symmetry, but on some other non-local

properties called topological invariants. Since these properties cannot be locally defined, topological phenomena can only be captured by considering the entire set of modes in the energy bands of a material. The main implication of this non-local character of topological effects is that impurities or local defects will not affect them. Therefore, these promising materials present unconventional and robust properties which may give rise to a new revolution in material technologies opening the door to the era of topology.

The concept of topological invariant comes from the mathematical area of topology, which studies properties that are conserved under continuous deformations [6]. The most typical example to illustrate this concept consists in classifying geometries such as a sphere and doughnut through their genus g. This property, counts the number of holes in an object: the sphere has $g = 0$ and the doughnut has $g = 1$. Since it is no possible to smoothly deform one into another, the genus is a topological invariant. The genus of geometry is mathematically formalized through the Gauss–Bonnet theorem. This theorem states that the surface integral of the Gaussian curvature of a closed geometry (K) is quantized. The associated topological invariant can be calculated for two-dimensional surfaces through the Euler characteristic χ, defined as

$$\chi = \frac{1}{2\pi} \iint_S K \mathrm{d}A \tag{1.1}$$

where S is a closed surface. This quantity is an integer related to the genus as $\chi = 2 - 2g$. For example, the Gaussian curvature of a spherical object of radius R is $K = 1/R^2$. Since the curvature is constant, the integral over its area $A = 4\pi R^2$ gives $\chi = 2$ which is consistent with $g = 0$, an object with no holes. This quantity is conserved if the sphere is deformed by flattering some parts of the surface and curving other parts. This is an important implication of the Gauss–Bonnet theorem to define topological invariant quantities. The Euler characteristic and the genus are usually integer numbers that, by definition, cannot change continuously implying that the physical properties topologically invariants would be robust to local perturbations.

1.1.1 Topology in condense matter

The first physical manifestation of topology was the quantum Hall effect (QHE) discovered by Klaus von Klitzing in two-dimensional (2D) electron gases under a strong magnetic field [7]. In 1985, von Klitzing received the Nobel Prize for showing the quantization and exceptional robustness of the

Hall conductance in these systems. In 1982, Thouless *et al.* [8] proposed the first topological characterization of this behaviour in terms of a topological invariant C_n, also known as the Chern number.[1] They determined the relation between this number and the Hall conductance σ_{xy} which can be expressed as,

$$\sigma_{xy} = -\frac{e^2}{h}\sum_n C_n. \tag{1.2}$$

The conductance increases with a quantized behaviour as the magnetic field is increased and consequently, more edge states occur on the 2D electron gas. Semi-classically,the electrons of the gas subjected to a perpendicular magnetic field undergo a cyclotron motion. At the interface with an insulating material, the electron motion is restricted resulting in chiral edge states. Since there are no available states to backscatter to, the electrons cannot travel along the interface in the opposite direction which results in robust chiral states. Equation 1.2 exemplifies the so-known *bulk-boundary correspondence*, where the Chern number (a topological invariant of the bulk), is related to the number of boundary modes. The QHE is the most common example of a topological phenomenon presenting an insulating bulk, while sustaining surface states topologically protected against disorder. This contribution of Thouless *et al.* to the field of topological materials was recognized with the Nobel Prize in 2016. An illustrative representation of how chiral edge states emerge due to the QHE is shown in Fig. 1.1.

There exits several models which describe the topological behaviour of Chern insulators [13, 14], nevertheless, the most relevant is the Haldane model [15]. Haldane highlighted for the first time that the key ingredient is not the applied magnetic field, but the breaking of the time-reversal symmetry (TRS). For example, the energy spectrum of a honeycomb lattice along its irreducible Brillouin zone (BZ) presents Dirac cones at the high symmetry points $\mathbf{K}$ and $\mathbf{K}'$ due to the crystalline symmetry. Although the Dirac cones can be gaped breaking either TRS or inversion symmetry, Haldane showed that the topological modes only emerge with broken TRS. In the recent years, the question was whether non-trivial topology can be found in systems preserving TRS.

In a new class of topological insulators systems, there is an effect reminiscent of the Haldane model [15] is known as the quantum spin-Hall effect (QSHE) [16, 17]. In an electronic system which preserves TRS, the Kramer's theorem imposes that for each state at energy $E(k)$, there will always be a

[1] The detail formulation of the Chern number is explained in Chapter 2.

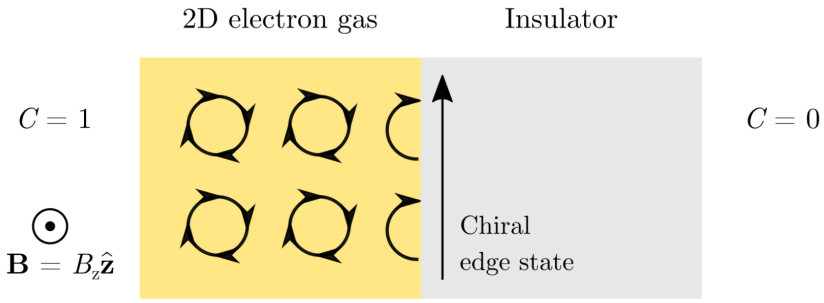

FIGURE 1.1: Quantum Hall effect in a two-dimensional electron gas: the first realization of a protected topological phase. Electrons follow a semiclassical cyclotron motion under a perpendicular magnetic field $\mathbf{B} = B_z\hat{\mathbf{z}}$. At the interface between the 2D electron gas under the magnetic field (with Chern number $C = 1$) and an insulator ($C = 0$), a chiral edge state emerges. Since there is no available state to backscatter, the eletrons are force to describe unidirectional propagation along the interface which is protected against defects. Figure adapted from Ref. [13].

state at $E(-k)$ with opposite momentum and spin. This implies that spin up and spin down modes are degenerate. The degeneracy is extended over the whole BZ when spin-orbit interactions (SOI) are neglected. As a consequence of SOI, the spin modes preserve the degeneracy only at high symmetry points in the BZ [16, 17]. Within this framework, the edge modes that emerge in a band gap can cross an even or odd number of times. The modes that cross an even number of times are topologically trivial since they can be adiabatically removed from the gap. While if they cross an odd number of times, they are topologically non-trivial since they the cannot be adiabatically changed [13]. In this type of system, the topological invariant is $\mathbb{Z}_2$ which results from $C_{\uparrow/\downarrow}$ mod 2, where $C_{\uparrow/\downarrow}$ is the spin-Chern numbers. Thus, $\mathbb{Z}_2 = 0$ indicates trivial topology whilst $\mathbb{Z}_2 = 1$ indicates non-trivial topology. An essential condition to fulfil Kramer's theorem is that the fermionic TRS operator ($\hat{T}$) satisfies $\hat{T}^2 = -1$. Typically, the term topological insulator (TI) refers to a $\mathbb{Z}_2$ insulator hosting QSHE edge states [13].

Additionally, within systems preserving TRS, there is another class of materials with edge modes that arise due to underlying crystalline symmetry properties, the so-called quantum valley Hall effect, which relies on inversion symmetry breaking [18]. As we introduced in the Haldane model, breaking inversion symmetry in a honeycomb lattice will lift the degeneracy of a Dirac point at the $\mathbf{K}$ and $\mathbf{K}'$ high symmetry points; however, the Chen

number is zero since TRS is preserved. Nevertheless, this type of system can still present some topological features determined by another topological invariant: the valley Chern number, C_v [19–21]. This fractional number quantifies the Berry curvature around valleys related by TRS — as $\mathbf{K}$ and $\mathbf{K}'$ points [22] — displaying opposite sign at each $C_v(\mathbf{K}) = -C_v(\mathbf{K}')$. The sum of all the valley Chern numbers within the BZ is equal to the Chern number. For these particular 2D systems C must zero since TRS is preserved. Nevertheless, there is a bulk-boundary correspondence that predicts the presence of topological valley states between regions with valley invariants of opposite sign [23]. Since the gap is locally closed at the valley, facing two materials with opposite C_v for the same valley results in the emergence of valley-polarized edge states at their interface that would be robust against defects that do not interact with the valleys.

1.2 Topological invariants and Wannier representation

Topologically invariant quantities characterize the topological character of any band insulator [24–28]. As we mentioned before, these quantities can be calculated from the complete set of Bloch modes in the energy band. These Bloch functions are periodic and delocalized in the lattice. Nevertheless, it is also possible to study topology of a material in terms of Wannier functions that are the real space representation of the modes that constitute the band. In condense matter physics these functions can be understood as localized orbitals. When a system can be described in terms of exponentially localized Wannier functions, it said to be “Wannier representable". The positions where this function is maximized are known as “Wannier centers". Importantly, this type of description is only possible for topologically trivial materials, since the Wannier functions in topologically non-trivial materials are delocalized and consequently, these materials are not “Wannier representable" [29]. However, there is a type of system which is Wannier representable but still possess localized modes protected by the lattice symmetry. The most representative model which presents this character, due to so called Wannier obstructions, is the Su-Schrieffer–Heeger (SSH) chain[30–32]. In order to explore the localization of the Wannier functions, the spectrum of the Wilson loop operator becomes an useful tool (specially for those phases preserving TRS) since this quantity is related to the projected position of Wannier

functions [33]. The shape of the Wilson loop spectrum for sets of connected bands indicates if the Wannier functions can be exponentially localized, as well as the Chern number associated to those bands. If the eigenvalues of the Wilson loop along the BZ do not wind — the phase does not cover a 2π change — then, this spectrum can be adiabatically transformed to a constant. This indicates that the Wannier functions can be exponentially localized and we can identify the system as topologically trivial. On the contrary, when the spectrum presents windings, this indicates a delocalization of the Wannier functions. The Chern number can be extracted from the spectrum since is equal to the number of the windings, where sign of the Chern number is determined by the slope of the spectrum. For example, the spectrum of a Chern insulator will wind with a slope of the same sign. On the other hand, in the case of $\mathbb{Z}_2$ insulators, two eigenvalue spectra will wind with opposite sign slopes. In addition to these simple examples, different topological phases can also be detected through the application of Topological Quantum Chemistry (TQC) [27]. This characterization tool is based on the symmetry analysis of Wannier and Bloch functions in real and reciprocal space respectively. Applying group theory to the Bloch states, TQC can predict the symmetry and position of the Wannier functions in real space. Moreover, TQC can determine if the system is Wannier representable and sort different topological phases including fragile topology and obstructed atomic limits.

1.3 Topology in photonic systems

Although most of the key concepts in band topology were originally developed in condensed matter physics, many of them were quickly transferred to propagating electromagnetic waves in photonic crystals [9]. Since most fundamental quantities such as the Berry phase, Berry curvature and Wilson loop spectra in the field of topological materials are based on the single-particle picture and the wave propagation through a periodic potential, most topological features can be translated to the propagation of waves in periodic classical systems [10].

In this thesis we focus on the realization of photonic topological insulators for *photonic crystals*. This means that we consider dielectric systems in which the dielectric constant is periodic and the lattice constant is comparable to the order of incident wavelength. The periodicity of the system limits the frequency at which light waves propagate in the system, alike electrons in

condense matter [11]. Thus, the modes of the system can be described by the photonic band structures — similarly to the electronic band structure [12].

1.3.1 Photonic Chern insulators

As we described before, breaking TRS is the key ingredient to achieve a topological Chen insulator. This implies that the direct analogy of QHE can be found in photonic systems. In 2008, Haldane and Rahgu proposed the first theoretical model for a photonic QHE realization [12, 34]. It consists of a system composed by gyromagnetic rods arranged in a hexagonal lattice, whose TRS breaking relies on the Faraday effect. Successively, a physical platform sustaining the photonic QHE was theoretically proposed and experimentally realized in a magneto-optical photonic crystal at microwave frequencies [35, 36]. For the experimental realization, a square lattice is used instead a hexagonal one, since the emergence of the chiral edge states only relies on the difference in the Chern number at the interface [37]. These states are topologically robust, they require strong magnetization conditions to operate.

1.3.2 Photonic $\mathbb{Z}_2$ insulators

The method to achieve TRS invariant topological effects in photonic systems is more complex. Due to the incompatibility between the bosonic time reversal operator and Kramer's theorem, it is very difficult to achieve a strict analogy for a $\mathbb{Z}_2$ insulator and the QSHE in photonics. Therefore, most research on topological effects in TRS invariant bosonic systems has been focused on methods that simulate certain characteristics of those topological systems, as the examples shown in Fig. 1.2. These effects can be realized in TRS invariant systems as coupled ring resonators [21, 38] and photonic crystals made of bianistropic metamaterials [39, 40]. More detailed information about these effects, can be found in Refs. [10, 14, 37].

1.3.3 Photonic valley effects

Since the topological valley effect in electronic systems relies mostly in inversion symmetry breaking, direct analogs can be achieved with quite ease in classical systems Thus, many theoretical and experimental realizations of Photonic topological valley systems have been develop in the recent past [10, 43, 44]. In all of them, breaking inversion symmetry is the key ingredient to gap Dirac cones and achieve a valley-Chern phase [45–47]. In Chapter 4, we

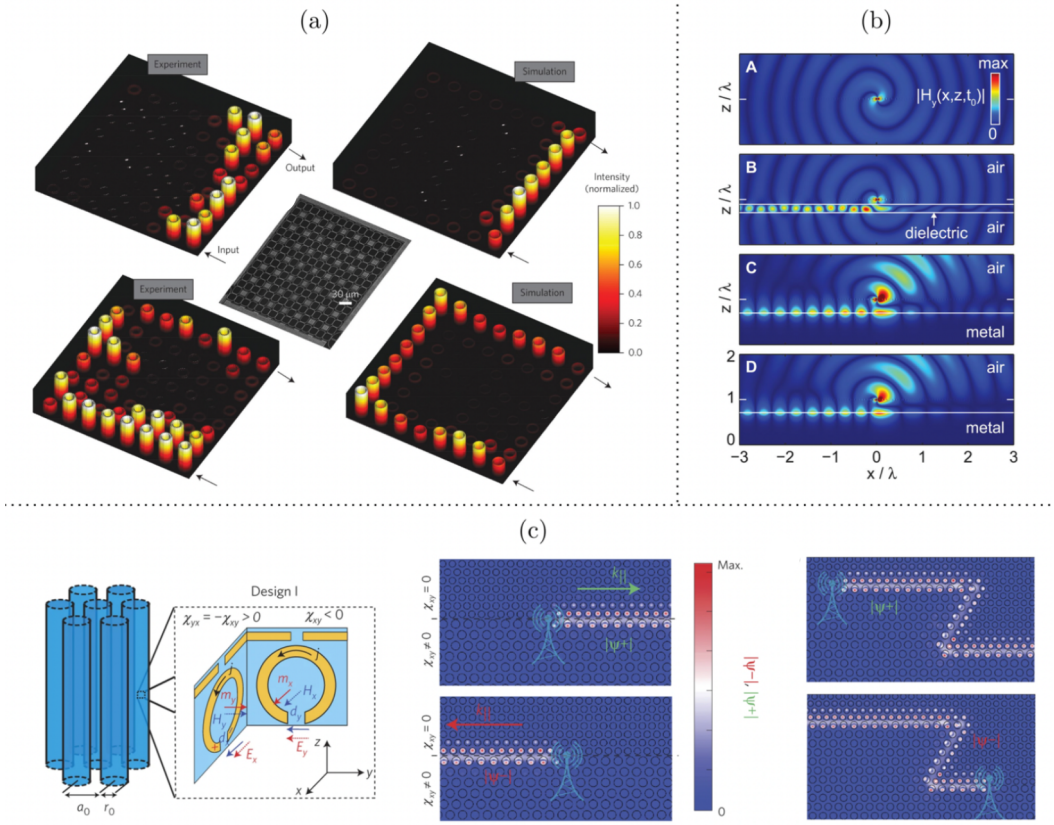

FIGURE 1.2: Examples of unidirectional propagation in photonic systems. (a) Coupled silicon ring resonators [38]. Pseudo-spins engineered from different phases giving rise to edge states. Reproduced from Ref. [21]. (b) Control of the intrinsic spin-orbit interaction of light [41], to achieve unidirectional propagation using a dipole emitter near the dielectric substrates and metal interfaces. Reproduced from Ref. [42]. (c) Bianistropic metamaterials, such lattices of split-ring resonators, used to engineer pseudo-spins and unidirectional modes. Adapted from Ref. [39].

will present an example of a photonic crystal that presents this valley effect, characterized by the valley Chern number C_v.

1.3.4 Photonic Obstructed Atomic Limit (OAL) insulators

In 2015, Wu and Hu proposed a method using photonic crystals to achieve edge states while preserving TRS [48]. This pseudo-spin effect depends on the crystalline symmetry of the so-called “breathing honeycomb" lattice — Fig. 1.3. As we will explain along this thesis, the lattice symmetry leads to similar properties to those of $\mathbb{Z}_2$ topological insulators showing the QSHE. By adjusting the symmetry, they showed that the crystal lattice has similar characteristics, including the energy band inversion between the bulk states

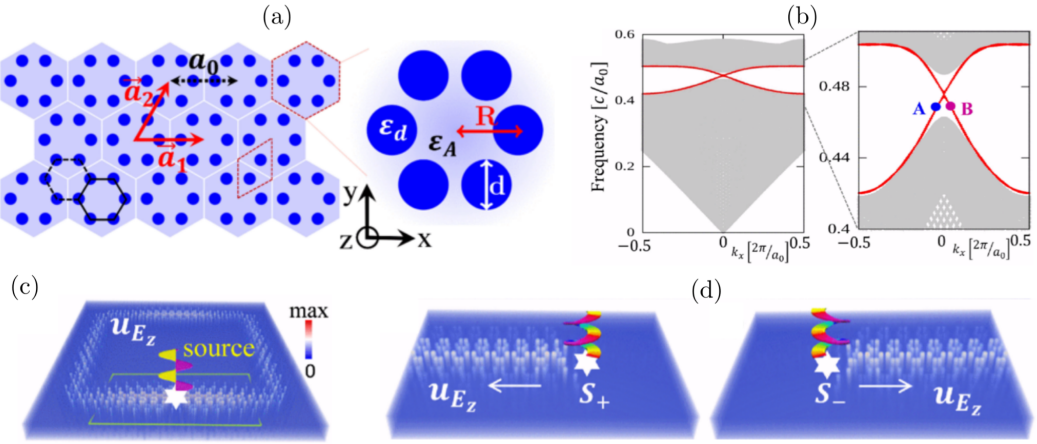

FIGURE 1.3: Engineering modes in a photonic crystal which reminds to those of the quantum spin Hall effect. (a) The breathing honeycomb lattice. A triangular lattice composed by six rods per unit cell, which are contracted (perturbed inwards) or expanded (perturbed outwards). (b) Edge states at the interface between contracted and expanded phases. A small imperceptible gap is present at Γ. (c) Excitation of edge modes with linear polarized light. (d) Excitation of edge modes with circularly polarized light, the excitation position is critical in exciting the unidirectional modes shown. Reproduced from [48].

and the directional edge state with pseudo-spin character. Due to its apparently simple approach and the promise of a true photonic insulator with topological protection, this contribution has led to a considerable interest in these kind of “breathing honeycomb" lattices. These ideas have been applied not only to the study of photonic crystals [49, 50], including optical [51] and microwave [52, 53] regimes, but to other classical systems as acoustic lattices [54] or mechanical [55] systems. For all of them, the emerging edge states have been successfully used to guide and manipulate waves. Although this wave propagation has been proved to be robust against some disorder [56], as we will show in this thesis, none of these breathing honeycomb lattices phases posses a non-trivial $\mathbb{Z}_2$ topological invariant. This implies that they are not a true bosonic analogue of the QSHE. As we detail in Chapters 4 and 6, the effect that Wu and Hu observed can be rigorously explained either using TQC or the eigenvalues of the Wilson loop operator. In a few words, the system turns out to be Wannier representable. Its maximally localized Wannier functions are localized either at the origin or at the edges of the unit cell depending on if the the lattice is on its expanded or contracted configuration. The Wannier states of each lattice represent two opposite atomic limits,

and could be considered a 2D analog of the 1D SSH chain introduced before. The phase these materials represent is named the photonic Obstructed Atomic Limit (OAL) [57].

1.3.5 Photonic fragile topology

Most of the work in the field of topological photonic systems has been focused on producing chiral or helical edge modes in Photonic Chern insulators and Photonic Crystals presenting $\mathbb{Z}_2$ or OAL phases. However, there is still an additional topological phase called "fragile", which was barely explored at the time the research contained in this thesis was beginning to be developed [58–65].

Fragile topology is a property of a given number of bands that can be identified by a bulk topological invariant through the eigenvalues of the Wilson loop operator. The Wilson loop spectra of a set of fragile bands consist in a pair of eigenvalues with opposite windings, which indicate that the Wannier centers are delocalized within the unit cell. This could in principle be an indication of $\mathbb{Z}_2$ topology. Nevertheless, this topological phase presents a distinctive feature; if a trivial band is added in the calculation of the non-Abelian Berry connection (2.19), then the eigenvalues of the wilson loop loose their winding and they behave as in the case of the OAL.

In solid state systems, this phase has been predicted to emerge in twisted bilayer graphene [66, 67] and transition metal dichalcogenide (TMD) heterostructures [68]. More importantly, an experimental realization of fragile topology in acoustic systems were recently shown in Ref. [69].

Chapter 5 of this thesis introduces the first known instance of a photonic crystal presenting fragile topology. Moreover, Chapter 5 explains in detail how fragile topology can be engineered in a Photonic Crystal.

1.4 Thesis structure

The forthcoming chapters of the thesis are structured as follows:

- **Chapter 2** summarizes the basic theoretical tools applied along the rest of the thesis. The first part is dedicated to a detailed explanation of how light propagates within a photonic crystal. Here we detail the assumptions needed to transform macroscopic Maxwell's equations into a periodic eigenvalue problem comparable to Schrödinger's equation.

The second part of this chapter is devoted to an explanation of the fundamental concepts in the field of topological materials. Thus it reviews the expressions used to define topological invariants in the continuous limit. Additionally, this chapter presents a basic description of the theory of TQC, based on symmetry and Wannier functions. The last part of the chapter describes the calculation of quantities such as the density of states (DOS) and local density of states (LDOS) in photonic crystals in the continuous limit.

- **Chapter 3** provides a practical approach on how to apply the theoretical concepts introduced in Chapter 2 in numerical calculations. The first part details the discrete expressions of the key quantities introduced in the previous chapter, together with procedures to compute topological invariants such as the Chern number, the valley-Chern number and the eigenvalues of the Wilson loop operator in numerical computations. Then, we offer a practical description on how to apply TQC in the optical response of photonic crystals. The final part provides a guide to compute the DOS and LDOS numerically.

- **Chapter 4** presents several examples of topological phases found in 2D photonic crystals. We include a detailed characterization of each of them via the computation of the invariants described in Chapter 2 and Chapter 3. We present the analysis for a Chern insulator with broken TRS, a valley Chern insulator with broken inversion symmetry, a system with OAL and a system presenting fragile topology.

- **Chapter 5** is devoted to a in-depth analysis of fragile topology. Here we put a special emphasis on how TQC can be applied to photonic crystals. This characterization is combined with the spectral analysis of the Wilson loop operator.

- **Chapter 6** shows a topological analysis of the breathing honeycomb lattice and other lattices based on it. We analyze the position of the Wannier functions, determined through TQC and the spectra of the Wilson loop operator. Additionally, we compare the predicted Wannier positions with the LDOS for sets of connected bands. This chapter explains in-depth the nature of the OAL phase and why can be easily confused with a $\mathbb{Z}_2$ topological phase.

We wrap up the thesis with a chapter devoted to *Conclusions*.

2 Theoretical Background

This chapter is focused on the theoretical background used to develop this thesis. Our description will start from the macroscopic Maxwell equations that govern light propagation within photonic crystals (PhCs). First, the Maxwell equations must be reduced to an eigenvalue problem. Then, trough the application of Bloch's theorem, we include periodic boundary conditions in our formulation. Afterwards, we explain the theory behind several topological invariants that can be found in the study of the optical response of PhCs. Moreover, we also describe how the theory of topological quantum chemistry (TQC) can be applyied to bosonic systems. Finally, we show as complementary characterization tool how to calculate the density of states (DOS) and the local density of states (LDOS) of PhCs [70, 71].

2.1 Maxwell equations

The propagation of electromagnetic waves in complex media– including the light propagation within PhCs – is governed by the macroscopic Maxwell equations:

$$\nabla \cdot \mathbf{B} = 0 \tag{2.1a}$$

$$\nabla \times \mathbf{E} + \frac{\delta \mathbf{B}}{\delta t} = 0 \tag{2.1b}$$

$$\nabla \cdot \mathbf{D} = \rho \tag{2.1c}$$

$$\nabla \times \mathbf{H} - \frac{\delta \mathbf{D}}{\delta t} = \mathbf{J} \tag{2.1d}$$

Here, $\mathbf{E}(\mathbf{r}, t)$ and $\mathbf{H}(\mathbf{r}, t)$ are the electric and magnetic field, respectively. $\mathbf{D}(\mathbf{r}, t)$ and $\mathbf{B}(\mathbf{r}, t)$ are the electric displacement and the magnetic flux; finally, ρ and $\mathbf{J}$ are the free charges and current densities. The derivation of these formulas from their microscopic counterparts can be found in Ref. [72].

For the purpose of this thesis, we will limit our analysis to media composed by regions of homogeneous dielectric materials that can be described as a function of the position vector ($\mathbf{r}$). We consider as well that there are no free charges or currents in the material, so we can set $\rho = 0$ and $\mathbf{J} = 0$.

Furthermore, we take other reasonable assumptions for many macroscopic dielectric media including PhCs:

- We assume that the field strengths are small enough such that the response can be restricted to linear regime.
- We consider isotropic macroscopic materials. Thus, the relative permittivity $\boldsymbol{\varepsilon}(\mathbf{r}, \omega)$ is a scalar function.
- The materials under study are transparent and have no losses. So, we can treat the dielectric constant $\boldsymbol{\varepsilon}(\mathbf{r})$ as a purely real and positive quantity.
- Finally, we consider that the dielectric function is periodic in space. Then, $\boldsymbol{\varepsilon}(\mathbf{r}) = \boldsymbol{\varepsilon}(\mathbf{r} + \mathbf{R})$, where $\mathbf{R}$ is the lattice vector expressed as linear combination of the primitive lattice vectors of the crystal ($\mathbf{a}_1\ \mathbf{a}_2\ \mathbf{a}_3$), $\mathbf{R} = n_1\mathbf{a}_1 + n_2\mathbf{a}_2 + n_3\mathbf{a}_3$.

Under these assumptions, the electric displacement and magnetic flux can be written in terms of the electric and magnetic fields as,

$$\mathbf{D}(\mathbf{r}) = \varepsilon_0 \boldsymbol{\varepsilon}(\mathbf{r})\mathbf{E}(\mathbf{r}) \tag{2.2a}$$

$$\mathbf{B}(\mathbf{r}) = \mu_0 \mathbf{H}(\mathbf{r}) \tag{2.2b}$$

Then, combining Eq. (2.1) and Eq. (2.2) we get the Maxwell equations as function of the fields:

$$\nabla \cdot \mathbf{H}(\mathbf{r}, t) = 0 \tag{2.3a}$$

$$\nabla \times \mathbf{E} + \mu_0 \frac{\delta \mathbf{H}(\mathbf{r}, t)}{\delta t} = 0 \tag{2.3b}$$

$$\nabla \cdot [\varepsilon(\mathbf{r})\mathbf{E}(\mathbf{r}, t)] = 0 \tag{2.3c}$$

$$\nabla \times \mathbf{H}(\mathbf{r}, t) - \varepsilon_0 \varepsilon(\mathbf{r}) \frac{\delta \mathbf{E}(\mathbf{r}, t)}{\delta t} = 0 \tag{2.3d}$$

To avoid the time dependency — and since we are working with linear equations — we can expand the fields into a set of harmonic modes:

$$\mathbf{H}(\mathbf{r},t) = \mathbf{H}(\mathbf{r})e^{-i\omega t} \tag{2.4a}$$
$$\mathbf{E}(\mathbf{r},t) = \mathbf{E}(\mathbf{r})e^{-i\omega t} \tag{2.4b}$$

In this way, we define the fields — or modes of the system — as a spatial part harmonically modulated in time by a complex exponential. Inserting this definition into Eq. (2.3), we can follow the formulation in frequency domain. Obtaining two divergence equations that set the conditions of transversality,

$$\nabla \cdot \mathbf{H}(\mathbf{r}) = 0 \tag{2.5a}$$
$$\nabla \cdot [\varepsilon(\mathbf{r})\mathbf{E}(\mathbf{r})] = 0, \tag{2.5b}$$

and two curl equations that relate $\mathbf{H}(\mathbf{r})$ and $\mathbf{E}(\mathbf{r})$,

$$\nabla \times \mathbf{E}(\mathbf{r}) - i\omega\mu_0\mathbf{H}(\mathbf{r}) = 0 \tag{2.6a}$$
$$\nabla \times \mathbf{H}(\mathbf{r}) + i\omega\varepsilon_0\varepsilon(\mathbf{r})\mathbf{E}(\mathbf{r}) = 0. \tag{2.6b}$$

Then, following the algebraic manipulation described in Ref. [70], Eq. (2.6) can be decoupled and expressed as two separate eigenvalue problems. One, in terms of the electric field

$$\nabla \times \nabla \times \mathbf{E}(\mathbf{r}) = \left(\frac{\omega}{c}\right)^2 \varepsilon(\mathbf{r})\mathbf{E}(\mathbf{r}). \tag{2.7}$$

And the other one, commonly known as *Master Equation*, in terms of the magnetic field

$$\nabla \times \left[\frac{1}{\varepsilon(\mathbf{r})}\nabla \times \mathbf{H}(\mathbf{r})\right] = \left(\frac{\omega}{c}\right)^2 \mathbf{H}(\mathbf{r}), \tag{2.8}$$

where c is the speed of light, $c = 1/\sqrt{\varepsilon_0\mu_0}$.

Although both formulations are eigenvalue problems,[1] they must be treated differently. Eq. (2.7) is more complex to solve due to the presence of the function $\varepsilon(\mathbf{r})$ on the right-hand side of the expression, which makes it a *generalized eigenvalue* equation. On the contrary, Eq. (2.8) can be easily solved as a Hermitian eigenvalue problem. For this reason, it is the expression most commonly used to determine the eigenfrequencies and eigenmodes of a given system. The usual procedure to explore the modes consists on computing the eigensolutions of the magnetic field using Eq. (2.8), and then recovering the electric field from Eq. (2.6a) [70, 71]. Many commercial and open source software packages have this procedure implemented. All the electromagnetic calculations in this thesis are carried out using MIT Photonic Bands (MPB) [73], which is one of these open sources solvers.

2.1.1 Solid-state electromagnetism

Given that this thesis is focused on the description of 2D PhCs, we can exploit the effect of the crystalline symmetries to complete our description.

Unlike homogeneous media, as air, where the translational symmetry is continuous — the system is invariant under translations of any distance and direction — PhCs have discrete translational symmetry imposed by the lattice. Therefore, the system remains unchanged only if it is shifted by units of the lattice vector $\mathbf{R}$. It is common practice to consider continuous translation symmetry along the z-direction and discrete in the xy-plane as we illustrate in Fig. 2.1.

The translational symmetry operation is defined by the unitary operator of translation, $\hat{T}_{\mathbf{R}}$, which acting over a function displaces the argument by $\mathbf{R}$, *i.e.* $\hat{T}_{\mathbf{R}}\varepsilon(\mathbf{r}) = \varepsilon(\mathbf{r}-\mathbf{R}) = \varepsilon(\mathbf{r})$. As the PhCs that we consider are translationally invariant, the operator of Eq. (2.8) commutes with $\hat{T}_{\mathbf{R}}$. Consequently, the eigenmodes can be classified according to how they behave under $\hat{T}_{\mathbf{R}}$.

Since the fields are expressed in plane wave expansion,[2] the eigenvalues of $\hat{T}_{\mathbf{R}}$ take the form of $e^{i\phi_{\mathbf{R}}}$. For our system we know — from the Maxwell equations — that $\phi_{\mathbf{R}}$ must be linear in $\mathbf{R}$, so introducing the wave vector $\mathbf{k}$ as a

[1] the operator acts over the function transforming it by a scalar factor.

[2] the solutions of Maxwell's equations take the form of a plane wave in structures where the refractive index is constant along the z direction.

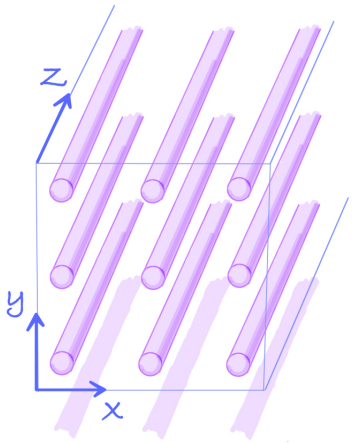

FIGURE 2.1: Segment illustration of a 2D photonic crystal with discrete translational symmetry in the xy-plane and invariant along the z-direction.

parameter, we can define it as $\phi_{\mathbf{R}} = -\mathbf{k} \cdot \mathbf{R}$. Hence, the fields of a PhC can be expressed as Bloch modes labeled by the wave vector $\mathbf{k}$,

$$\mathbf{H}_{\mathbf{k}}(\mathbf{r}) = e^{i\mathbf{k}\mathbf{r}}\mathbf{u}_{\mathbf{k}}(\mathbf{r}) \tag{2.9a}$$

$$\mathbf{E}_{\mathbf{k}}(\mathbf{r}) = e^{i\mathbf{k}\mathbf{r}}\mathbf{v}_{\mathbf{k}}(\mathbf{r}) \tag{2.9b}$$

where $\mathbf{u}_{\mathbf{k}}$ and $\mathbf{v}_{\mathbf{k}}$ are periodic functions of the lattice, *i.e.* $\mathbf{u}_{\mathbf{k}}(\mathbf{r}) = \mathbf{u}_{\mathbf{k}}(\mathbf{r} + \mathbf{R})$.

Going back to the eigen formulation of the Maxwell equations — Eqs. (2.7–2.8) —, now we can solve the problem for each of the propagation directions given by $\mathbf{k}$.

$$\nabla \times \nabla \times \mathbf{E}_{\mathbf{k}}(\mathbf{r}) = \left(\frac{\omega_{\mathbf{k}}}{c}\right)^2 \varepsilon(\mathbf{r})\mathbf{E}_{\mathbf{k}}(\mathbf{r}) \tag{2.10a}$$

$$\nabla \times \left[\frac{1}{\varepsilon(\mathbf{r})}\nabla \times \mathbf{H}_{\mathbf{k}}(\mathbf{r})\right] = \left(\frac{\omega_{\mathbf{k}}}{c}\right)^2 \mathbf{H}_{\mathbf{k}}(\mathbf{r}) \tag{2.10b}$$

The corresponding set of discrete eigenvalues from the problem resolution compose the band dispersion of the system. In this way, we can identify the modes by the band index n — given by the frequency —, and the propagation direction $\mathbf{k}$.

Despite the fact that Eq. (2.10) must be solved as a fully vectorial problem in three-dimensional (3D) structures, we can take advantage of the symmetries

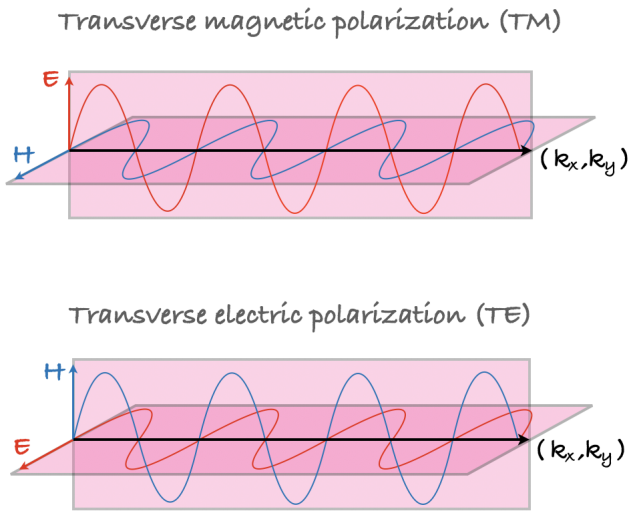

FIGURE 2.2: Illustration of different field polarizations of the electromagnetic field in 2D crystals, which is propagated along the xy-plane. Since the mirror symmetry plane coincides with the propagation plane, we can observe how for TM modes the electric field is odd transformed while for TE modes the magnetic field is even transformed due to its psudovectorial nature.

of our 2D system to simplify the resolution. Particularly, we exploit the mirror reflection symmetry which allows us to classify the eigenmodes into even and odd solutions with respect to this symmetry operation. In general, for any given 2D PhC where $\hat{z}$ is the invariant direction of the system, the fields can be either polarized as (E_x, E_y, H_z) (mirror even) or (H_x, H_y, E_z) (mirror odd). These two polarizations are known as transverse electric (TE) or transverse magnetic (TM) modes respectively. We illustrate how the modes are arrange with respect a mirror plane in Fig. 2.2.

For TM modes, the magnetic field is confined to the xy-plane, therefore the non-zero components of the magnetic field are $H_x(\mathbf{r}), H_y(\mathbf{r})$. Most importantly, the electric field becomes a scalar function, being $E_z(\mathbf{r})$ the only nonzero vector component. Similarly, for TE modes, $H_z(\mathbf{r})$ is the only nonzero component of the magnetic field. Consequently, Eq. (2.10) can be rewritten for 2D

PhCs as two decoupled scalar equations, one for each of polarization.

$$\nabla \times \nabla \times E_z(\mathbf{r}) = \left(\frac{\omega}{c}\right)^2 \varepsilon(\mathbf{r}) E_z(\mathbf{r}) \tag{2.11a}$$

for TM modes

$$\nabla \times \left[\frac{1}{\varepsilon(\mathbf{r})} \nabla \times H_z(\mathbf{r})\right] = \left(\frac{\omega}{c}\right)^2 H_z(\mathbf{r}) \tag{2.11b}$$

for TE modes

We can reduce the differential equation for TE modes defining the following differential operator:

$$\hat{\Theta}[\#] = \nabla \times \left(\frac{1}{\varepsilon(\mathbf{r})} \nabla \times \#\right) \tag{2.12}$$

which is linear and Hermitian [70, 71]. Now, Eq. (2.11b) can be written as

$$\hat{\Theta}\, H_z(\mathbf{r}) = \left(\frac{\omega}{c}\right)^2 H_z(\mathbf{r})\,, \tag{2.13}$$

where $(\omega/c)^2$ is the eigenfrequency of the eigenfunction $H_z(\mathbf{r})$.

At this point, it is important to recall the formal equivalence of Eq. (2.13) with respect to the stationary Schrödinger equation ($\hat{H}\ \Psi(\mathbf{r}) = E\ \Psi(\mathbf{r})$) — used to described periodic systems in condense matter physics. As consequence, most of the concepts developed for condense matter can be applied to PhCs keeping in mind the most important difference: the fermionic character of electronic systems vs. the bosonic character of electromagnetic systems.

2.2 Topology

In general, given a quantum or classical periodic differential operator, its spectrum can be arranged in a sequence of bands and gaps. Many of the physical properties of crystalline materials can be inferred from the intensity distribution of the Bloch states and their bulk spectrum. Nevertheless, these quantities cannot tell us anything about the geometrical phase acquired by the eigenmodes when they evolve in k-space. Instead, considering the shape of the Bloch states is essential for the topological classification of materials.

This classification could be carried out through topological invariants calculations or through symmetry analysis of the eigenmodes. In this section, we review the theory behind the invariants used throughout this thesis [14, 74]. Also, we explain the fundamentals of the theory of topological quantum chemistry (TQC) that relates real and reciprocal space by symmetry, and how a material can be topologically assessed.

2.2.1 Berry phase, curvarture and connection

In electronic systems the topological properties are associated to the bands below the Fermi level, but this concept does not exist for classical waves. However, it is possible to address the bands and gaps of the system individually by tuning the frequency of the photons exciting the lattice. Therefore, we can characterize the topological properties associated to gaps by the analysis of the band or group of bands — whenever they present degeneracy points — below the gap.

Although this thesis is focused in 2D systems, we start explaining the topological phenomena with the most simple case in one dimension (1D) — the Su-Schrieffer–Heeger (SSH) model [30–32]. This model consists on a 1D chain composed by two lattice sites with different connectivity (Figure 2.3).

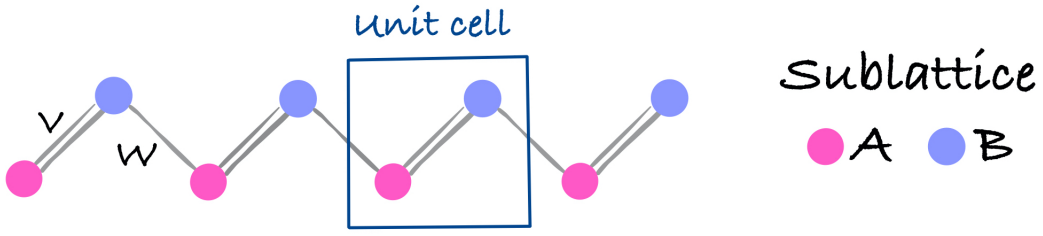

FIGURE 2.3: Schematic structure of the Su-Schrieffer–Heeger (SSH) model

In this system there are two different type of hoppings[3], one intracell and another intercell. Tuning those hoppings drive the system to different topological regimes.

The first regime occur when the intracell hopping term **v** is stronger than the intercell **w**, so the charge will be concentrated inside the unit cell. As we mentioned in the previous section, from the eigenproblem that define

[3]term used referring the interaction strength between cell sites

the system, we can obtain the eigenvalues and Bloch eigenvectors along the first BZ. We illustrate in Figure (2.4) how the band structure looks like for this case, and we can see the closed path described by the bands taking into account the periodicity of reciprocal space.

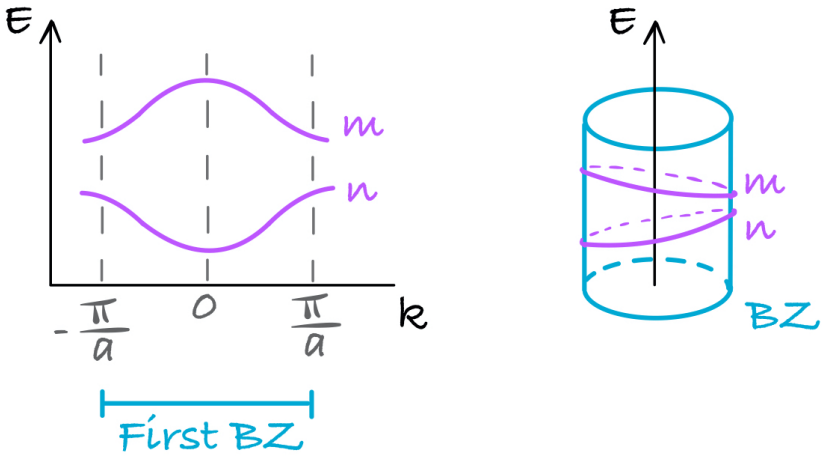

FIGURE 2.4: Schematic representation of the bands in the Brillouin zone for the trivial regime of the SSH model.

For the 1D case, the first BZ takes values between $-\pi/a$ and π/a. This $2\pi/a$ periodicity is reflected in the bands as well as in the eigenfunctions. To identify the topology of the system, we explore the adiabatic evolution of the function along the BZ. The band n — bellow the gap (Figure 2.4) — can be characterized by the study of the so-called Berry (Pancharatnam-Zak) phase [74–77]. This phase is acquired by the eigenstate of the band n along a closed path γ in reciprocal space. The general expression of the Berry-Pancharatnam-Zak phase is:

$$\phi_n = \oint_\gamma \mathbf{A}_n(\mathbf{k}) \cdot d\mathbf{k}\,, \tag{2.14}$$

where $A_n(\mathbf{k})$ is the so-called Berry connection that is defined as

$$\mathbf{A}_n(\mathbf{k}) \equiv i \langle \mathbf{u}_{n,\mathbf{k}} | \nabla_\mathbf{k} | \mathbf{u}_{n,\mathbf{k}} \rangle \tag{2.15}$$

where $\mathbf{u}_{n,\mathbf{k}}$ are the periodic part of the Bloch states at a given $\mathbf{k}$ of the band n.

Following the SSH case, the integral is performed between $-\pi/a$ and π/a which are the values that k can take in the first BZ. Due to the periodicity in reciprocal space, the eigenstate at $k = -\pi/a$ is equal to the one at $k = \pi/a$. Therefore, if we explore the phase evolution of the states, we expect — looking at Eqs. (2.14–2.15)— phase conservation for trivial cases. On the

contrary, any phase with modulo 2π acquired in the adiabatic evolution of the state along the BZ is due to topological effects.

If we want to change from a trivial phase to a topologically non-trivial phase, we have to perform a non-adiabatic transformation which is reflected in the bands as a gap closing and reopening. The degeneracy point happen in the ssh model when both hoppings are equal, $\mathbf{v} = \mathbf{w}$, as we illustrate in Fig. 2.5. For this case, the maxima of charge are placed exactly on the cell sites.

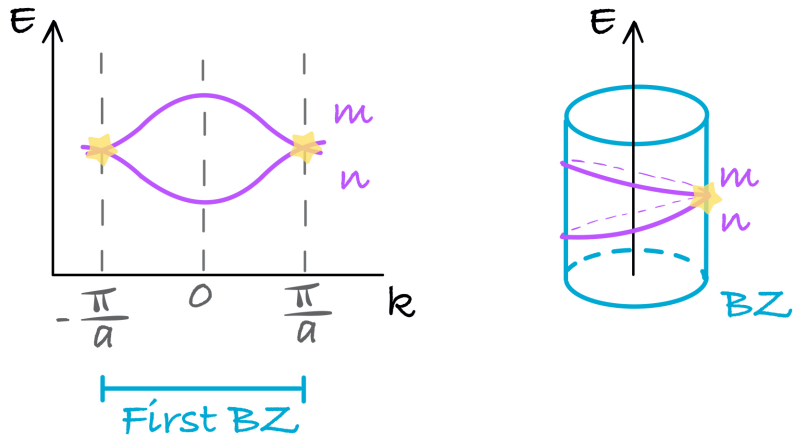

FIGURE 2.5: Schematic representation of the bands in the Brillouin zone for the SSH model when both hoppings are equals. The bands present a degeneracy marked by a star.

Finally, the second regime of the ssh model occur when the itercell hopping $\mathbf{w}$ is greater than the intracell $\mathbf{v}$. This change in the hopping lead to the reopening of the gap. In this case, the charges are placed between unit cells.

For an atomic system, we can easily visualize how the electronic cloud will be concentrate between unit cells while the positive charge of the nuclei is still place on the lattice sites. This unbalance of charge can be translated in the finite size system as edge states protected by chiral symmetry [4]. This is so called the bulk-boundary correspondence, which allow us to predict properties of the boundary — finite system — from the study of the properties of the bulk — infinite periodic system. Although in this regime, the bands are exactly the same as in the first regime showed in Fig. 2.4, the phase evolution is different.

As one can expect from the charge unbalance, the state acquire an additional phase along the BZ in the second regime ($\mathbf{w} > \mathbf{v}$) due to topological effects, while the phase is preserved in the first regime ($\mathbf{w} < \mathbf{v}$). Thus, the Berry

[4] name given for the state invariance under parity transformation

phase of the band n in the first regime has a value of 0, whereas in the second regime has a phase of 2π. At this point it is important to recall that unlike the Berry connection, which is gauge-dependent, the Berry phase is gauge invariant up to multiples of 2π.

Aside from the most simple 1D case, we want to apply those concepts in 2D. So, we can introduce another gauge invariant quantity, the Berry curvature $\Omega_n(\mathbf{k})$, which is defined as:

$$\Omega_n(\mathbf{k}) = \nabla_{\mathbf{k}} \times \mathbf{A}_n(\mathbf{k})\,. \tag{2.16}$$

Applying Stoke's theorem to Eq. (2.14), we can express the Berry phase, ϕ_n, as a function of $\Omega_n(\mathbf{k})$,

$$\phi_n = \oint_\gamma \mathbf{A}_n(\mathbf{k}) \cdot d\mathbf{k} = \iint_\Gamma [\nabla_{\mathbf{k}} \times \mathbf{A}_n(\mathbf{k})]\, d\mathbf{s} \equiv \iint_\Gamma \Omega_n(\mathbf{k}) d\mathbf{s} \tag{2.17}$$

where Γ is a surface bounded by the closed path γ along which the integral in Eq. (2.14) is evaluated. From this expression we can see that the Berry curvature can be understood as the Berry phase per unit of reciprocal area. Mapping this curvature within the first BZ allows to explore phase discontinuities that can be induced by topological effects.

2.2.2 Chern and Valley-Chern number

The first BZ define a closed surface in the directions of periodicity. In Fig. (2.6) we show the closed path in 1D, where the k points are equivalent to those that are displaced by G — that in general is the reciprocal lattice vector expressed as combination of the reciprocal unit vectors.

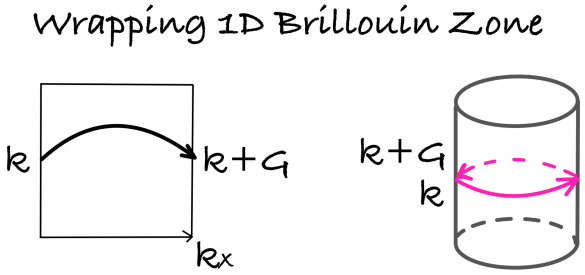

FIGURE 2.6: Schematic representation of the reciprocity for a one dimensional Brillouin zone.

If we extend the periodicity to a second spatial dimension, for 2D systems, the surface is closed in an additional direction describing a torus. In Fig. 2.7

we illustrate how get a torus from a square 2D BZ. This periodicity in reciprocal space implies that the eigenfunctions at k and k+G are equivalent.

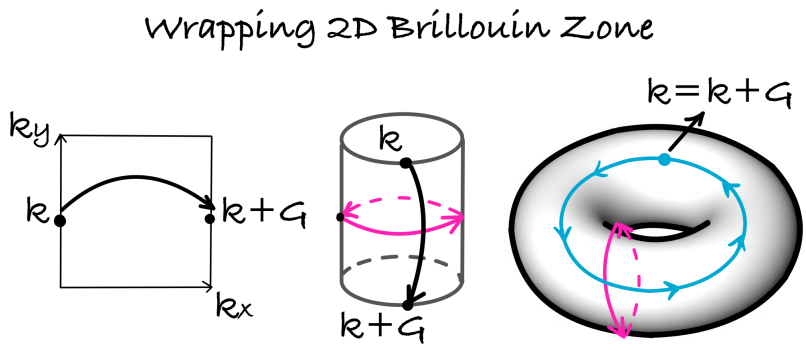

FIGURE 2.7: Schematic representation of the reciprocity for a two dimensional Brillouin zone.

Exploring how the eigenfunctions transform adiabatically within the 1st BZ, the boundary term vanishes but its modulo 2π indeterminacy manifests in the Chern theorem [78]. This theorem states that the integral of the Berry curvature over a closed manifold — as the 1st BZ — is quantized in units of 2π. This integer number is the so-called Chern number, and it is essential for understanding various physical effects when TRS is broken, such as as the QHE [8].

The Chern number for a two-dimensional manifold is defined as:

$$C_n = \frac{1}{2\pi} \oint_{\mathrm{BZ}} \Omega_n(\mathbf{k})\, d^2\mathrm{k} \quad \text{with} \quad C_n \in \mathbb{Z}, \tag{2.18}$$

where the closed surface Γ coincides with the torus defining the 1st BZ (Fig. 2.7).

Therefore, this number quantified the phase acquired due to topological effects. The so-called Chern insulators posses $C \neq 0$ when the TRS is broken, this number also gives information about the boundary since the integer number coincides with the number of edge states and the sign indicates the propagation direction of those states. On the other side, when TRS is preserved, the Chern number is always zero.

However, it does not mean that the system is completely trivial. For example, there are systems which present pair of valleys — other "internal" degrees of freedom in the BZ — related by TRS. Although we can observe this valleys mapping the Berry curvature, we also can quantified the topological charge around each valley. Performing the integral in Eq. (2.18) around each valley, the contribution from each valley is isolated and quantified by the so-called valley-Chern number [79]. This number is not integer anymore but fractional. As the topological charge is equally distributed into both valleys but with opposite sign, we expect the same fractional valley Chern number for both valleys but with opposite sign.

2.2.3 Wilson loop and Wannier functions

Aside from valley-Chern insulators, other materials preserving TRS can also have topological properties. This is the case of systems supporting QSHE [17] and fragile phases [58, 59, 62]. For those cases, the study of the eigenvalues of the Wilson loop operator — in momentum space — helps to determine the topological nature of the system. This operator is obtained considering a non-Abelian generalization of the Berry-Pancharatnam-Zak phase.

Considering N connected bands, the non-Abelian Berry connection takes the form:

$$\mathbf{A}_{m,n}(\mathbf{k}) = i\langle u_{\mathbf{k},m}|\nabla_{\mathbf{k}}|u_{\mathbf{k},n}\rangle, \quad n,m = 1,\dots N\,. \tag{2.19}$$

From it, we can derive the unitary matrix that describes the Wilson loop operator as,

$$W(\ell) = \mathcal{P}\exp\left\{-i\int_{\ell} d\mathbf{l}\cdot\mathbf{A}(\mathbf{k})\right\}\,, \tag{2.20}$$

where ℓ is a loop in momentum space and $\mathcal{P}$ denotes a path ordering of the exponential.

For a closed path ℓ described by a straight line through the BZ, the eigenvalues of the Wilson loop correspond to the expectation value of the position operator in real-space with modulo 2π [33, 74].

Therefore, gives us information about the localization in real space of the Wannier center — expected position of the Wannier function[5].

[5] Although the Wannier functions are used to described the electronic cloud in condense matter physics, for the case of EM-waves they can be related with the localization of the EM-fields.

The Wannier functions are Fourier related with the Bloch modes and can be defined as,

$$w_{i\mathbf{R}}(\mathbf{r}) \equiv \sum_{\mathbf{k}} e^{-i\mathbf{k}\cdot\mathbf{R}} U_{ij}(\mathbf{k}) \psi_{j\mathbf{k}}(\mathbf{r}), \tag{2.21}$$

where $\mathbf{R}$ is the lattice vector, and $U_{ij}(\mathbf{k})$ is an $N \times N$ unitary matrix that represents the space spanned by the N-bands.

These functions can be maximally localized with a well defined center position in the UC as for the cases of topologically trivial materials. Or they can be delocalized within the UC as for topologically non-trivial materials. The position of the Wannier center is equivalent to the bulk polarization which is $\mathbb{Z}_n$-quantized topological invariant for crystalline insulators with C_n-symmetry rotations. The location of these positions for a set of bands can be explored by the adiabatically change of the Wilson loop spectrum.

For trivial bands where the Wannier states are maximally localized, the Wilson loop spectrum shows almost constant values along the reciprocal directions. If the value is 0, it means that the charges are in equilibrium in the UC. Going back to the SSH example, we were in this case at the $\mathbf{w} = \mathbf{v}$ regime where the nuclei and the electronic cloud are placed at the same lattice site. While when we change to the regimen $\mathbf{w} > \mathbf{v}$, the function is localized between two UCs. In those cases, occur an obstruction due to the charge unbalance generating symmetry protected edge modes. This is reflected in the spectrum of the Wilson loop will as constant values around π or $-\pi$. Therefore, in terms of Wannier functions the obstructions are trivial.

In the same terms, for systems that posses non-trivial topology, the Wannier states are delocalized in the crystal. This is reflected in the Wilson loop spectrum as windings, it means that along the reciprocal direction the eigenvalues differs by 2π.

Thus, the Wilson loop is a very powerful tool to extract information about the Wannier states in our system and consequently, about the topological character of the band or group of bands that we want characterized.

2.2.4 Topological Quantum Chemistry

Since the topological nature depends on the crystalline symmetries, we applied the theory of topological quantum chemistry [27] — developed initially for condense matter physics — to photonic energy bands. This theory is based on the fact that the Bloch modes transform in reciprocal space with the same symmetry as — isomorphic to — the Wannier functions do in real space.

Considering a topologically trivial set of bands, the functions $w_{n\mathbf{R}}$ are exponentially localized around some center $\mathbf{r}_n + \mathbf{R}$— which posses the lattice periodicity. In real space, we call Wyckoff position to each point of the unit cell (UC) where those centers can be placed. Nevertheless, for trivial systems the Wannier centers are placed in a more symmetric Wyckoff positions called maximal — which are determined by the spatial group of the lattice. These positions are characterized because they remain invariant under the symmetry operations called generators of the lattice.[6] Each maximal Wyckoff position transforms under its site-symmetry group[7] ($G_{\mathbf{r_n}}$). Thus, the Wannier function centered at this maximal Wyckoff position transforms according to one irreducible representation (*irrep*) of this site-symmetry group.

The symmetry of the eigenmodes in reciprocal space is determined by the symmetry of the function that induce the band(s). The Bloch modes are transformed at each **k**-point under a certain *irrep* of the little group of **k** ($G_{\mathbf{k}}$) [80] — which is the group of symmetry operations that leaves **k** invariant. At specific high symmetry **k**-points, the *irreps* have dimensionality greater than 1 — and up to 8. This type of degeneracy is imposed by the symmetry of the crystal and cannot be broken with small perturbations — that is why they are also known as crosses protected by symmetry.

Assessing the *irrep* of the high symmetry **k**-points for isolated set of bands — separated by gaps, we get their corresponding band representation (BR). The BRs are essential mathematical artefacts to extract topological information [27, 81, 82], since relate by symmetry the localized Wannier functions in real space with the set of bands induced in momentum space.

[6] symmetry operations needed to create the lattice.

[7] symmetry group that describe the maximal Wyckoff position and is a subgroup of the spatial group of the lattice.

All BRs can be obtained as a sum of elementary band representations (EBRs), which are tabulated in Ref. [83, 84]. Each EBR is identified by its space group, the Wyckoff position which labels the set $\mathbf{r}_n$ of centers, and an *irrep* of the group $G_{\mathbf{r_n}}$ which leaves each center invariant. Inverting this observation, any set of bands that cannot be expressed as a sum of EBRs does not admit exponentially localized and symmetric Wannier functions, and is therefore topologically nontrivial. Note that these considerations apply equally well to both photonic and electronic crystals.

2.3 Density of states (DOS) and local density of states (LDOS)

In this section we describe the calculation needed to define the DOS and LDOS in photonic crystalline lattices. Combining both we can get information about the number of states available to excite in the PhC for a given frequency and position. This represents essential key information to couple a crystal and a quantum emitter. To explore how the eigenmodes of the PhC overlap with a radiating dipole emitter, we can define the LDOS [85] as,

$$\rho_\mu(\mathbf{r};\omega) = \frac{6\omega}{\pi c^2}\left[\mathbf{n}_\mu \cdot \mathrm{Im}\left[\mathbf{G}(\mathbf{r},\mathbf{r}';\omega)\right]\cdot \mathbf{n}_\mu\right] \tag{2.22}$$

where $\mathbf{n}_\mu$ is the unit vector in the μ-direction which is determined by the spatial orientation of the emitter. Therefore, $|\mu|$ is the module of the resulting dipolar moment.

If we consider the most simple case, an spherical emitter, the photons can propagate in any spatial direction.[8] Therefore, we can averaging over all the directions,

$$\rho(\mathbf{r};\omega) = \frac{2\omega}{\pi c^2}\mathrm{Tr}\left[\mathrm{Im}\left[\mathbf{G}(\mathbf{r},\mathbf{r}';\omega)\right]\right] \tag{2.23}$$

In both, Eq. (2.22) and Eq. (2.23), $\mathbf{G}(\mathbf{r},\mathbf{r};\omega)$ is the Green's tensor which describes how the emmitter placed at $\mathbf{r}'$ interacts with the electric field of the crystal at a given frequency and position $\mathbf{r}$. In Appendix A we show the derivation needed to find an analytical solution of the Green's function in terms of the eigenvectors. Which is defined as,

[8] Consequently, at certain directions the emitted photons can couple with the electric field of the crystal.

$$\mathbf{G}(\mathbf{r},\mathbf{r}';\omega) = \int_{\mathbf{k}} d\mathbf{k} \sum_n \frac{c^2\omega_{\mathbf{k}n}^2}{\omega^2\left(\omega_{\mathbf{k}n}^2-\omega^2\right)}\mathbf{E}_{\mathbf{k}n}(\mathbf{r})\otimes\mathbf{E}_{\mathbf{k}n}^*(\mathbf{r}') - \left(\frac{c}{\omega}\right)^2\frac{\delta(\mathbf{r}-\mathbf{r}')}{\varepsilon(\mathbf{r})}\,\mathbf{I}\,. \tag{2.24}$$

where the last term, is a real quantity proportional to the identity tensor. The integral of Eq. (2.24) should be treated as a Cauchy principal value integral when the frequency of the dipole coincides with the eigenfrequency, i.e. $\omega = \omega_{\mathbf{k}n}$.

As we are considering the PhC infinite and lossless — as we show in section 2.1 — then, the spectrum is discrete in the form of $\delta(\omega-\omega_{\mathbf{k}n})$. Hence, another approach for this problem resolution consists on introducing an infinitesimal loss to the permittivity $\varepsilon(\mathbf{r})$. This makes the resonant frequencies complex with real parts comparable to $\omega_{\mathbf{k}n}$, and a small imaginary part from the loss rate $\gamma_{\mathbf{k}n}$.[9]

To solve Eq. 2.24 we need to invoke the following mathematical identity:

$$\lim_{\eta\to 0}\operatorname{Im}\left[\frac{1}{\omega_{\mathbf{k}n}^2-(\omega+i\eta)^2}\right] = \frac{\pi}{2\omega_{\mathbf{k}n}}\left[\delta(\omega-\omega_{n\mathbf{k}})-\delta(\omega+\omega_{\mathbf{k}n})\right] = \frac{\pi}{2\omega_{\mathbf{k}n}}\delta(\omega-\omega_{\mathbf{k}n}) \tag{2.25}$$

where we have neglected the term $\delta(\omega+\omega_{\mathbf{k}n})$ because we are concerned only about positive frequencies.

Combining Eq. (2.24) and Eq. (2.25), we get:

$$\rho(\mathbf{r};\omega) = \int_{\mathrm{BZ}} d\mathbf{k}\sum_n \mathbf{E}_{\mathbf{k}n}(r)\otimes\mathbf{E}_{\mathbf{k}n}^*(r)\delta(\omega-\omega_{\mathbf{k}n}) \tag{2.26}$$

The information about the number of resonant eigenstates at each frequency can be extract from the DOS, which are defined as the LDOS integral over the UC,

$$J(\omega) = \int_{\mathrm{UC}}\int_{\mathrm{BZ}} d\mathbf{k}\sum_n \delta(\omega-\omega_{\mathbf{k}n}) \tag{2.27}$$

[9]Conceptually, this means that all the poles of the system are moved from the real axis to the lower-half of the complex plane, preventing in that way the divergence of the aforementioned subspace in the Green's tensor. With this extension to the complex plane, the contribution of each mode to the tensor is a Lorentzian.

If the eigenmodes are normalized with respect to the UC — such that they fulfill the condition $\langle \mathbf{E}_{\mathbf{k}n}(\mathbf{r}) | \mathbf{E}_{\mathbf{k}n}(\mathbf{r}) \rangle = 1$ — the previous expression is reduced to

$$J(\omega) = \int_{\mathrm{BZ}} d\mathbf{k} \sum_{n} \delta(\omega - \omega_{\mathbf{k}n}) \tag{2.28}$$

Although the DOS and LDOS were first derived to couple the crystal and an external emitter, in this thesis we use the LDOS for topological assessment. As we can explore the EM field concentration from a set of bands in real space, we also can relate the position of the maximum density within the UC with the predicted Wannier center position.

3 Fundamentals of topology: the discrete limit

In this chapter, we describe the methodology applied in this thesis to assess the topology of two dimensional (2D) photonic crystals (PhCs). This methodology consists in an adaptation of the continuous formulation described in Chapter 2, to the discrete limit. As we usually do not have access to a continuous form of the periodic part of the field, $u_{n,\mathbf{k}}(\mathbf{r})$, to provide a practical procedure for topological characterization we have to address their values at a set of discrete $\mathbf{k}_i$-vectors — within the first Brillouin zone (BZ).

In the following sections, we detail the calculation methods used in this thesis to compute topological invariants from a finite grid defined in momentum space.

3.1 Discretization of the first Brillouin zone

First, we identify the unit cell and the point group of symmetry for a given periodic 2D system. To carry out such identification, we can analyze the proper symmetry operations following the flowchart shown in Fig. 3.1.

Then, we define its first BZ which is the unitary cell in momentum space determined by the lattice vectors. The set of points generated by translation operations of the primitive vectors, describe its Bravais lattice. We show in Fig. 3.2, how identify the Bravais lattice and the BZ for a square and hexagonal lattice.

Nevertheless, the election of the unitary reciprocal cell is not unique, can be equivalently deformed if the symmetry are respected and the enclosed area is preserved. In Fig. 3.3, we illustrate how the BZ previously defined can be equivalent displaced/distorted in reciprocal space.

Then, we discretize it into a regular mesh of equally spaced $\mathbf{k}$-points following the $\mathbf{b_1}$- and $\mathbf{b_2}$-directions. Each point of the grid defines the momenta of

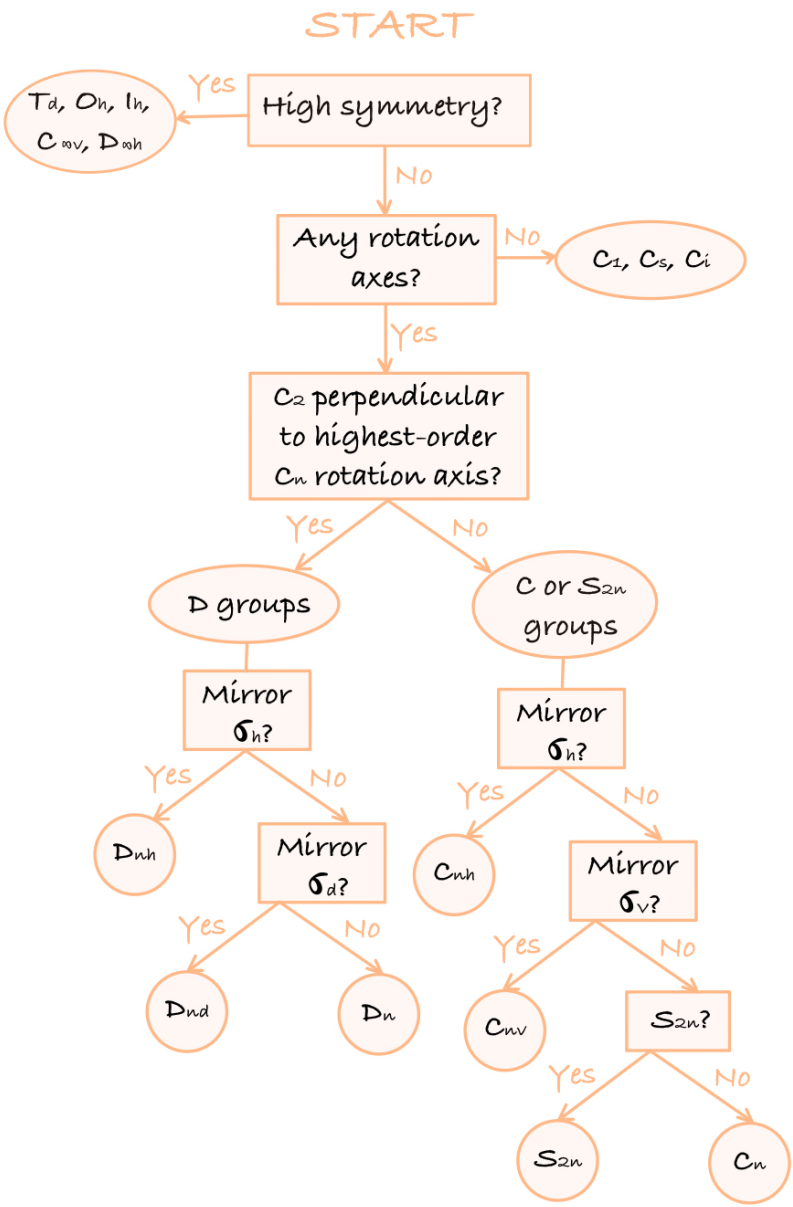

FIGURE 3.1: Point Group determination flowchart. [86]

the periodic eigenfunctions. In Fig. 3.4 we illustrate two examples of BZ discretizations for different lattices in 2D: square and triangular (or hexagonal).

As we mentioned before, the choice of the BZ is not unique but, in general, it is better to choose the most convenient cell to simplify the discretization. For instance, in the case of the triangular lattice (right panel of Fig. 3.4), we take the rhombus BZ instead of the hexagonal one. Since the rhombus is defined by the reciprocal lattice vectors, the discretization is simplified alongside those directions.

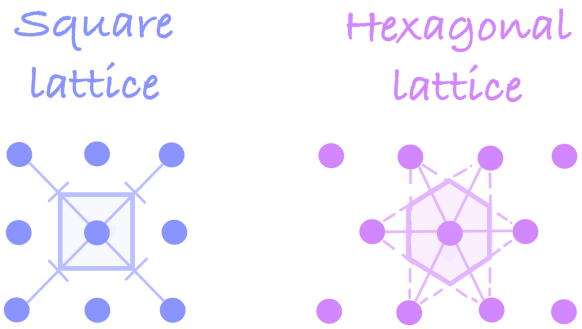

FIGURE 3.2: Schematic graphical determination of the first BZ — shaded area — in a Bravais lattice. On the left side, the blue points define a square lattice. On the right side, the violet points define a hexagonal Bravais lattice.

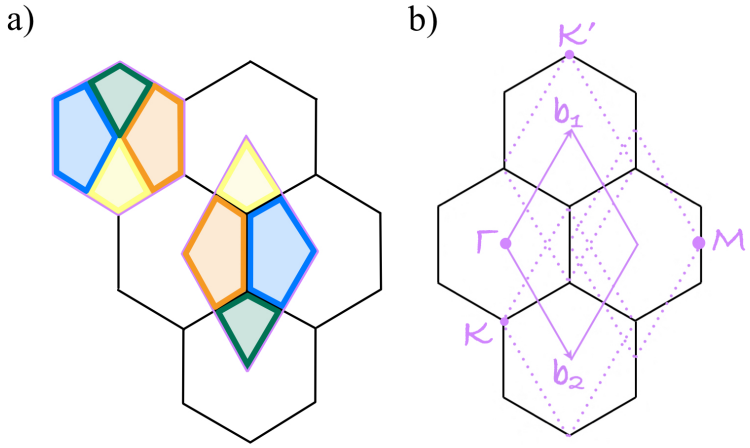

FIGURE 3.3: Schematic representation of reciprocal space for an hexagonal (or triangular) lattice. Panel a) shows that the area enclosed on the hexagonal BZ is equivalent to the the rhombus BZ defined by the reciprocal lattice vectors — $(\mathbf{b_1}, \mathbf{b_2})$. Panel b) shows how this rhombus BZ can be equivalently displaced, setting different high symmetry points as corners.

Although in principle, the grid size should not affect the result of the calculation, we have to use a large enough discretization to achieve an accurate description. For the calculations shown in this thesis we use a grid of at least (24×24) $\mathbf{k}$-points, increasing this number with the complexity of the system. One must choose a number which includes all the high symmetry points, since degeneracies usually occur at these momenta. Therefore, they are the most important $\mathbf{k}$-points for the calculation of topological invariants.

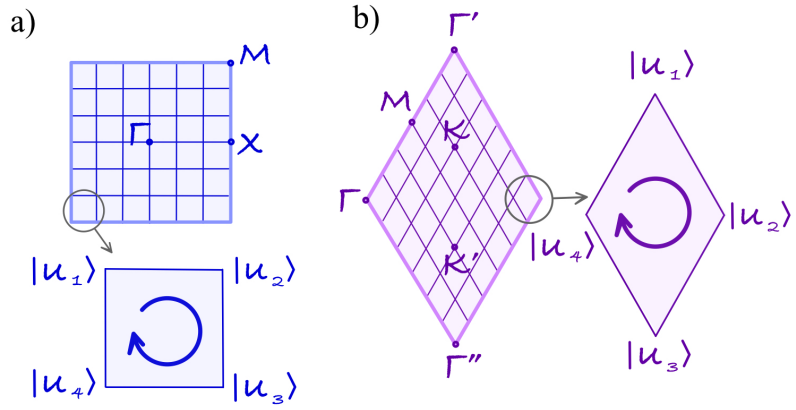

FIGURE 3.4: Discretization of the first BZ for a square a) and triangular lattice b). For each lattice, a zoom-in of the plaquette over which the Berry curvature is evaluated is shown.

Finally, we compute numerically the Bloch eigenstates for each of the grid points, $\mathbf{k}_i$. In our case, we use MPB [73] to solve the eigenvalue equation (2.8).

3.2 Discrete Berry curvature

Using the discrete set of Bloch states computed for each $\mathbf{k}$-point defined by the grid, we can explore how the geometrical phase evolves non-adiabatically in a closed path. Consecuently, we can explore the topological character of a given crystalline PhC. For that purpose, we compute the discrete version of the Berry curvature — or Berry phase per unit of area — applying the four-point formula to each plaquette of the grid. This formulation is a discrete version of Eq. (2.16), that represent the phase acquired by the system due to topological effects. In this discret limit, the Berry-Pancharatnam-Zak phase around a plaquette for a non-degenerate band, is given by [87]:

$$\phi = -\mathrm{Im}\ \log\left[\left\langle u_{\mathbf{k}_1}(\mathbf{r})\middle|u_{\mathbf{k}_2}(\mathbf{r})\right\rangle\left\langle u_{\mathbf{k}_2}(\mathbf{r})\middle|u_{\mathbf{k}_3}(\mathbf{r})\right\rangle\left\langle u_{\mathbf{k}_3}(\mathbf{r})\middle|u_{\mathbf{k}_4}(\mathbf{r})\right\rangle\left\langle u_{\mathbf{k}_4}(\mathbf{r})\middle|u_{\mathbf{k}_1}(\mathbf{r})\right\rangle\right] \tag{3.1}$$

where $u_{\mathbf{k}_j}(\mathbf{r})$ are the periodic functions at each corner of the plaquettes (as is shown in Fig. 3.4).

It is important to emphasize that the path defined along each plaquete is closed, and therefore, the first and last point are the same. Additionally, we observe that in Eq. (3.1) each state appears twice — once as a $\langle$bra$|$ and once

as a $|\text{ket}\rangle$ — and consequently any arbitrary phase coming from the diagonalization procedure cancels out. So, the four point formula essentially isolates the phases coming from topological effects at each plaquette.

For the case of a set of n bands — isolated from the rest — that exhibits one or more degeneracies, we have to replace the scalar products in Eq. (3.1) by the determinant of overlap matrices in order to consider the contribution of all the bands involved. Equivalently to the case of a single band, we can write:

$$\phi = -\text{Im}\ \log\left\{\det\left[\mathcal{S}_{\mathbf{k}_1\mathbf{k}_2}\mathcal{S}_{\mathbf{k}_2\mathbf{k}_3}\mathcal{S}_{\mathbf{k}_3\mathbf{k}_4}\mathcal{S}_{\mathbf{k}_4\mathbf{k}_1}\right]\right\} \tag{3.2}$$

where $\mathcal{S}$ is the overlap matrix with size $(n \times n)$ which considers all the possible overlaps between $\mathbf{k}$ and $\mathbf{k}'$ for the set of n degenerate bands. This matrix can be expressed as,

$$S_{\mathbf{k}\mathbf{k}'} = \begin{bmatrix} \langle u^1_{\mathbf{k}}(\mathbf{r})|u^1_{\mathbf{k}'}(\mathbf{r})\rangle & \langle u^1_{\mathbf{k}}(\mathbf{r})|u^2_{\mathbf{k}'}(\mathbf{r})\rangle & \cdots & \cdots & \langle u^1_{\mathbf{k}}(\mathbf{r})|u^n_{\mathbf{k}'}(\mathbf{r})\rangle \\ \langle u^2_{\mathbf{k}}(\mathbf{r})|u^1_{\mathbf{k}'}(\mathbf{r})\rangle & \langle u^2_{\mathbf{k}}(\mathbf{r})|u^2_{\mathbf{k}'}(\mathbf{r})\rangle & \langle u^2_{\mathbf{k}}(\mathbf{r})|u^3_{\mathbf{k}'}(\mathbf{r})\rangle & \cdots & \langle u^2_{\mathbf{k}}(\mathbf{r})|u^n_{\mathbf{k}'}(\mathbf{r})\rangle \\ \vdots & \cdots & \ddots & \ddots & \vdots \\ \langle u^n_{\mathbf{k}}(\mathbf{r})|u^1_{\mathbf{k}'}(\mathbf{r})\rangle & \langle u^n_{\mathbf{k}}(\mathbf{r})|u^2_{\mathbf{k}'}(\mathbf{r})\rangle & \cdots & \left\langle u^n_{\mathbf{k}}(\mathbf{r})\middle|u^{n-1}_{\mathbf{k}'}(\mathbf{r})\right\rangle & \langle u^n_{\mathbf{k}}(\mathbf{r})|u^n_{\mathbf{k}'}(\mathbf{r})\rangle \end{bmatrix} \tag{3.3}$$

where the superscript ℓ of $u^\ell_{\mathbf{k}}$ indicates the band index.

As we are considering 2D PhCs in this thesis, we can decouple the modes into two different polarizations to simplify the problem arising from the vectorial nature of electromagnetic fields (see Chapter 2). As we will see, for each polarization, the field is normalized differently with respect the unit cell and consequently, the scalar product must be defined according to each polarization. For TM modes, the solutions for the electric field are simpler to manipulate, since they become scalar functions ($\mathbf{E}_{\mathbf{k}}(\mathbf{r}) = E_{\mathbf{k}}(\mathbf{r})\hat{z}$). Defining the Bloch wavefunctions as in Eq. (2.9b), $v_{\mathbf{k}}(r)$ is the periodic part of the electric field solutions. The fields coming from MPB [73] are normalized with respect the unit cell as

$$\langle \varepsilon(\mathbf{r})\ \mathbf{E}_{\mathbf{k}n}(\mathbf{r})|\mathbf{E}_{\mathbf{k}n}(\mathbf{r})\rangle = 1.$$

Due to this normalization constraint, the scalar products in Eqs. (3.1–3.3) must be defined as:

$$\langle v_{\mathbf{k}}(\mathbf{r})|v_{\mathbf{k}'}(\mathbf{r})\rangle = \sum_{r_1,r_2}[\varepsilon(r_1,r_2)\ v_{\mathbf{k}}(r_1,r_2)]^* v_{\mathbf{k}'}(r_1,r_2)\Delta S\,. \tag{3.4}$$

where r_1 and r_2 are the components of the real-space positions, and ΔS is the surface differential.

On the other hand, for TE modes, $u_{\mathbf{k}}(\mathbf{r})$ is the periodic part of the magnetic fields, as we defined in Eq. (2.9a). If we consider materials without magnetic response, we set $\mu = 1$, and the scalar products in Eqs. (3.1–3.3) are defined as:

$$\langle u_{\mathbf{k}}(\mathbf{r})|u_{\mathbf{k}'}(\mathbf{r})\rangle = \sum_{r_1,r_2} u^*_{\mathbf{k}}(r_1,r_2)u_{\mathbf{k}'}(r_1,r_2)\Delta S \tag{3.5}$$

while if we consider materials with magnetic response, as in some Chern insulators, $\mu \neq 1$. In those scenarios, the magnetic fields are normalized by MPB such that

$$\langle \mu(\mathbf{r})\ \mathbf{H}_{\mathbf{k}n}(\mathbf{r})|\mathbf{H}_{\mathbf{k}n}(\mathbf{r})\rangle = 1.$$

The magnetic permeability, μ, should be included in the scalar product as:

$$\langle u_{\mathbf{k}}(\mathbf{r})|u_{\mathbf{k}'}(\mathbf{r})\rangle = \sum_{r_1,r_2} [\mu(r_1,r_2)\ u_{\mathbf{k}}(r_1,r_2)]^* u_{\mathbf{k}'}(r_1,r_2)\Delta S\,. \tag{3.6}$$

3.3 Chern and valley-Chern number

If we integrate the Berry curvature of all the plaquettes over the BZ, we get information about the total topological charge. The result of the integration can be expressed in terms of multiples of 2π, which gives us the definition of the discrete version of the Chern number,

$$C = \frac{1}{2\pi}\sum_{\mathrm{BZ}} \phi_j = \frac{1}{2\pi}\sum_{\mathrm{BZ}} \mathrm{Im}\left[\log \prod_i \langle u_{\mathbf{k}_i}|u_{\mathbf{k}_{i+1}}\rangle\right] \tag{3.7}$$

when TRS is preserved, this number is strictly zero. On the contrary, if TRS is broken, as for materials with an external magenetic field, this number can take non-zero integer values. In those cases, we call the systems Chern insulators. If we consider a heterogeneous system composed of a finite size topological part ($C \neq 0$) and a trivial part ($C = 0$), it will present edge states at the interface. The number of edge states is directly connected to the Chern number of the topological part through the so-called bulk-edge correspondence [13].

Moreover, there are cases where the TRS is preserved and relates pairs of high symmetry points — *e.g.*, the **K** and **K**′ points for a hexagonal or triangular lattice — with non-trivial topological charges that can be complementary. Then,

in order to quantify the topological charge we can define another topological invariant, the valley-Chern number. This invariant addresses the regions that enclose one of the high symmetry points related by the TRS operator.

The computational procedure to calculate the valley-Chern number is the same as the one employed in Eq. (3.7), but reducing the integration of the Berry curvature to one exact half of the first BZ. In the case of a square lattice it can be done with the same four-points formula, while for the hexagonal case, an additional set of three points plaquettes must be added in order to divide the BZ into two identical parts, drawing the division line from $\mathbf{\Gamma}'$ to $\mathbf{\Gamma}'''$ (Fig. 3.4 right panel). Therefore, this "topological invariant" will be half-integer evaluated and with opposite sign for each half of the first BZ.

3.4 Discrete Wilson loop

In this section we discretize the Wilson loop introduced in the previous chapter. As the Wilson loop is path ordered along one of the reciprocal directions, the first and last $\mathbf{k}$-point of the calculation should be equivalent by translational symmetry. Nevertheless, the arbitrary phase added by the diagonalization procedure will be different at each $\mathbf{k}$-point and, in this calculation, it does not cancel out for those points at the BZ boundaries. Therefore, we need to apply a periodic gauge transformation in order to remove any arbitrary phase coming from the diagonalization.[1]

3.4.1 Periodic gauge

In order to fix the gauge choice for the periodic part of the field, we will take advantage of their periodicity. As we mentioned in the previous chapter, the eigenfunctions of a periodic system are described as Bloch states:

$$\mathbf{H}_{\mathbf{k}}(\mathbf{r}) = e^{i\mathbf{k}\cdot\mathbf{r}}\, u_{\mathbf{k}}(\mathbf{r})\,. \tag{3.8}$$

In $\mathbf{k}$-space, the states related by a reciprocal lattice vector $\mathbf{G}$ are equivalent,

$$\mathbf{H}_{\mathbf{k}+\mathbf{G}}(\mathbf{r}) = e^{i(\mathbf{k}+\mathbf{G})\cdot\mathbf{r}}\, u_{\mathbf{k}+\mathbf{G}}(\mathbf{r}) = \mathbf{H}_{\mathbf{k}}(\mathbf{r})\,. \tag{3.9}$$

[1] Although there are other procedures to exclude arbitrary phases in the calculation, we only described the one used in this thesis.

Nevertheless, since calculation at each $\mathbf{k}$-point are independently done, eigenstates with different momentum can present a different arbitrary phase after the diagonalization.

Certain calculations, such as the Wilson loop, require fulfilling the condition imposed by Eq. (3.9). Therefore, we need to fix this arbitrary phase at the boundary eigenstates using the following relation between their periodic parts,

$$u_{\mathbf{k}+\mathbf{G}}(\mathbf{r}) = e^{-i\mathbf{G}\cdot\mathbf{r}} u_{\mathbf{k}}(\mathbf{r}) \,, \tag{3.10}$$

The phase factor of the previous expression can be written as:

$$e^{-i\mathbf{G}\cdot\mathbf{r}} = \frac{u_{\mathbf{k}+\mathbf{G}}(\mathbf{r})}{\mathbf{H}_{\mathbf{k}+\mathbf{G}}(\mathbf{r})} e^{i\mathbf{k}\cdot\mathbf{r}} \,, \tag{3.11}$$

where we have used the formal boundary condition Eq. (3.9). The phase factor on the right-hand side can be obtained from Eq. (3.8),

$$e^{i\mathbf{k}\cdot\mathbf{r}} = \frac{\mathbf{H}_{\mathbf{k}}(\mathbf{r})}{u_{\mathbf{k}}(\mathbf{r})} \,. \tag{3.12}$$

Combining Eqs. (3.11) and (3.12), we finally obtain the phase factor in which we are interested in

$$e^{-i\mathbf{G}\cdot\mathbf{r}} = \frac{u_{\mathbf{k}+\mathbf{G}}(\mathbf{r})}{\mathbf{H}_{\mathbf{k}+\mathbf{G}}(\mathbf{r})} \frac{\mathbf{H}_{\mathbf{k}}(\mathbf{r})}{u_{\mathbf{k}}(\mathbf{r})} \,. \tag{3.13}$$

Concluding, we define the gauged periodic part of the field at $(\mathbf{k}+\mathbf{G})$ by inserting the previous phase factor into Eq. (3.10):

$$u'_{\mathbf{k}+\mathbf{G}}(\mathbf{r}) = \frac{u_{\mathbf{k}+\mathbf{G}}(\mathbf{r})}{\mathbf{H}_{\mathbf{k}+\mathbf{G}}(\mathbf{r})} \mathbf{H}_{\mathbf{k}}(\mathbf{r}) \tag{3.14}$$

$u_{\mathbf{k}+\mathbf{G}}(\mathbf{r})$ being the periodic part of the field at $(\mathbf{k}+\mathbf{G})$ obtained directly from numerical evaluation — in our case with MPB [73] — and $\mathbf{H}_{\mathbf{k}}(\mathbf{r})$ and $\mathbf{H}_{\mathbf{k}+\mathbf{G}}(\mathbf{r})$ the Bloch states at $\mathbf{k}$ and $(\mathbf{k}+\mathbf{G})$, respectively, also directly obtained from MPB [73].
For Wilson loop calculations, it is mandatory to fix this phase at the boundaries by implementing this new corrected periodic function $u'_{\mathbf{k}+\mathbf{G}}(\mathbf{r})$ along the boundaries of the 1$^{\text{st}}$ BZ for all $(\mathbf{k}+\mathbf{G})$ positions.

Importantly, one needs to apply this transformation individually to the $\mathbf{\Gamma}$-point in order to avoid applying the transformation more than once. Additionally, if we look Eq. (2.11b), at zero frequency any constant function is a

solution to Maxwell's equations in 2D. Nevertheless, in order to avoid singularities in the Wilson loop calculation, we choose a constant, normalized eigenfunction for $\omega = 0$ at the $\mathbf{\Gamma}$ point.

3.4.2 Wilson loop calculation

First, it is important to recall that the calculation has to be performed differently for the case of one band or for a group of degenerate bands — in both cases separated from the rest by gaps. For the most simple case, the one-band case, we can calculate the discrete Wilson loop as,

$$W(k_i) = -\mathrm{Im}\left[\log\left(\prod_{k_j}\left\langle u_{(k_i,k_j)}(\mathbf{r})\middle| u_{(k_i,k_{j+1})}(\mathbf{r})\right\rangle\right)\right]. \tag{3.15}$$

This formula indicates that the Wilson loop can be computed for each k_i along the k_1 direction by taking the phase of the final product of the overlap between pairs of consecutive periodic functions. Then, all the eigenvalues of this operator are projected at each $k_j$along the k_2 direction.

For the case of a group of degenerate bands, we replace the scalar product by overlap matrices with the same structure as the ones described in Eq. (3.3). Then the Wilson loop reads,

$$W(k_i) = -\mathrm{Im}\left[\log\left(\prod_{k_j} S_{(k_i,k_j),(k_i,k_{j+1})}\right)\right]. \tag{3.16}$$

In this case, we construct the overlap matrices between consecutive points along the lines in the k_1 direction. Then we multiply the overlap matrices for each pair of points element by element, and the resultant matrix must be diagonalized. The phases of its eigenvalues along the k_2 direction encode information about the position of the (hybrid) Wannier centers in real space.

In two dimensions, one of the momenta k_1 defines the integration variable of the closed path ℓ in Eq. (2.20), while the other momentum k_2 is a free parameter characterizing the Wilson loop.

For a topologically trivial system, the eigenvalues along the momentum k_2 are adiabatically deformable to a constant value, reflecting that the Wannier functions are localized.

For non-trivial topological systems, the eigenvalues may wind as a function of the momentum k_2, meaning that the Wilson loop spectrum presents a variation of $2\pi n$, $n \in \mathbb{Z}$ along the BZ (c.f. Sec. 4.1) — corresponding to delocalization of the Wannier functions. Additionally, from the slope and the number n of windings we can extract important information. The sign of the slope will tell us about the sign of the Chern number, whereas the number of windings will tell us its absolute value. Another possible topological phase is the *photonic* obstructed atomic limit (OAL), which presents non-winding but displaced values of the Wilson loop. Therefore, this phase supports a maximally localized Wannier representation, but in this case the Wannier centers are located between consecutive the real space unit cells, instead of at the origin as for trivial systems. In analogy with an electronic system, it means that in a photonic OAL the Wannier centers are not located at the position where the photonic "atoms" — the collection of dielectric objects in the unit cell — sit [9].

Moreover, there is a recently discovered class of topology referred to as "fragile" topology. Usually, this phase displays a Wilson loop spectra with opposite windings which indicates that although the total Chern number is equal to zero, the Wannier centers are delocalized within the unit cell. This system presents a spectra and topological features similar to those of $\mathbb{Z}_2$ insulators. Although, the special feature of this phase is that if a trivial band is added in the non-Abelian Berry connection (2.19), then the eigenvalues of this enlarged system behave as in the case of the OAL, losing their topological character.

Thus, the Wilson loops are very useful to identify fragile topological phases and $\mathbb{Z}_2$ topological insulators. In both of these scenarios, the total Chern number is equal to zero since TRS is preserved, but the WL spectrum shows clearly pairs of winding with opposite slopes. Although the shape of the Wilson loop spectra is the same for both topological phases, their character significantly differs. For topologically fragile systems, the windings are transformed into a trivial WL spectrum when a new set of trivial bands is added to the topological ones, while for $\mathbb{Z}_2$-insulators, the winding of the WL spectrum is preserved.

At this point, it is important to mention that mimicking $\mathbb{Z}_2$ strong topology in photonic systems requires of duality symmetry and crystal symmetries as a proxy for fermionic TRS [39].

3.5 Topological Quantum Chemistry of light

In this section we describe how to apply the theory of Topological Quantum Chemistry (TQC) to PhCs. The constituents of atomic or molecular crystals are always placed at specific positions of the unit cell (UC), at the maximal Wyckoff positions where the Wannier functions — if the are localized — are placed as well. Therefore, TQC usually analized the ireducible representations (*irreps*) induced from the real functions. On the contrary, for PhCs — or metamaterials — the dielectric material can be placed in any position of the UC. Then, the bands are induced from the collective electromagnetic charge in the UC whose function can be or not exponentially localized. Therefore, the most practical approach to analyze metamaterials starts from the reciprociprocal space.

The topological analysis by symmetry of PhCs consists in several steps summarized in Figure 3.5. Once we have identified the spatial group of the lattice — as well as the group of the reciprocal space if they do not coincide —, we compute the fields at each high symmetry point. Taking into account that each of them transform under specific subgroups of the spatial one, the so-called little group. Using GT-Pack[88, 89] for Mathematica we extract the corresponding collection of *irreps* under which the Bloch modes at high symmetry points are transformed. Then, we can define the band representation (BR) of the system. The BR is composed by all those *irreps* for set of bands separated by gaps. The BR of the system must be compared with the elementary band representation (EBR) of the spatial group that are available on the Bilbao Crystallographic Server (BCS). If the BR of the system can be expressed as sum of EBR then, the system is trivial. If the BR can not be expressed as a sum — or sum of integer linear combination — then, the system is topological. Meaning that the Wannier functions are delocalized. Last, if the BR can be express as a substraction of EBR indicates that this set of bands present fragile topology. If a set of bands induced from a function with the same substracted symmetry is added, then the topology is destroyed becoming trivial.

3.6 DOS and LDOS calculation

In this section, we describe how the DOS and LDOS integrals defined in the previuos chapter can be expressed in a discrete formulation.

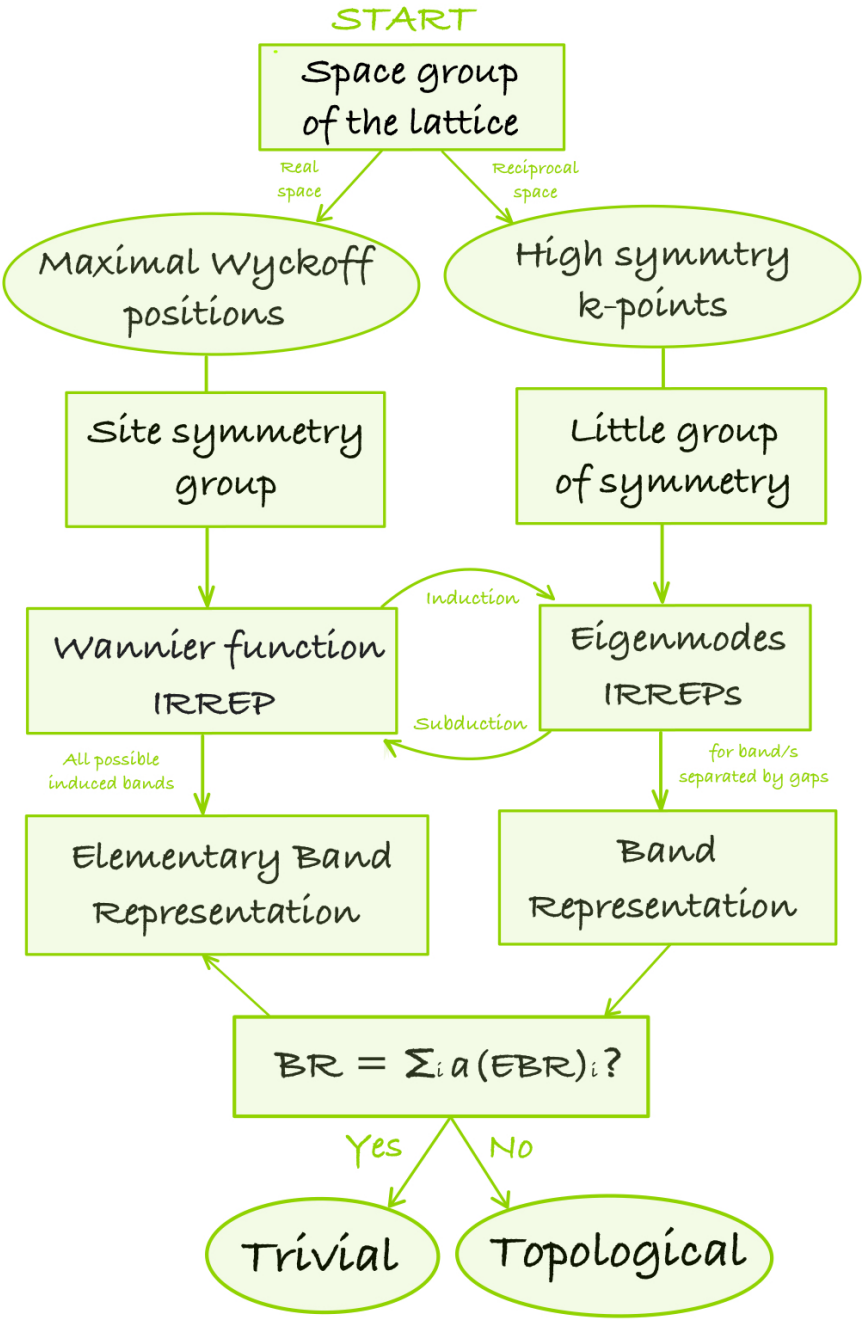

FIGURE 3.5: Flowchart to summarize how to implement TQC.

As, in principle, we want to study the coupling of PhCs to electric dipolar emmiters, we use the electric fields computed for each $\mathbf{k}$-point of the BZ grid to introduce the discretize version of Eq. (2.26),

$$\rho(\mathbf{r};\omega) = \sum_{k_x,k_y} \sum_{n} |\mathbf{E}_{\mathbf{k}n}(\mathbf{r})|^2 \, \delta(\omega - \omega_{\mathbf{k}n}) \Delta k_x \Delta k_y \tag{3.17}$$

This formula considers the electric response over all the k_x and k_y directions of the modes belonging to all n bands with eigenfrequencies at ω.

If we integrate over all real space positions we obtain the discrete formulation of the DOS

$$J(\omega) = \sum_{k_x,k_y} \sum_{n} \delta(\omega - \omega_{\mathbf{k}n}) \Delta k_x \Delta k_y \tag{3.18}$$

This formula essentially counts the number of states available at each frequency, therefore,

$$\delta(\omega - \omega_{\mathbf{k}n}) = \begin{cases} 1 & \text{if} \quad \omega < \omega_{\mathbf{k}n} < \omega + d\omega \\ 0 & \text{otherwise} \end{cases} \tag{3.19}$$

where $d\omega$ is the numerical tolerance that we set to detect the values of $\mathbf{k}$ at which the bands present eigenvalues similar to ω.

We name this method of calculation of the *DOS* and *LDOS* the "Area Method". Nevertheless, one can also express $\rho(\mathbf{r};\omega)$ and $J(\omega)$ as line integrals:

$$\rho(\mathbf{r};\omega) = \int_{l_{\mathbf{k}}} dl \sum_{n} \frac{|\mathbf{E}_{\mathbf{k}n}(\mathbf{r})|^2}{|\nabla_{\mathbf{k}} \omega_{\mathbf{k}n}|} = \int_{l_{\mathbf{k}}} dl \sum_{n} \frac{|\mathbf{E}_{\mathbf{k}n}(\mathbf{r})|^2}{|\mathbf{v_g}(\mathbf{k})|} \tag{3.20}$$

$$J(\omega) = \int_{l_{\mathbf{k}}} dl \sum_{n} \frac{1}{|\nabla_{\mathbf{k}} \omega_{\mathbf{k}n}|} = \int_{l_{\mathbf{k}}} dl \sum_{n} \frac{1}{|\mathbf{v_g}(\mathbf{k})|} \tag{3.21}$$

where $|\mathbf{v_g}(\mathbf{k})|$ is the norm of the group velocity for the wave vector $\mathbf{k}$ at which $\omega < \omega_{\mathbf{k}n} < \omega + d\omega$, and $l_{\mathbf{k}}$ is the closed contour defined by the wavevectors satisfying the condition. These equations can be discretized as

$$\rho(\mathbf{r};\omega) = \sum_{l_{\mathbf{k}}} \sum_{n} \frac{|\mathbf{E}_{\mathbf{k}n}(\mathbf{r})|^2}{|\mathbf{v_g}(\mathbf{k})|} \Delta l^i \tag{3.22}$$

$$J(\omega) = \sum_{l_{\mathbf{k}}} \sum_{n} \frac{1}{|\mathbf{v_g}(\mathbf{k})|} \Delta l^i \tag{3.23}$$

Note that Δl^i, the differential of line, now will be different on each particular point on the line depending on the computationally determined $\mathbf{k} = (k_x, k_y)$-s satisfying $\omega < \omega_{\mathbf{k}n} < (\omega + d\omega)$, and indexed by i. Thus,

$$\Delta l^i = \sqrt{(k_x^{i+1} - k_x^i)^2 + (k_y^{i+1} - k_y^i)^2} \tag{3.24}$$

We name this method of calculation of the DOS and LDOS the "Line Method".

The practical application of this method requires of several computational steps — summarized in Fig. 3.6. First, we take a grid discretization of the BZ

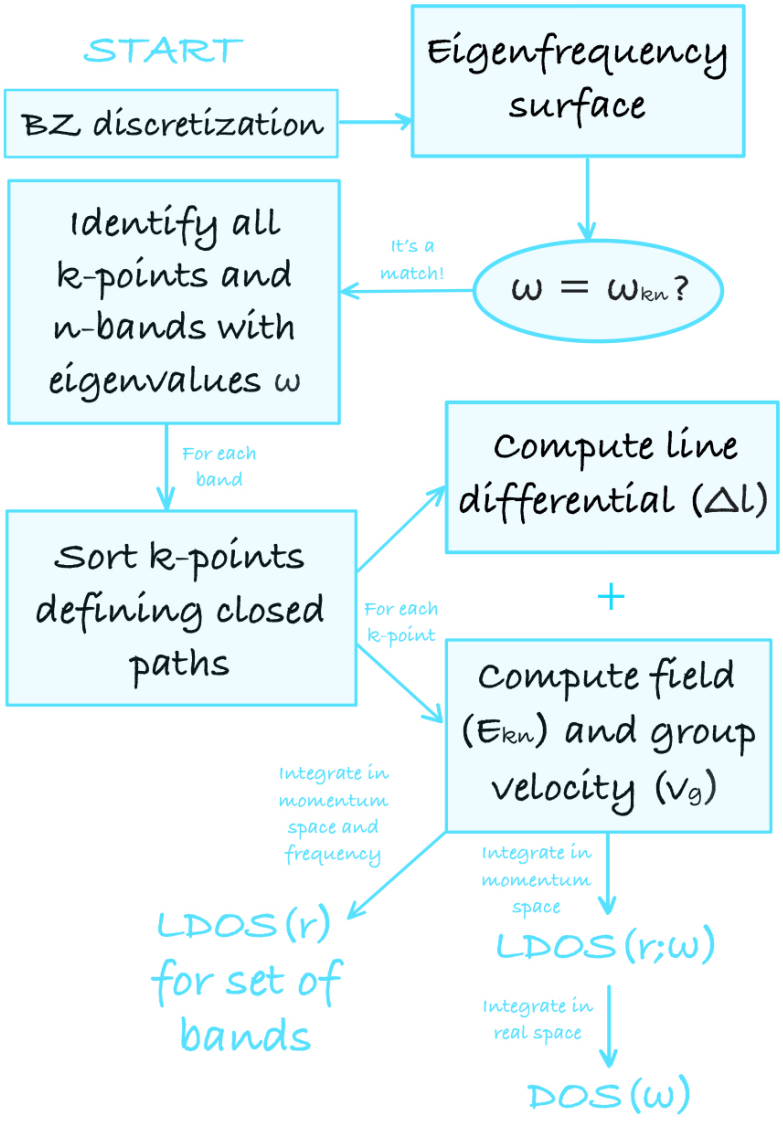

FIGURE 3.6: Flowchart summarizing all the steps needed to compute the LDOS and DOS at each frequency, as well as the LDOS for set of bands.

large enough — in our case, at least 128×128 points[2]. Then, we compute the eigenvalues in order to construct the energy surface. Once we have the surface, we explore the contour levels at each ω with a tolerance of $d\omega = 10^{-7}$. Then, all the wavevectors $\mathbf{k}$ with ω are sorted in order to define a

[2]Usually depends on the system, while more complex, more points are needed to achive a considerable resolution.

closed path[3] and compute the differentials needed as in Eq. 3.24. Finally, at each of those points we compute the electric field and the group velocity to apply Eqs. 3.22–3.23

[3] If the grid is not large enough we can make an interpolation between the **k** points of the contour.

4 Topological Photonic Systems: Examples

In this chapter, we apply the procedures described in Chapter 3 to different topological systems. For different systems, starting from a trivial phase we exploit the symmetry of each system to get topology features by non-adiabatically transformations. Furthermore, we explain how determine the topological phases studied in this thesis as well as their main features and implications.

4.1 Chern Insulator

We start presenting the case of a photonic crystal (PhC) where the electric permittivity $\varepsilon \to \varepsilon(\mathbf{r})$ and the magnetic permeability $\mu \to \mu(\mathbf{r})$ are both periodic functions. For this particular example, we reproduce the case of the gyromagnetic Chern insulator proposed by Wang *et al.* [35].

The proposed trivial system consists on a 2D PhC composed by a square array of yttrium-iron-garnet (YIG) magneto-optic cylinders with radius $R = 0.11a_0$ and isotropic electric response, $\varepsilon = 15$, in air [see Fig. 4.1 a)]. If an external magnetic field is applied in the z-direction, it will induce a gyromagnetic anisotropy which results in the following permeability tensor inside each of the rods:

$$\mu = \begin{bmatrix} \mu & i\kappa & 0 \\ -i\kappa & \mu & 0 \\ 0 & 0 & \mu_0 \end{bmatrix}, \tag{4.1}$$

where $\mu = 14\mu_0$ and $\kappa = 12.4\mu_0$. According to Ref. [35], these values correspond to an applied magnetic field of 0.16 T.

Then, we solve the corresponding equation that describes the propagation of

transverse magnetic (TM) modes[1] in the system (Eq. 2.7). Nevertheless, one must be aware that for the case where the system has magnetic response, we have to reformulate it as,

$$\nabla \times \left[\frac{1}{\mu(\mathbf{r})}\nabla \times E_z(\mathbf{r})\right] = \left(\frac{\omega}{c}\right)^2 \epsilon(\mathbf{r}) E_z(\mathbf{r})\,; \tag{4.2}$$

defining the generalized eigenvalue problem of the system — which includes $\mu(\mathbf{r})$.

In Fig. 4.1, we show the TM band dispersion for the trivial — panel a) — and the topological case — panel b) —, respectively. The transition between the two phases is obtained by switching on the external magnetic field.

For the trivial case, we observe degeneracies between the second and the third band at M, and between the third and the fourth at Γ. The only gap in the system is between the first and the second band. Although this gap is preserved when the magentic field is switched on, the associated Chern number is zero — which means that it is a trivial gap. The external magnetic field breaks time reversal symmetry (TRS) in the system, resulting on the emergence of topological properties. In panel b) we can see that the degeneracies of the higher bands are removed, and two gaps are non-trivially opened.

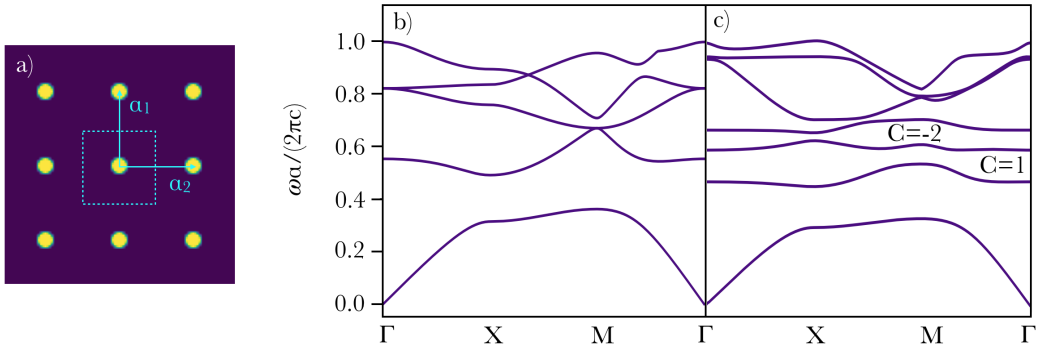

FIGURE 4.1: a) Square array of YIG magneto-optic cylinders of radius $R = 0.11a_0$ in air. The basis vectors of the lattice are: $a_1 = (1,0)a_0$ and $a_2 = (0,1)a_0$. b) TM band dispersion for the trivial system and c) for the Chern insulator with applied external magnetic field.

The next step is compute the fields at each discrete $\mathbf{k}$-point. For the calculations shown here, we used a grid size of (128×128).

[1] Modes with the magnetic field confined in the xy-plane and perpendicular electric field along the z-direction.

Since we are interested in TM modes, we compute $E_z(\mathbf{r})$ and its periodic part, $v_{\mathbf{k}}(\mathbf{r})$ — which are normalized in the unit cell as: $\langle \varepsilon(\mathbf{r}) v_{\mathbf{k}}(\mathbf{r}) | v_{\mathbf{k}}(\mathbf{r}) \rangle = 1$. As we detailed in previous chapters, this normalization of the eigensolutions must be considered for the topological invariants calculation.

If the use of magnetic field solutions $\mathbf{H}(\mathbf{r})$ is preferred, we have to take into account the magnetic response — when it is needed — for the correct normalization. The periodic part of the magnetic modes are normalized with respect the unit cell as: $\langle \mu(\mathbf{r}) u_{\mathbf{k}}(\mathbf{r}) | u_{\mathbf{k}}(\mathbf{r}) \rangle = 1$. We extract the topological information associated with each gap, from the band(s) bellow, using the methods described in previous chapters.

As we can see in Fig. 4.2 a), the Berry curvature of the first band is homogeneous and equal to zero, thus corresponds to a trivial band, while for the rest of the bands Fig. 4.2 b)-d), the Berry phase presents a spatial modulation with a finite average value. This phase modulation indicates that as the eigenvector is propagating in a closed path, there is a manifestation of topological character due to the application of the external magnetic field. It means that those bands possess an associated Chern number different from zero.

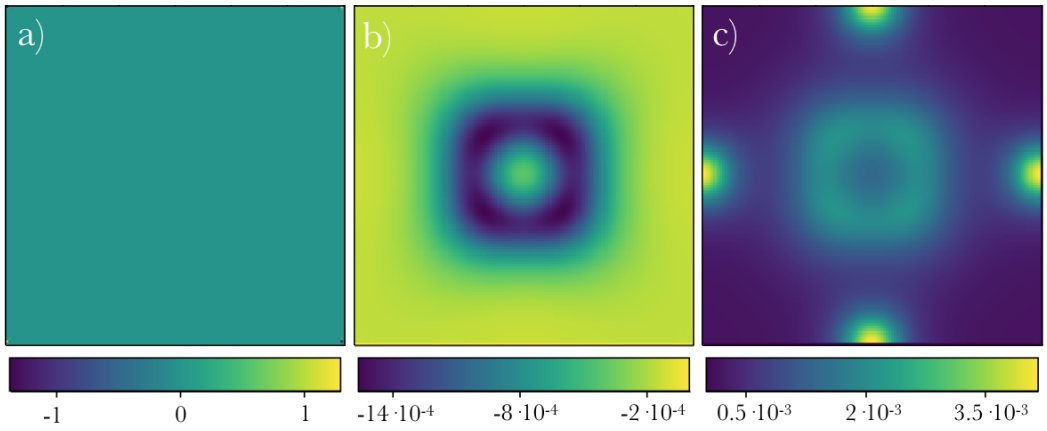

FIGURE 4.2: Berry phase distribution in the unit cell for each band. a) The trivial character of the first band is evidenced by a constant Berry phase equal to zero, while the higher bands – the second b) and third c) – present a phase structure since the Chern number is different from zero.

These results are confirmed and completed by the analysis of the Wilson loop spectra. The spectrum of the first band, Fig. 4.3 a), shows trivial character since the value is constant. On the contrary, the Wilson loop spectrum of the second band winds with positive slope, meaning that the Chern number of this band is 1 — Fig. 4.3 b). For the third band we observe two windings of

the Wilson loop eigenvalues, in this case with positive slope. Therefore the Chern number of this band is -2 [see Fig. 4.3 c)]. It is important to note that the slope of the Wilson loop spectra depends on the sign convention chosen in the exponential in Eq. (2.20).

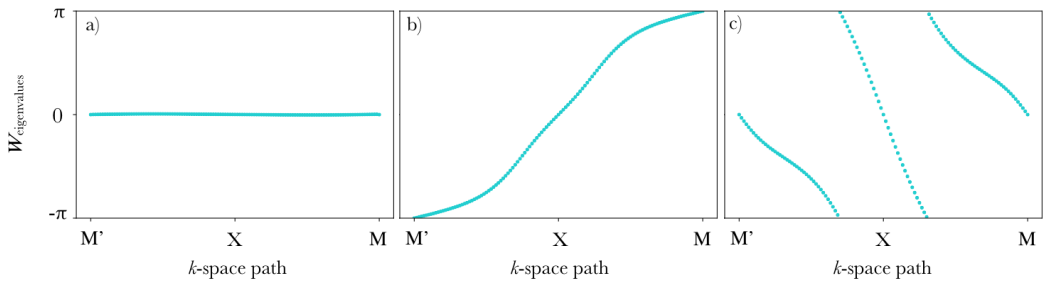

FIGURE 4.3: Wilson loop for each band of the system. (a) Trivial band, $C = 0$, (b) second band, $C = 1$ and (c) third band, $C = -2$.

The windings, and consequently the non-trivial Chern number, are telling us that the Wannier functions are delocalize within the lattice and the charge moves between consecutive unit cells. The consequence of this charge delocalization is reflected in the finite-size system by the emergence of topological modes in the gap. The number edge states that will emerge can be predicted by the sum of the Cher numbers bellow the gap. Also, they will propagate forward or backwards depending on the sign of the Chern number.

These ideas have been experimentally realized in the same set-up but employing different gyromagnetic materials [36]. The experiments have shown the presence of uni-directional edge states associated to the quantized Chern numbers of the system between the second and the third band. A similar experiment in the same set-up has been also conducted as a function of the applied magnetic field to show further topological features of the system [90].

4.2 Valley-Chern Insulator

In this section, we analyze a system that possesses a valley degree of freedom based on the system described by Ma and Shvets in Ref. [91].

We start modeling a PhC which consists in a triangular array of dielectric cylinders made of silicon, ε=13, and radius $R = 0.3075a_0$ — as is shown in Fig. 4.4 a). Then, we explore the spectrum of the transverse electric (TE)

modes[2] of the system. It presents degeneracy points at K and K' between the second and the third band [Fig. 4.4 a)]. As K and K' are points related by TRS, we can observe how this symmetry is preserved in the system since the bands are completely mirror symmetric respect to Γ — along a path including K and K', such as $M - K - \Gamma - K' - M$.

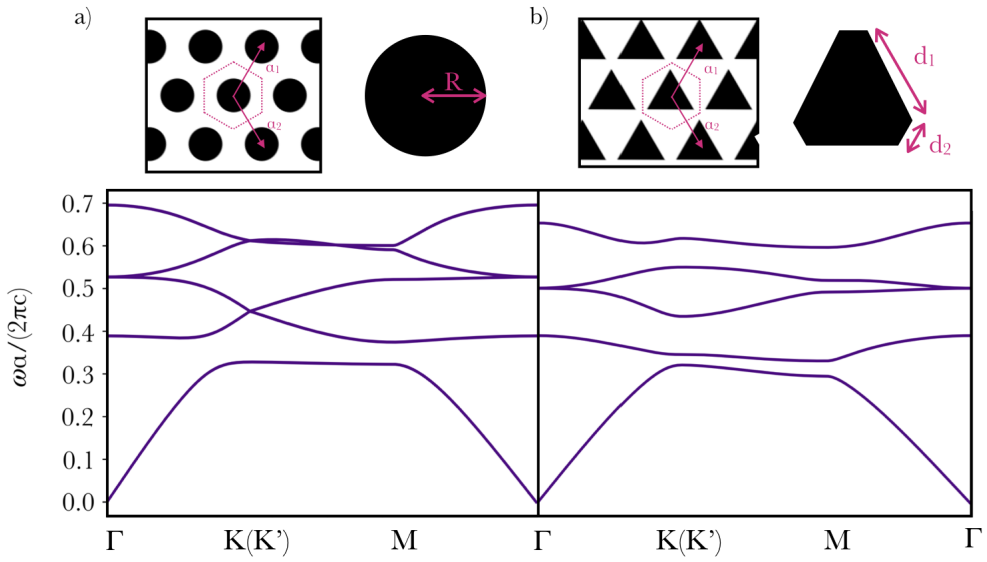

FIGURE 4.4: a) TE band structure and geometry of triangular array of cylinders of radius radius $R = 0.3075a_0$ and ϵ=13. b) Band structure and geometry of triangular array of triangles with ϵ=13. The length of the larger edge is $d_1 = 0.825a_0$ and for the shorter one is $d_2 = 0.055a_0$. Unitary lattice vectors for both are $a_1 = (1/2, \sqrt{3}/2)a_0$ and $a_2 = (1/2, -\sqrt{3}/2)a_0$.

Since we are using the most symmetric shape for the dielectric material, cylinders, all the symmetry of the point group of the triangular lattice ($p6mm$) are preserved. While if we change the shape of the dielectric we reduce the symmetry. Transforming the cylinder into cut triangles, as shown in Fig. 4.4 b), we remove 3-fold mirror axis as well as the C_6 rotation. The main rotation axis of this system is C_3 and thus, the spatial group of the lattice is reduced to $p3m1$. This real space transformation has its consequences for the symmetry of the reciprocal space, where the symmetry is also reduced. Therefore, the modes transform under the symmetry operations of this different space group.

[2]Modes with the electric field confined in the xy-plane and perpendicular magnetic field along the z-direction.

If now we compare the band dispersion of both lattices, we can observe that the only degeneracy preserved is the one at Γ between the third and the fourth band. While the degeneracy at K — and K' — between the second and the third band is removed opening a new gap, as can be seen in Fig. 4.4.

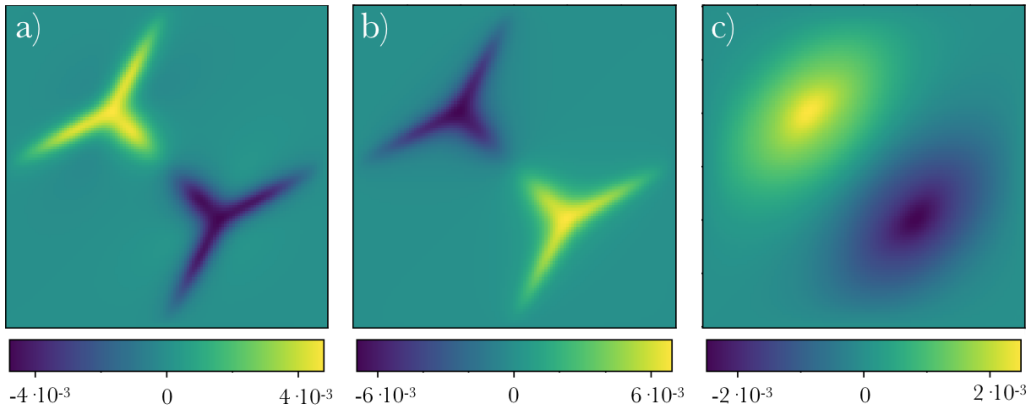

FIGURE 4.5: Berry curvature distribution for the first BZ for the first three bands in the reciprocal space, computed with the four-point formula and plotted with squared shape. We can see that there is a discontinuity of this phase around the K-point and the same but with opposite sign around its time-reversed partner, K'-point.

Since TRS is preserved, the total Chern number associated to this gap is equal to zero. But looking at the Berry curvature (Fig. 4.5) of each set of bands, we observe a spatial modulation with opposite sign around the K and K' points. We can compute the valley-Chern number around these related points, by integrating the Berry curvature over half of the BZ containing only one of the high symmetry points [79]. For this system, we explore the valley-Chern number associated with the gap opened between the second and the third band, around the K point is $C_v = +0.5$, and around K' is $C_v = -0.5$. Therefore, this system present localize topological properties around those points which implies certain propagation directions to achive non-trivial modes.

The absence of a total Chern number is confirmed by the analysis of the Wilson loop spectra, as we can see the displacement of the Wannier centers but without any winding (Fig. 4.6). Since the rate of change of the Wilson loop is proportional to the Berry curvature, we can see also that these plots are consistent with the curvature maps (Fig. 4.5).

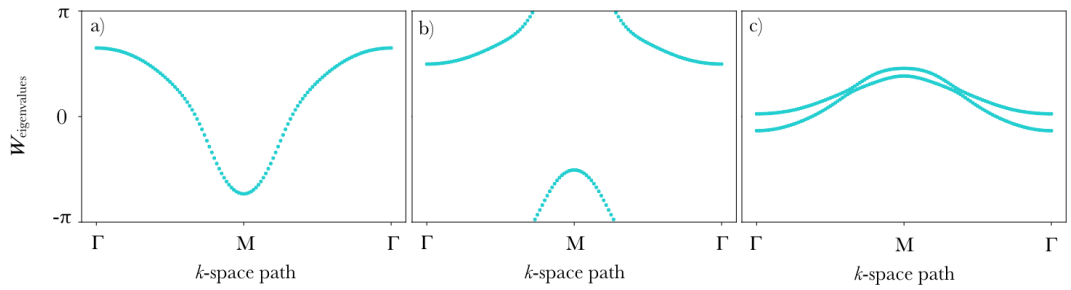

FIGURE 4.6: Eigenvalues of the Wilson loop for the first band a), the second b) and the set of the following two degenerate bands, third and fourth c). All of them show trivial character due to the zero-valued Chern number.

4.3 *Photonic* OAL Insulator

In this section we explore the topological properties of one of the most popular designs employed in the field of topological photonics, introduced by Wu and Hu in Ref. [48, 92].

The system is a triangular lattice with a unit cell containing six cylinders ($\epsilon = 11.7$) with radius $R = 0.12a_0$, placed at a distance $1/3a_0$ from the center of the unit cell. The band structure of this lattice — upper panel of Fig. 4.7 b) — shows an artificial fourfold degeneracy at the Γ-point. This degeneracy emerges from the folding of the bands due to the choice of an artificial enlarged unit cell which is necessary to simulate a breathing honeycomb lattice — in order to move the cylinders towards the center, or the edges, of the hexagon. Displacing the cylinders to different distances from the center of the unit cell these artificial degeneracies are lifted and topological properties may emerge in the associated gaps.

On one hand, placing the cylinders at $a_0/3.16$, contracting the lattice — upper panel of Fig. 4.7 a) — the artificial degeneracy is broken leaving the first band isolated, and two sets of degenerate bands: one group of bands formed by the second and the third band bellow the gap; and another set formed by the fourth and the fifth above. Both sets of bands present degeneracies at Γ and K. To analyze the topological character of those new gaps we can look at the Wilson loop spectra — Fig. 6.10 a) and 6.10 b) — of the bands. For the first band, it shows a constant value equal to zero, which is representative of a trivial gap. For the set of the second and third bands we can see that the projected position of the Wannier centers are slightly moving but without any winding, preserving the trivial character. Which means that the gap is trivially opened. On the other hand, if the cylinders are placed

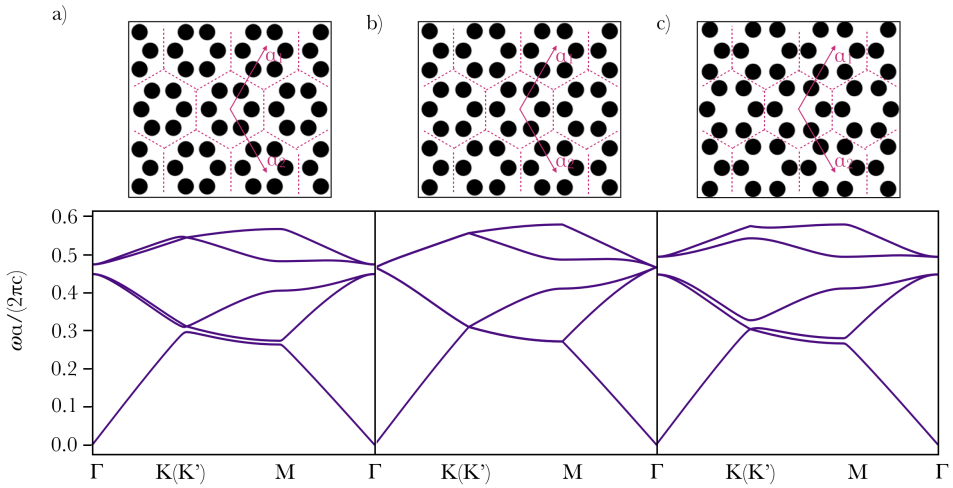

FIGURE 4.7: TM band structure of the artificial honeycomb lattice formed by six cylinders per unit cell. Panel b) refers to the cylinders placed at $1/3a_0$ from the center; a) refers to a contracted lattice, with the center of the cylinders moved to $1/3.16a_0$, and c) to an expanded lattice with the centers of the cylinders at $1/2.78a_0$. For the three of them the unitary vectors are $a_1 = (1/2, \sqrt{3}/2)a_0$ and $a_2 = (1/2, -\sqrt{3}/2)a_0$.

at $a_0/2.78$, expanding the lattice — upper panel of Fig. 4.7 c)— only the gap between the third and the fourth band is opened. In this case, the degeneracy at Γ between the second and the third band is preserved when the gap is opened but the crossing at K is now between the first and the second band indicating that possibly a band inversion occur when the gap is opened by a non-adiabatic transformation. Therefore, to study the topological character of this gap we have to analyze the three lowest bands together. Looking at the Wilson loop spectra — Fig. 6.10 c) — we observe no windings, which indicates trivial character because the Wannier functions are not delocalized. But instead, are localized in the center ($W = 0$) and around the edge of the unit cell ($W = \pm\pi$). Although the charge is not as delocalized as a strong topological insulator, the charge can be shared between consecutive unit cells making possible the emergence of symmetry protected modes with similar features as topological modes. This indicates that the system presents an obstruction similar to that emergent in the Su-Schrieffer-Heeger (SSH) chain in 1D [74], called obstructed atomic limit. Therefore, in analogy to condensed matter, we call optical systems presenting this phenomenology *photonic* OAL insulators.

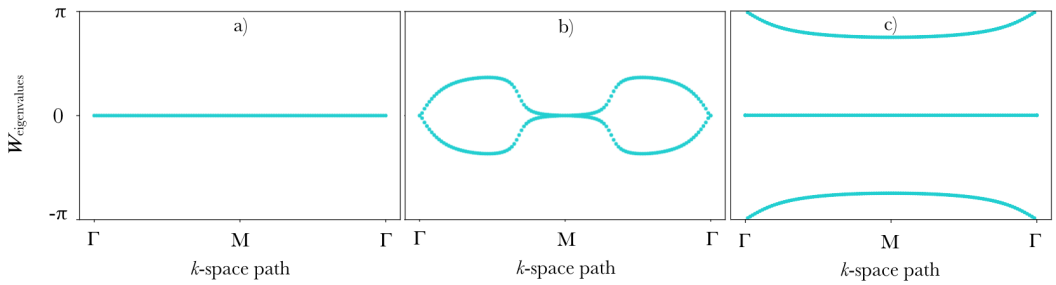

FIGURE 4.8: Wilson loops of the contracted a) and b) and expanded c) artificial honeycomb lattice, respectively. The contracted lattice shows trivial Wilson loops while the expanded shows the characteristic Wilson loop of an OAL.

4.4 Fragile-Phase Insulator

In the previous section, we show how a honeycomb lattice defined by an artificial unit cell that can be adiabatically changed moving the positions of the dielectrics. In this section, we use the system described in [57] to show a fragile photonic phase.

For this case, we use the artificial honeycomb unit cell with six lattice positions but the adiabatic change is made by reshaping the dielectrics — preserving the spatial group symmetry of the lattice (*p6mm*). We transform the cylinders into ellipses and the variation of the length of the ellipses' axes drives topological phase transitions — from fragile to trivial, and from trivial to OAL — by closing and reopening gaps.[3]

The system to exemplify the fragile topology consists of an array of six dielectric ellipses of silicon ($\epsilon = 11.7$) per unit cell, whose length of the two principal axes are $d_1 = 0.4a_0$ and $d_2 = 0.13a_0$, and are placed at $a_0/3$ from the center of the unit cell — Fig. 4.9 a). In Fig. 4.9 b) we show the band dispersion for the TM modes. We can observe two main gaps: one between the first and the second band and another between the third and the fourth. The second and the third present degeneracies at K and Γ. We analyze the Wilson loop spectra to characterize the corresponding sets of bands separated by gaps. For the first band — Fig. 4.10 a) — the eigenvalues of the Wilson loop has a constant value equal to zero which means that the Wannier centers are localized in the center of the unit cell. This shape is typically associated with single trivial bands. For the set of the second and the third bands, we see that the Wilson loops wind with opposite signs. Therefore, the total Chern

[3] We described the system with more details in Chapter 6.

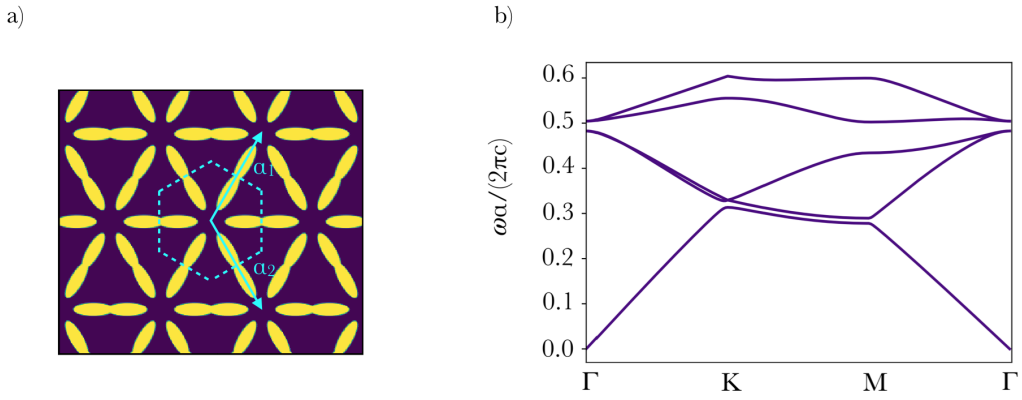

FIGURE 4.9: a) Schematic representation of the system consisting on a triangular array with $a_1 = (1/2, \sqrt{3}/2)a_0$ and $a_2 = (1/2, -\sqrt{3}/2)a_0$, composed by ellipses whose diagonals length are $d_1 = 0.4a_0$ and $d_2 = 0.13a_0$ with $\epsilon = 11.7$ and placed at $a_0/3$. b) The corresponding TM band dispersion.

number for this set of bands is equal to zero. This shape of the Wilson loop spectra is similar to the one of $\mathbb{Z}_2$ insulators, but occurs frequently for fragile bands with twofold rotational symmetry [29]. To distinguish between both

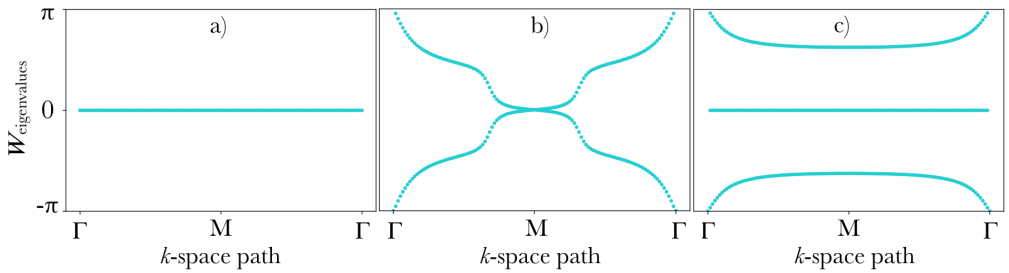

FIGURE 4.10: Wilson loop for: a) first band that possesses trivial topological character, b) set of the second and third band which has two windings with opposite sign and c) set of the three lowest bands that present the shape of an OAL, proving the topological fragility of the former set.

phases, we can add a trivial band to our topological set. If the winding is preserved, then it is a $\mathbb{Z}_2$ topological insulator. While for fragile phases, the winding is destroyed. Thus, we analyze a new subset of bands, the one that contains the three lowest bands. In this case, the winding of the Wilson loop is destroyed and takes the shape of an OAL [Fig. 4.10 c)]. This is a clear proof of the topological fragility associated to the second and the third bands.

In the following chapter, we use group theory as well to deep analyze all the phases obtained by changing the length of the main ellipses' axes.

5 Fragile topology

This chapter is based in the work published in Ref. [57]. First, we introduce the model that describes our family of photonic crystals (PhCs) and we compute the band structures for a several lattice structures. Then, we determine the symmetry properties of the photonic Bloch functions in order to determine the positions of the maximally localized photonic Wannier centers — when they exist — for each crystal structure. Using this symmetry analysis we can identify the parameter range over which our model exhibits fragile topology. Moreover, we verify the results by computing Wilson loop spectra.

5.1 Crystallographic description of the model

For our design, we start choosing a two-dimensional triangular lattice of lattice constant a_0 with an artificially enlarged unit cell of six silicon cylinders ($\varepsilon = 11.7$) of diameter d arranged in a hexagonal pattern. Since we want to preserve the symmetry of the lattice, this non-primitive unit cell is necessary to distort — in a second step — the rods into ellipses along proper lattice directions. The ellipses are described by their principal axes of length d_1 and d_2, being d_1 oriented in the direction of the lattice vectors — *i.e.* pointing towards the center of the unit cell as is shown in panel a) of Fig. 5.1. The PhCs considered in this chapter have the symmetries of the symmorphic space group $p6mm$(# 183) [93]. The Bravais lattice for this space group is generated by the primitive translations:

$$\mathbf{a}_1 = a_0 \left(\frac{1}{2}\hat{\mathbf{x}} + \frac{\sqrt{3}}{2}\hat{\mathbf{y}} \right), \quad \mathbf{a}_2 = a_0 \left(\frac{1}{2}\hat{\mathbf{x}} - \frac{\sqrt{3}}{2}\hat{\mathbf{y}} \right); \tag{5.1}$$

where a_0 is the lattice parameter.

The point group of the lattice is isomorphic to $C_{6v}(6mm)$ whose generators are a sixfold rotation C_6 about the origin, and the mirror reflection m_y —

which interchanges $\mathbf{a}_1$ and $\mathbf{a}_2$. In panel b) of Fig. 5.1, we show the Wyckoff positions[1] of the space group *p6mm* which are relevant for our PhCs. The 1*a* position has reduced coordinates $\mathbf{q}_{1a} = (0,0)$, and the site symmetry group G_{1a} which leaves this position invariant is isomorphic to the full point group of the lattice, C_{6v}. The lattice translations applied to the 1*a* position describe a triangular lattice. The 2*b* position has multiplicity 2 with reduced coordinates $\{\mathbf{q}^1_{2b}, \mathbf{q}^2_{2b}\} = \{(1/3,2/3),(2/3,1/3)\}$, since the operation m_y interchanges $\mathbf{q}^1_{2b}$ and $\mathbf{q}^2_{2b}$. The site symmetry group G_{2b} of each point at the 2*b* position is isomorphic to the point group C_{3v} — that consists of a threefold rotation and a mirror symmetry $C_3 m_y$. Applying the lattice translations to the points in the 2*b* Wyckoff position yields to a honeycomb lattice. The 3*c* position has multiplicity 3, with reduced coordinates $\{\mathbf{q}^1_{3c}, \mathbf{q}^2_{3c}, \mathbf{q}^3_{3c}\} = \{(1/2,0),(0,1/2),(1/2,1/2)\}$. The symmetry operation which permutes these points is C_3. The stabilizer group G_{3c} of each 3*c* position is isomorphic to the point group C_{2v}. Although these points are all the maximal Wyckoff positions of the space group, we also indicate in the figure the non-maximal 6*d* Wyckoff position where we place the elliptical dielectric rods. This latter position has multiplicity 6, and lies along the lines connecting the 1*a* and 3*c* Wyckoff positions.

5.2 Photonic Band Representations

Afterwards, using the MIT Photonic Bands package (MPB) [73], we compute the band structures for the transverse magnetic (TM) modes of three representative configurations of these crystals (Fig. 5.2). As we will show below, there exists a parameter regime where the second and third bands (counting up from zero energy) are isolated from the rest of the states in the spectrum and exhibit fragile topology. Also, there are two different regimes where the set of the three lowest bands present degeneracies: one is a trivial phase and the other an obstructed phase, which are connected by band inversion.

In order to assess the topological properties of the bands in our system, we apply the theory of Topological Quantum Chemistry (TQC) [27] to our photonic energy bands. First, we examine the transformation properties of the Bloch eigenstates of the PhC at each of the high symmetry points $\mathbf{k}_*$ in the Brillouin zone (BZ).

[1] Points within the unit cell that fall into orbits under the action of the space group.

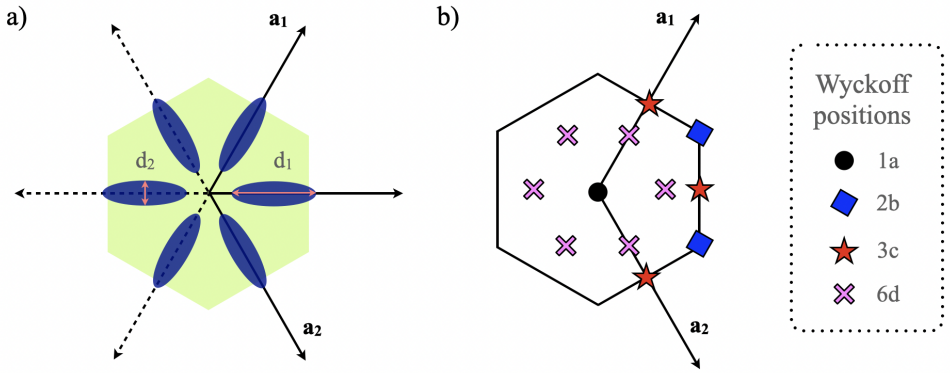

FIGURE 5.1: a) Schematic showing the real-space unit cell of the structures studied in this work. a_1 and a_2 are the real-space lattice vectors. The centers of the ellipses are fixed at a distance $b = \frac{a_0}{3}$ from the center of the unit cell, a_0 being the lattice constant. d_1 and d_2 are the lengths of the principal axes of the ellipses. Higher dielectric constant is shown in blue. When tiling this pattern we use the convention that the dielectric function in any blue region is the same, including when ellipses overlap. b) Shows the real space unit cell with relevant Wyckoff positions labelled. The $1a$ position is indicated by a black circle , the $2b$ position by blue squares, the $3c$ position by red stars, and the $6d$ position by pink crosses.

In the following, we use the reciprocal lattice the vectors as a basis for vectors in the reciprocal space

$$\mathbf{g}_1 = \frac{4\pi}{a_0\sqrt{3}}\left(\frac{\sqrt{3}}{2}\hat{\mathbf{x}} + \frac{1}{2}\hat{\mathbf{y}}\right), \quad \mathbf{g}_2 = \frac{4\pi}{a_0\sqrt{3}}\left(\frac{\sqrt{3}}{2}\hat{\mathbf{x}} - \frac{1}{2}\hat{\mathbf{y}}\right) \tag{5.2}$$

As we explain in Chapter 2, the group of symmetry operations $G_{\mathbf{k}_*}$ that leaves $\mathbf{k}_*$ invariant is known as the little group of $\mathbf{k}_*$. Within the BZ, there are three main classes of $\mathbf{k}$-points with nontrivial little group — the so-called high-symmetry $\mathbf{k}$-points. First, the Γ point with reduced coordinates $(0,0)$ that has as its little group the full space group of the lattice. Next, the K and K' points with reduced coordinates $(1/3,1/3)$ and $(2/3,2/3)$, respectively. The little group of these points is isomorphic to the space group $p3m1$, with point group C_{3v}. Finally, we have another set of points, the M, M', and M'' points with reduced coordinates $(1/2,0),(0,1/2)$, and $(1/2,1/2)$, respectively. The little group of these points is isomorphic to the space group $p2mm$, with point group C_{2v}. We show the hexagonal Brillouin zone with the high-symmetry points labelled in Fig. 5.3.

Thus, the eigenstates at each $\mathbf{k}_*$ transform under irreducible representations

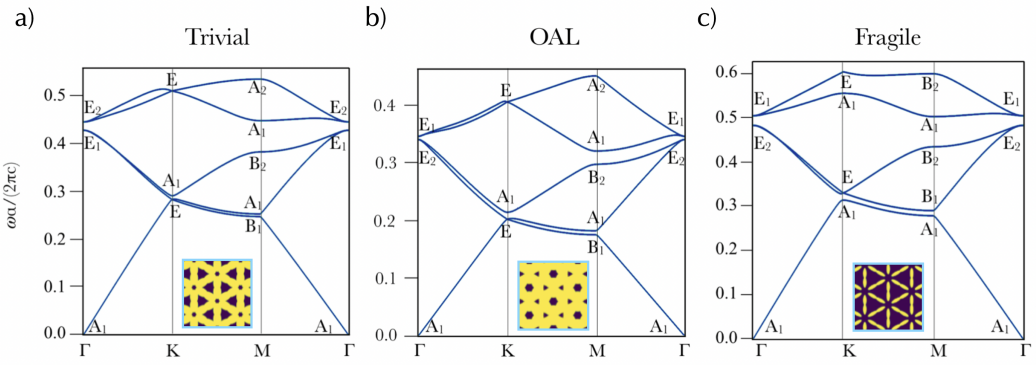

FIGURE 5.2: Photonic band structures of three representative examples studied in this work, with little group representations labeled at the high symmetry points. Inset shows the corresponding arrangement of dielectric ellipses. a) Topologically trivial structure, with $d1 = 0.52a_0$ and $d2 = 0.31a_0$. b) Band structure of a structure representative of the "obstructed atomic limit" (OAL) phase, with $d1 = 0.4a_0$ and $d2 = 0.61a_0$. c) Topologically fragile structure, with $d1 = 0.4a_0$ and $d2 = 0.13a_0$.

(*irreps*) of its little group $G_{\mathbf{k}_*}$ [80]. Note that in 2D lattices, the Wannier functions can be exponentially localized at one specific high-symmetry Wyckoff position $\mathbf{q}$, transforming according to irreducible representations of the stabilizer group $G_{\mathbf{q}}$ of $\mathbf{q}$. Since the space group *p6mm* is symmorphic, both site symmetry and little group *irreps* can be labelled by *irreps* of point groups. In this case, we have seen above that the relevant point groups are C_{2v}, C_{3v}, and C_{6v}. In Table 5.1 we give the character tables for these representations.

Using the GTPack package [88, 89] for Mathematica, we now compute the representation labels at each $\mathbf{k}_*$ in our photonic band structures (see Fig. 5.2). Then, we use the representations of the corresponding little groups given in the Bilbao Crystallographic Server (BCS) [94–96] to compare them with our assignments. Doing so, by looking at the *irreps* of the lowest three bands we identify three different phases in our model (see Table 5.2).

In order to understand how to extract the information about the topological character from the representation labels, it is important to recall [27, 81, 82] that for a set of isolated bands $i \in \{1, \ldots, N\}$ the symmetry properties of the Bloch-wave eigenstates at every momentum $\mathbf{k}$ in the BZ are determined by the symmetry transformation properties of the Wannier function which induces the set of bands.

$$w_{i\mathbf{R}}(\mathbf{r}) \equiv \sum_{\mathbf{k}} e^{-i\mathbf{k}\cdot\mathbf{R}} U_{ij}(\mathbf{k}) \psi_{j\mathbf{k}}(\mathbf{r}). \tag{5.3}$$

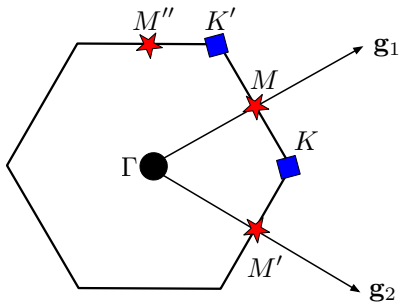

FIGURE 5.3: Schematic representation of the first Brillouin zone with the high symmetry Γ, M, and K points labelled [57]. Note that little group and site symmetry representations of points labelled by black circles are given by *irreps* of C_{6v}. *Irreps* for all blue squares are given by labels for C_{3v}. *Irreps* for all red stars are given by labels for C_{2v}.

Where $\mathbf{R}$ is a lattice vector, and $U_{ij}(\mathbf{k})$ is an $(N \times N)$-unitary matrix which represents a choice of "gauge" for the space spanned by the N-induced bands. For a topologically trivial set of bands, the matrix U can be chosen to make the functions $w_{n\mathbf{R}}$ exponentially localized about some center $\mathbf{r}_n + \mathbf{R}$. In this case, the *irreps* of the site-symmetry group under which the Wannier functions transform fully determines the *irreps* of the little group at each $\mathbf{k}_*$ within the BZ for a given set of bands. Such set of bands receives the name of *band representation*, as defined in Refs. [27, 97, 98]. Therefore, these Wannier functions carry a band representation which can be expressed as a sum of elementary band representations (EBRs) tabulated in Ref. [83, 84].

Each EBR is identified by its space group, the maximal Wyckoff position — which labels the set $\mathbf{r}_n$ of centers (in this case: 1a, 2b, or 3c) — and an *irrep* of the corresponding site-symmetry group $G_{\mathbf{r_n}}$. Thus, they are denoted as:

$$(\rho \uparrow G)_{\mathbf{r}_n}, \tag{5.4}$$

where ρ is an *irrep* of the site symmetry group $G_{\mathbf{r_n}}$ of the Wyckoff position $\mathbf{r}_n$. Although, each EBR contains a finite number of bands, we can define a direct sum $\oplus$ of EBRs concatenating bands. The total multiplicity of all little group *irreps* that appear in a sum of EBRs is equal to the sum of the EBR multiplicities. Similarly, we can define a formal difference of EBRs [29, 67] at the level of little group *irreps*. We define

$$\mathcal{S} \equiv (\rho_1 \uparrow G)_{\mathbf{r}_1} \ominus (\rho_2 \uparrow G)_{\mathbf{r}_2} \tag{5.5}$$

ρ	E	C_2	m_1	m_2
A_1	1	1	1	1
A_2	1	1	-1	-1
B_1	1	-1	-1	1
B_2	1	-1	1	-1

ρ	E	m	C_3
A_1	1	1	1
A_2	1	-1	1
E	2	0	-1

ρ	E	m_1	C_2	C_3	m_2	C_6
A_1	1	1	1	1	1	1
A_2	1	-1	1	1	-1	1
B_1	1	-1	-1	1	1	-1
B_2	1	1	-1	1	-1	-1
E_1	2	0	-2	-1	0	1
E_2	2	0	2	-1	0	-1

TABLE 5.1: Character tables for the point groups used in this work. (a) is the character table for C_{2v}, which labels representations of both G_{3c}, the stabilizer group of the $3c$ position, as well as of the little groups G_M, $G_{M'}$, and $G_{M''}$ of the M points. (b) is the character table for C_{3v}, which labels representations of both G_{2b}, the stabilizer group of the $2b$ position, as well as of the little groups G_K and $G_{K'}$ of the K points. (c) is the character table for C_{6v} which labels representations of both G_{1a}, the stabilizer group of the $1a$ position, as well as of the little group G_Γ of the Γ point.

	Γ	K	M
Trivial	A_1, E_1	A_1, E	A_1, B_1, B_2
OAL	A_1, E_2	E, A_1	B_1, A_1, B_2
Fragile	A_1, E_2	A_1, E	A_1, B_1, B_2

TABLE 5.2: Little group *irreps* for the three gapped phases of our model. *Irreps* at each $\mathbf{k}_*$ are ordered from lowest to highest energy. Note that while the OAL and fragile bands contain the same *irreps* in the lowest three bands, they differ by a band inversion at K and M.

to be the set of little group *irreps* obtained by subtracting the *irreps* in $(\rho_2 \uparrow G)_{\mathbf{r}_2}$ from those in $(\rho_1 \uparrow G)_{\mathbf{r}_1}$ — which determines as well the multiplicity.

The full set of EBRs for all space groups can be found in Ref. [83]. Here, we summarized in Table 5.3 the little group *irreps* which appear in the relevant EBRs for the assignment of phases emerging in our particular system.

Using the *irrep* labels — given in Table 5.2 — for the representative phases, along with the catalogue of EBRs in the BCS [94–96] — summarized in Table 5.3 — we can identify the band representations describing each phase of the PhCs.

For the first structure, with ellipses of $d_1 = 0.52a_0, d_2 = 0.31a_0$, we see that

EBR	Γ	K	M
$(A_1 \uparrow G)_{1a}$	A_1	A_1	A_1
$(E_1 \uparrow G)_{1a}$	E_1	E	$B_1 \oplus B_2$
$(A_1 \uparrow G)_{3c}$	$A_1 \oplus E_2$	$E \oplus A_1$	$A_1 \oplus B_1 \oplus B_2$

TABLE 5.3: EBRs appearing in the lowest three bands of our photonic crystal structures. The first column gives the label of the EBR. The second column gives the little group *irreps* describing bands at Γ in the EBR. Similarly, third column gives the little group *irreps* describing bands at K, and the fourth column the *irreps* for bands at M.

the lowest band carries *irrep* labels consistent with the band representation $(A_1 \uparrow G)_{1a}$. This EBR indicates that the photonic Wannier functions are centered at the origin of the unit cell with zero angular momentum (s-like orbital).[2] The second and third bands are connected to each other, and consistent with the $(E_1 \uparrow G)_{1a}$ band representation, with a pair of Wannier functions centered at the origin of the unit cell and transforming like a dipole (p-like orbital). The set of three bands must be considered together since they present a degeneracy between the first and second band at K which indicates that the characters of both modes are correlated. The spectra of this structure is indicated as the "trivial" phase in Fig. 5.4 a), since all the photonic states can be expressed in terms of localized modes near the origin of the unit cell. Note that although there are no dielectric rods at this maximal $1a$ Wyckoff position, the Wannier functions are trapped by the symmetric arrangement of dielectrics surrounding the origin.

For the next representative structure, with $d_1 = 0.4a_0, d_2 = 0.61a_0$, we see that the first three bands are all interconnected. Taken their *irrep* labels together, we observe that are consistent with s-like photonic Wannier functions centered on a kagome lattice ($3c$ position) which transform under the $(A_1 \uparrow G)_{3c}$ EBR. Although this phase was identified in Ref. [48] as possessing nontrivial topology, here we show that the photonic Wannier functions are localized on a kagome rather than a triangular lattice. Therefore, in contrast to the trivial phase, the centers of these functions lie within the dielectric ellipses and between consecutive unit cells. The band dispersion of this structure is shown in panel b) of Fig. 5.2, labelled as "obstructed atomic limit" (OAL) phase in analogy with similar transitions in electronic materials.

For the last representative structure, with $d_1 = 0.4a_0, d_2 = 0.1333a_0$, we see

[2]The singularity near Γ for photonic modes [99] should not obstruct the formation of Wannier functions for the electric field of TM modes in 2D, since it is polarized out of plane.

that the lowest band can be described by s-like Wannier function centered at the origin of the unit cell $[(A_1 \uparrow G)_{1a}]$, while the second and third bands cannot be expressed as the sum of EBRs. However, the three bands taken together have the same representations as the $(A_1 \uparrow G)_{3c}$ EBR — as in the OAL phase. Therefore, the set of bands 2&3 have the representations which correspond with a subtraction of EBRs, $(A_1 \uparrow G)_{1a} \ominus A_1 \uparrow G)_{3c}$. This representative band structure is shown in Fig. 5.2 c). We will show in following sections that the set of bands two and three realizes fragile topology in this crystal [58, 59].

We summarize our results as a function of the axis lengths d_1 and d_2 in Fig. 5.4, where we show the range parameters for each phase. The numerical details of the calculation are detailed in Appendix C.

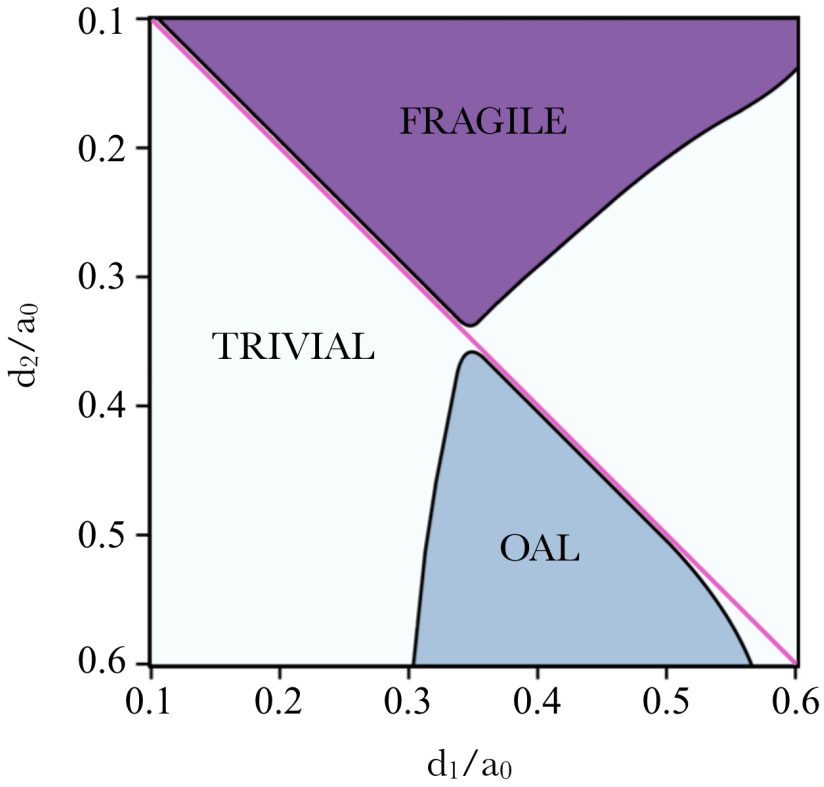

FIGURE 5.4: Phase diagram for the photonic band topology. We show the topological properties of the second and third bands as a function of the length of principal axes of the elliptical rods. Light blue indicates that the bands form the trivial band representation, Dark blue indicates the "obstructed atomic limit" (OAL), and Purple indicates the fragile topological phase. Finally, magenta indicates an intervening gapless phase with fine-tuned degeneracy.

5.3 Wilson loop of the fragile phase

To support the conclusions of the previous section, we compute the eigenvalues of the Wilson loop operator for each isolated set of bands of the structure supporting the fragile topological phase.

As we introduce in Chapter 2, the Wilson loop is a unitary matrix and the phases $\{\theta_i\}$ of its eigenvalues are gauge-invariant modulo 2π. These phases are related to the centers of hybrid Wannier functions — localized in the $\mathbf{a}_2$ direction and extended in the $\mathbf{a}_1$ direction — supported by the bands [87, 100]. In the case when we evaluate the Wilson loop spectra for a small number of bands, the *irreps* of the Bloch functions at high symmetry momenta can place constraints on the allowed topological phases $\{\theta_i\}$ — see Appendix B. Therefore, the EBRs from each of the different maximal Wyckoff positions in this space group have qualitatively different Wilson loop spectra.[3] The Wilson loop spectrum for topologically trivial bands do not cover the entire range $[0, 2\pi]$ of possible phases — i.e. they do not wind. In Fig. 5.5 a) we

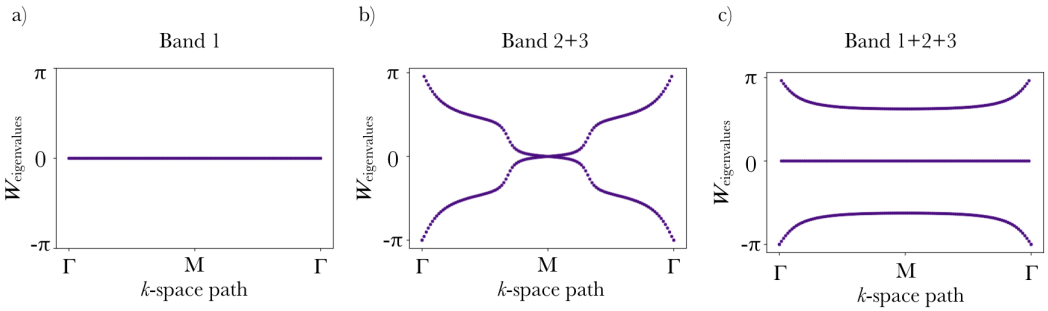

FIGURE 5.5: Wilson loops corresponding to the lowest three in the fragile topological phase. (a) shows the Wilson loop for the isolated first band. The Wilson loop phase here is pinned to $\theta = 0$, a consequence of the C_2 eigenvalues of the band. (b) shows the Wilson loop eigenvalues for the interconnected second and third bands. The Wilson loop spectrum consists of two bands, which wind in opposite directions from $-\pi$ to π as a function of momentum. As in Ref. [58], this winding is guaranteed by the C_2 eigenvalues of the bands, and indicates their nontrivial fragile topology. (c) shows the Wilson loop for all three bands taken together, which does not display any winding.

show the Wilson loop spectrum of the lowest band in the fragile topological structure. The phase is pinned at $W_{\text{eigenvalues}} = 0$, which is consistent with a maximally localized Wannier functions centered at the $1a$ position. In contrast, the Wilson loop spectrum for the second and third bands, shown

[3] We show the Wilson loop spectra of the trivial and OAL phases in Appendix C.

in Fig. 5.5 c), clearly display a nontrivial winding. As we mentioned before, the integer winding number is an indicator of nontrivial topology. Note that before performing these detailed Wilson loop calculations, we were already able to anticipate these results demonstrating the utility of TQC applied to photonic systems.

5.4 Fragile Topology

In contrast to a conventional $\mathbb{Z}_2$ topological insulator, the Wilson loop winding in the topologically fragile phase is *not* protected. In fact, due to the limited number of bands considered, the crossings in the spectrum at $\mathbf{k}_1 = 0$ and $\mathbf{k}_1 = \pi$ are guaranteed by the twofold rotational symmetry C_{2z}. It is important to recall that the C_{2z} invariant points in the BZ are Γ together with M, M' and M''. We can observe in Table 5.2, that bands two and three of the Fragile phase at Γ transform according to the *irrep* E_2 whose C_{2z} eigenvalues are $(+1, +1)$, while at the M points the eigenvalues are $(-1, -1)$ — corresponding to *irreps* B_1, B_2. This means, as was shown in Refs. [58, 101], that the Wilson loop at $\mathbf{k}_1 = 0$ passes through Γ and M and has its phases pinned to π. Similarly, at $\mathbf{k}_1 = \pi$ passes through M' and M'', and its phases are hold in 0. Thus, this forces the winding of the spectrum in panel b) of Fig. 5.5 which indicates nontrivial topology — for a detailed explanation see Appendix C. Indeed, bands two and three realize the same fragile topological phase discussed previously in a toy model in Ref. [58]. In both cases, the *irreps* at the high symmetry points do not match a sum of EBRs, instead they do match a difference of EBRs. Particularly, we can see from above that the *irreps* for bands two and three are consistent with the formal difference

$$(A_1 \uparrow G)_{3c} \ominus (A_1 \uparrow G)_{1a}, \tag{5.6}$$

reflecting the fact that if all the three bands are taken together, they have the same *irreps* as in the OAL case. This reflects the defining feature of fragile topology — that fragile topological bands become trivial when a topologically trivial band is added. We verify this for our model computing the Wilson loop for the lowest three bands — shown in Fig. 5.5 c). The three-band Wilson loop exhibits no winding, and is consistent with Wannier functions centered at the kagome ($3c$) position — showing topological features of OAL.

5.5 Finite-size System

In this section we define a periodic structure composed by a topologically fragile part and another part with trivial topology. To emulate the properties of the finite-size system, we construct a super-cell with the two topological phases extended along one dimension (1D) emulating a ribbon. This super-cell allows us to study the possible emergence of in-gap localized states at the boundary between phases. The fragile topology of the structure is associated to the set of the second and third band of the bulk TM modes. Since this topological character is destroyed when a trivial band is considered together with this specific set of fragile bands, we need a trivial structure that presents a well defined gap in this specific frequency range. This way, we preserve the isolation of the fragile bands and their topological character. To that purpose, we explore the TM modes of a triangular array of cylinders placed at the center of the cell. The dielectric constant of the cylinder is $\varepsilon = 11.7$ and the radius $r = 0.18a_0$. In Fig. 5.6 we show together the band dispersion of the bulk TM modes for both periodic structures. We can observe that the fragile bands are placed into the gap of the trivial phase. Although there are no degeneracies with the fragile bands, the first band of the fragile phase — light blue in Fig. 5.6 — around K is within the energy range delimited by the fragile bands. This fact can lead to the mixing of the character of both structures in the finite-size system.

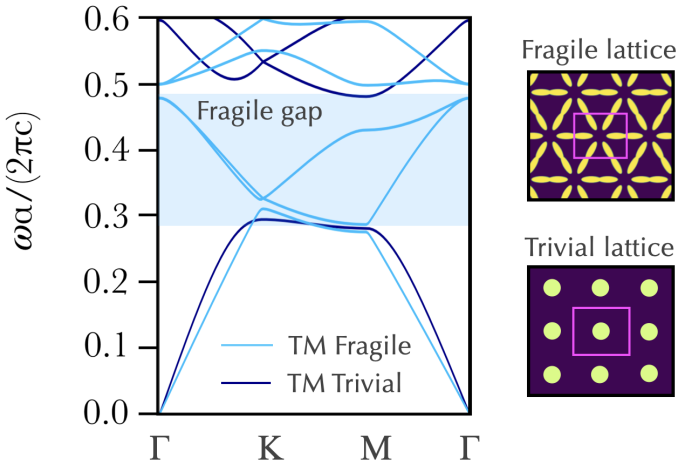

FIGURE 5.6: Band structure of the TM modes of the trivial and fragile phases. The bands corresponding to the trivial structure which are plotted in dark blue together while the light blue are the bands obtained from the periodic structure which shows fragile topology in the set formed by the second and the third band. The shaded area indicates the energy range where the fragile bands are located.

We define a super-cell composed by a repetition of twenty unit cells of the non-trivial phase in y-direction, followed by other twenty unit cells of the trivial phase in the same direction. Using MPB [73], we solve the macroscopic Maxwell's equation for this ribbon. Note that as we elongate the cell in real space along one spatial direction, the reciprocal space acquires a one-dimensional character since one of the reciprocal lattice vectors becomes smaller as one real space lattice vector is extended. The bands in the super cell are folded along this direction, showing a well defined set of bulk bands separated by gaps — as we show in left panel of Fig. 5.7. The shaded area of the figure corresponds to the frequency range where we are going to explore possible emergence of edge states since it coincides with the gap above the fragile bands. In the right panel of Fig. 5.7, we show the zoom in of this frequency range where we can observe the presence of two states (pointed by arrows) that seem to be hanging from the bulk bands.

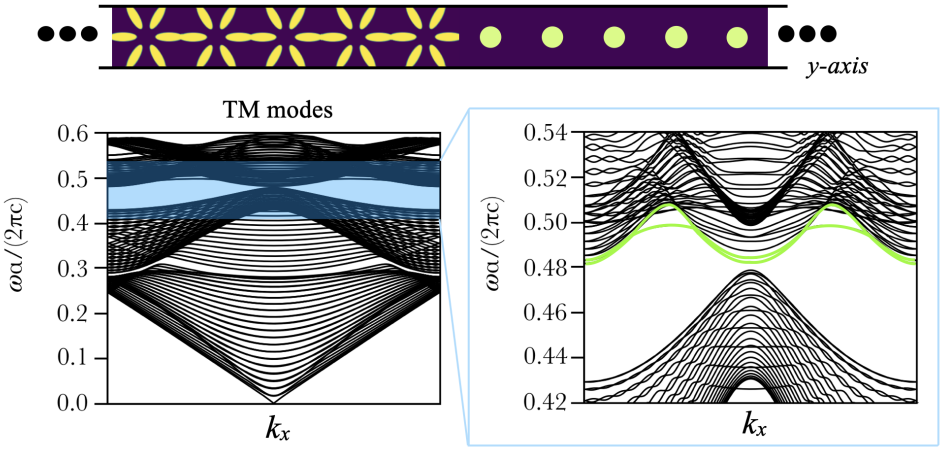

FIGURE 5.7: Schematic structure of the super-cell composed by twenty unit cells of trivial triangular array of cylinders and twenty unit cells of topological fragile triangular array of ellipses. The material of both topological phases is silicon ($\varepsilon = 11.7$) in air. Bellow, the left panel shows the bands along k_x, being the shaded area the gap correlated with the fragile bands. A zoom in of the shaded area is shown in the right panel. In this range can be observed a full band gap between well defined bulk of bands and two degenerate bands that seem hanging from the upper bulk marked in color lime.

Trying to detach those states from the upper bulk bands, we explore the effect of the progressive change of the dielectric constant in the fragile part of the super-cell. In each step, we increment by a value of 0.1 up to 12.7; we observe that for values of ε up to 12.4 the in-gap states are still connected to the upper

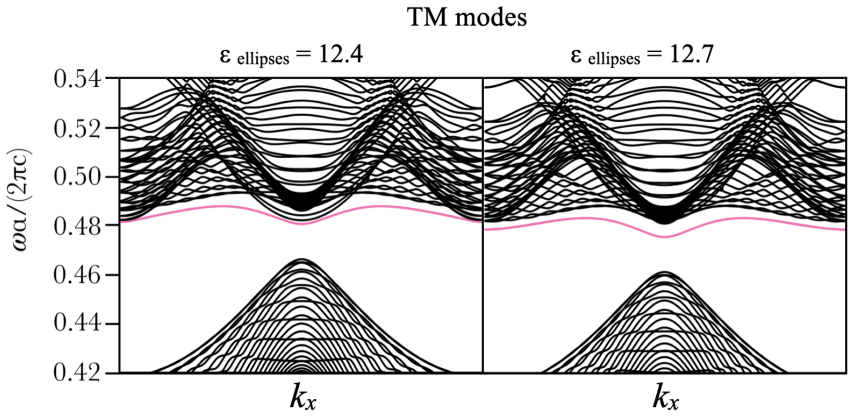

FIGURE 5.8: Band structure of the super-cell composed by twenty unit cells of trivial triangular array of silicon cylinders ($\varepsilon = 11.7$) in air, and twenty unit cells of topological fragile triangular array of ellipses. The left panel shows the bands along k_x for the ribbon composed by ellipses with $\varepsilon = 12.4$. The two degenerate bands in pink are edge states that are connected with the upper bulk of bands. In the right panel, the band structure correspond to a ribbon which contains ellipses with $\varepsilon = 12.7$. The pink bands are degenerate edge states that are placed completely into the gap.

FIGURE 5.9: Upper panel shows the ribbon structure composed by a trivial phase and a topologically fragile phase. Both lower panels correspond to the degenerate modes that exit within the gap.

bulk modes. However, for larger values of ε the in-gap states are completely detach from the upper bulk modes and are fully inside the gap of the system.

In order to characterize these two degenerate bands we plot the corresponding z component of the electric field at Γ to observe their profile along the ribbon. In Fig. 5.9 we show that the field is concentrate at the interface between the two phases with a well defined decay.

6 LDOS vs. Wannier functions

In Chapter 5 we applied different techniques to identify the topological character of several photonic crystals (PhCs) based on two dimensional (2D) artificial honeycomb lattices.

In this chapter, we combine the theory of topological quantum chemistry (TQC), the Wilson loop spectrum and the local density of states (LDOS) calculation to analyze the topological character of various PhCs which are based on an artificial honeycomb lattice. From this configuration, we expand and shrink the lattice to perform geometric adiabatic changes to the system. Then, we construct a PhC composed by a expanded and a shrunken lattice together. We show how changing the dielectric materials in such system we can design different topological phases.

6.1 Breathing honeycomb lattice

6.1.1 Model

In this section we characterize the topological properties of the breathing honeycomb PhC introduced by Wu and Hu in Ref. [48]. We define a two dimensional (2D) honeycomb lattice — being z the invariant direction — with an artificially enlarged unit cell. This non-primitive cell is composed by six silicon rods ($\varepsilon = 11.7$) of radius $r = 0.12a$ in vacuum ($\varepsilon = 1$), being a the lattice parameter. Each of those rods is located at a distance $R = R_0(1 \pm \delta)$ from the origin, where $R_0 = a/3$ is the location of the cylinders in the unperturbed honeycomb arrangement; and the parameter $\pm\delta$ quantifies the perturbation in the system which expand or shrink the lattice. While for positive values of δ the lattice is expanded, for negative values of δ the lattices is contracted — as is shown in Fig. 6.1.

The band dispersion of the TM modes in the unperturbed honeycomb lattice presents an artificial four-fold degeneracy at Γ caused by folding of the band structure due to the enlarged unit cell — center panel of Fig. 6.2. Then, we

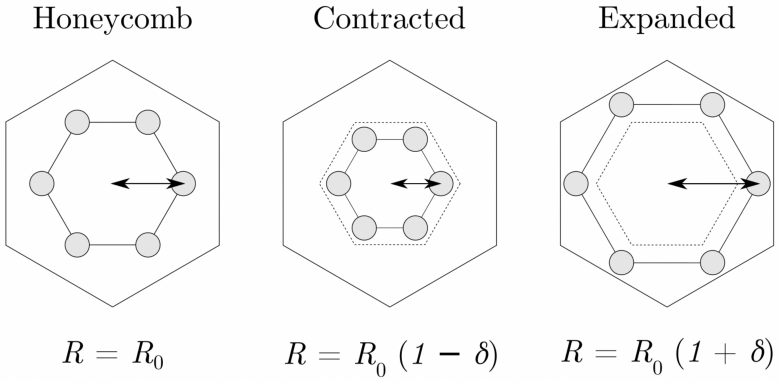

FIGURE 6.1: Non-primitive unit cell of the photonic breathing honeycomb lattice composed by six silicon rods ($\varepsilon = 11.7$) of radius $r = 0.12a$ in vacuum ($\varepsilon = 1$). *From left to right:* Unit cell of the unperturbed honeycomb lattice with the rods placed at a distance $R_0 = a/3$ from the origin. Unit cell of the contracted lattice whose cylinders are moved towards the center at a distance $R = R_0(1-\delta)$, being the perturbation $\delta = 0.11$. Unit cell of the expanded honeycomb lattice with the rods displaced to a distance $R = R_0(1+\delta)$ from the center, keeping the perturbation $\delta = 0.11$.

consider a perturbation of $\delta = \pm 0.11$, that moves the rods farther ($\delta = +0.11$) or closer ($\delta = -0.11$) from the center of the unit cell. The TM band structure of both perturbed lattices — right and left panel of Fig. 6.2 — shows the opening of a band gap between $\omega a/(2\pi c) = 0.4 - 0.5$, which indicates a non-adiabatic change in the system's response.

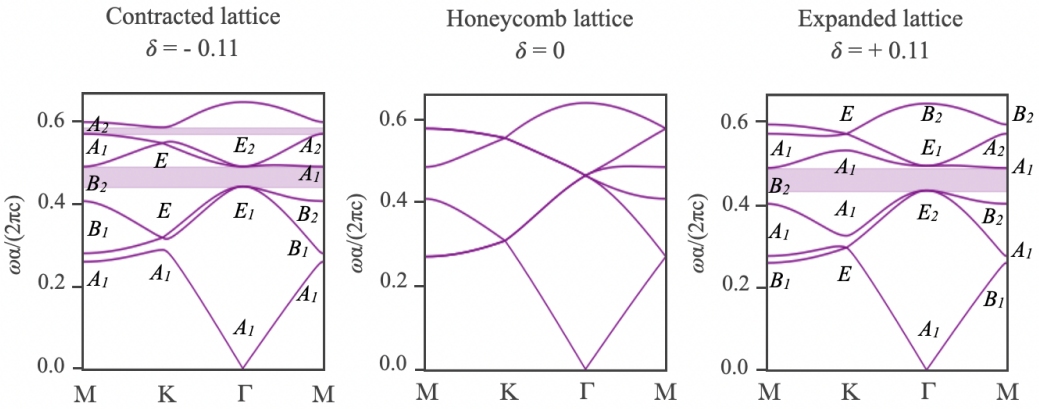

FIGURE 6.2: Band dispersion of the TM modes, *from left to right*, of the expanded, unperturbed and contracted lattices. The perturbation of the expanded and contracted lattice is $\delta = \pm 0.11$, respectively. For gaped systems, the shaded area indicates complete band gaps and, the *irrep* of each Bloch modes at high symmetry k-points are labeled inset.

6.1.2 Topological analysis

At first, we determine the topological properties of the system applying TQC. Fig. 6.2 shows the band structure of the expanded and contracted lattices together with the *irreps* of the Bloch modes at the high symmetry **k**-points, computed using GTPack [88, 89]. As we introduced in Chapter 5, we use the catalogue of Elementary Band Representations (EBRs) of the space group of the lattice (*p6mm*), found in the Bilbao Crystallographic Server [94–96], to characterize the topology of each gaped system. We summarize the relevant EBRs for the breathing honeycomb lattice in Table 6.1.

EBR	Γ	K	M
$(A_1 \uparrow G)_{1a}$	A_1	A_1	A_1
$(E_1 \uparrow G)_{1a}$	E_1	E	$B_1 \oplus B_2$
$(A_1 \uparrow G)_{3c}$	$A_1 \oplus E_2$	$E \oplus A_1$	$A_1 \oplus B_1 \oplus B_2$

TABLE 6.1: Relevant EBRs of *p6mm* for the lowest three bands of the photonic breathing honeycomb lattice.

For topologically trivial gaped systems, the Band Representation of connected bands can be expressed as linear combinations of these EBRs. Additionally, we can identify where the Wannier function that induces the connected bands is placed. For both gaped systems, the expanded and contracted lattice, we consider the three lowest energy bands for the corresponding analysis, which is shown in Table 6.2.

	Γ	K	M	EBR
Expanded	A_1, E_2	E, A_1	B_1, A_1, B_2	$(A_1 \uparrow G)_{3c}$
Contracted	A_1, E_1	A_1, E	A_1, B_1, B_2	$(A_1 \uparrow G)_{1a} \oplus (E_1 \uparrow G)_{1a}$

TABLE 6.2: Little group *irreps* for the three lowest bands of each phase. Together with the corresponding EBR for the contracted lattice, or sum of EBRs for the expanded lattice.

We can observe several band inversions comparing the band representation of both gaped lattices, as is shown in the band structures of Fig. 6.2. A band inversion is identified — for two bands cases — as the flipping of the *irreps* at certain high symmetry point between consecutive bands. The artificial unperturbed honeycomb lattice with $\delta = 0$, presents degeneracies that allow the mixing of the character between bands. Those artificial degeneracies are lifted perturbing the lattice with $\delta = \pm 0.11$, defining an expanded or contracted lattice respectively. The bands acquire a different character in the

high symmetry point of the degeneracy depending on the sign of the perturbation. In this case, we observe at Γ that the *irrep* of the bands 2 & 3 is E_1 for the contracted lattice and E_2 for the expanded. This indicates a different character of the Bloch modes in each structure for the lowest energy set of bands. At the K point instead, we observe that in the contracted case there is a degeneracy between bands 2 & 3 and band 1 is isolated. Alternatively, in the expanded lattice, bands 1 & 2 present a degeneracy while band 3 is non degenerate. Therefore, the *irreps* at the K point flip their character being A_1, E for the contracted case and E, A_1 for the expanded. Similarly, at the M point, the *irreps* of the bands 1 & 2 are flipped, being A_1, B_1 for the contracted lattice and B_1, A_1 for the expanded case.

For the contracted lattice we observe two sets of isolated bands, band 1 and bands 2 & 3, while for the expanded lattice we only observe one connected set formed by the three lowest bands. We now determine which EBRs form the band representation of each set of connected bands. These EBRs will give us information about the *irrep* of the Wannier function which induces the bands, as well as its location in real space, labelled by one of the maximal Wyckoff position.

Looking at the EBRs of the contracted lattice, we observe that the two sets of bands are induced from Wannier functions placed at the position $1a$ — which corresponds to the center of our real space unit cell. The lowest energy band is induced from a Wannier function of character A_1 and the second set is induced from Wannier functions of character E_1. For the expanded lattice instead, the three lowest energy bands form a connected set which is induced from a Wannier function that transforms under the *irrep* A_1 and is centered in the position $3c$ — the edge between two cells in our definition. Therefore, we can understand this two configurations as a 2D analogy of the 1D SSH chain [27]. In the case of the contracted lattice, the Wannier functions sit at the position $1a$. We call this limit the natural (atomic) limit. While in the case of the expanded lattice, the Wannier center is located between consecutive unit cells at the $3c$ position. This situation is refereed as the obstructed (atomic) limit (OAL[1]). Therefore, the obstructed phase has to be defined with respect to a natural limit. Nevertheless, as both limits admit exponentially localized Wannier representations, we can conclude that our system presents a trivial $\mathbb{Z}_2$ topological character.

[1] This topological phase was labeled in the past in analogy with solid-state systems as the photonic obstructed atomic limit (OAL).

Moreover, as in the previous chapter, we can characterize each system through the calculation of the Wilson loop spectrum for each set of connected bands, Fig. 6.3.

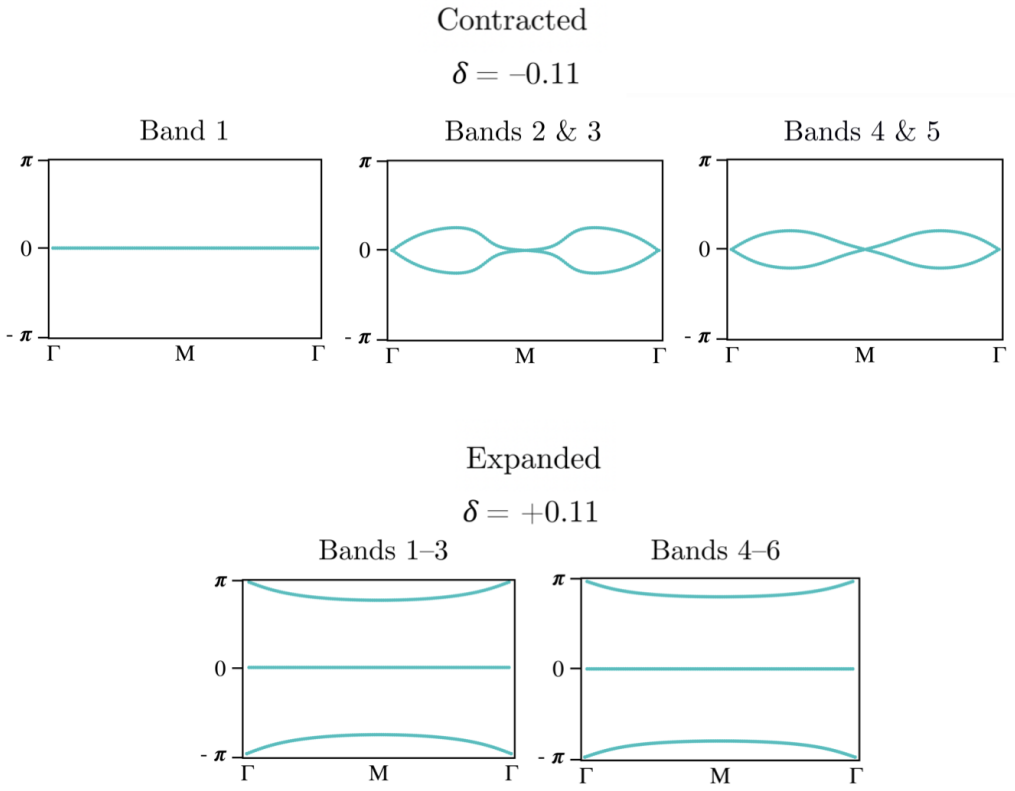

FIGURE 6.3: Wilson loop spectra along Γ- M -Γ of each set of connected bands. The lower part shows the spectrum of the set of bands for the contracted lattice, which indicates that the Wannier centers are trivially localized around the center of the unit cell. While, in the upper part we can observe the spectrum of the set of bands for the expanded lattice, which indicates that the Wannier centers as well localized at the edge of the unit cell, representing an obstruction phase of the trivial phase. Figure adapted from Supplemental Material of Ref. [102].

The resulting eigenvalues of the Wilson loop operator shown in Fig. 6.3, present no winding — which are characteristic of $\mathbb{Z}_2$ or Chern insulators — for all sets of bands in both structures. Nevertheless, we can observe that the localization of the Wannier centers is different for each lattice. For the contracted lattice ($\delta = -0.11$), we confirm that the Wannier centers are placed at the $1a$ maximal Wyckoff position, which is represented with eigenvalues pinned at 0 or around it. For the expanded lattice ($\delta = +0.11$), the eigenvalues are not exclusively localized in the origin of the unit cell as in the previous system. They are localized around its edges as well. We can observe that at Γ the eigenvalues are pinned at $\pm\pi$ which indicates a charge localization

shared between consecutive unit cells. The eigenvalues of the Wilson loop operator around $\pm\pi$ confirms that the Wannier centers are located at the $3c$ Wyckoff position, indicating that the system presents an obstruction similar to the 1D SSH chain.

In this chapter, we introduce an additional analysis tool through the calculation of the local density of states (LDOS) for each set of connected bands following the methodology described in Chapter 3. The maximum values of this real space function integrated over a set of connected bands, should correspond to the maximal Wyckoff position predicted by TQC for the Wannier center.

For the contracted lattice — right column of Fig. 6.4 — we observe that the LDOS in the first band is mostly concentrated inside the dielectric rods and pointing towards the position $1a$. To explore the LDOS outside the rods, we artificially set to zero the values of the LDOS in the dielectric regions by making $\varepsilon = 0$ in the calculation of the LDOS 3.22. The maximum of the LDOS in the air region forms a ring centered around the origin and connecting the dielectric rods. We observe a highly symmetric LDOS distribution which fits with the *irrep* (A_1) of the band's EBR — see Table 6.2.

The LDOS of the set of bands 2 & 3 shows a more precise localization of the maximimum inside the dielectric rods and a less symmetric shape. The maximum values of the LDOS presents an arc shape that connect non-equally all the rods. Comparing it with the LDOS of band 1, there is a clear lowering of the symmetry, as indicated by the different EBR of the bands — which specifically is induced with E_1 *irrep* in this case.

For the expanded lattice — top left panel of Fig. 6.4 — we observe that the LDOS for the set of the three lowest energy bands is localized inside the dielectric rods, but in this case pointing to the position $3c$. Observing the LDOS outside the rods, its maximum values connect dielectric rods from different unit cells (Wyckoff position $3c$). Moreover, we observe that the highly symmetric LDOS distribution fits as well with *irrep* A_1, as indicated by the EBR for this set of connected bands — see Table 6.2.

Since the contracted lattice is the trivial phase of the breathing honeycomb lattice, it represents the configuration that sets the natural atomic limit. In this configuration, the maximum of the LDOS in real space is located is around the center of the unit cell. For the expanded lattice instead, the maximum distribution is between consecutive unit cells. Therefore, this configuration

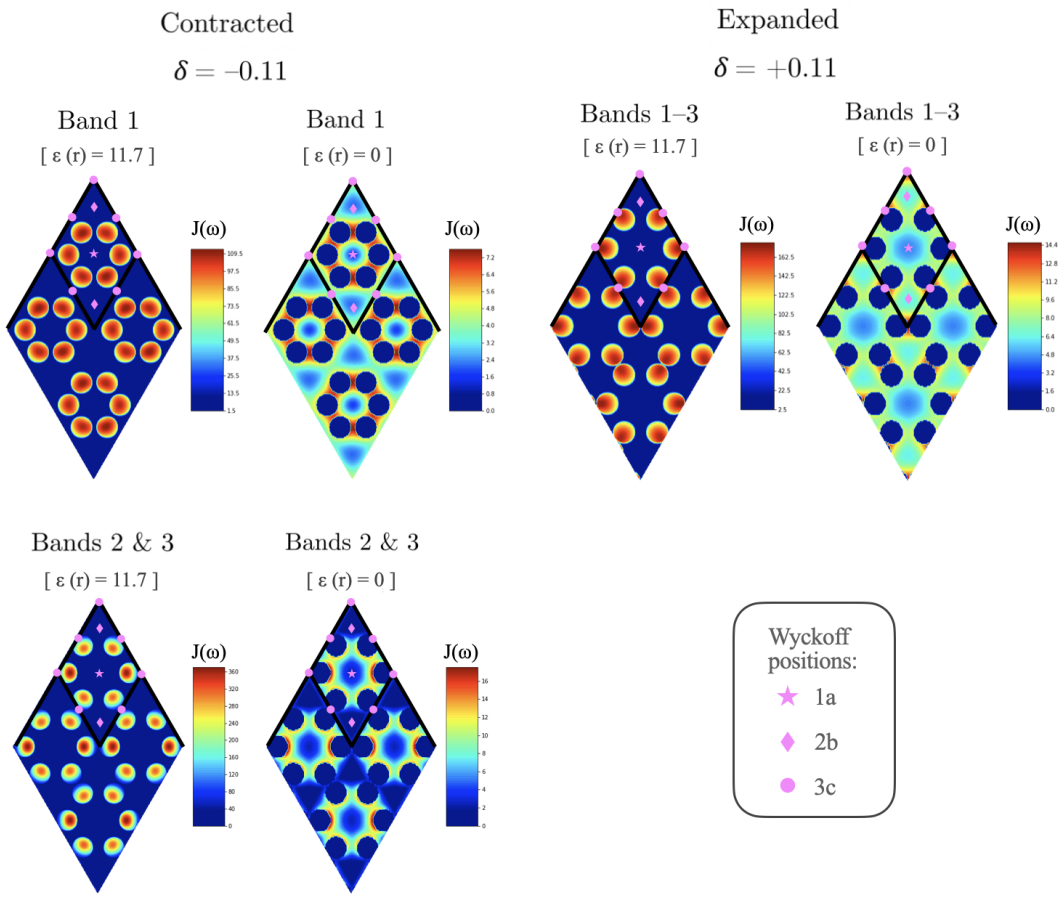

FIGURE 6.4: Transverse magnetic Local density of states (LDOS) considering the contribution of connected bands. For each set of bands, the LDOS calculation with $\varepsilon = 11.7$ is shown at the left side, and those with artificial $\varepsilon = 0$ at the right side. This procedure permits to resolve the LDOS distribution in the media, air in our case. Both of them are plotted in a supercell composed by four consecutive unit cells. The unit cell at the top of the super cell also includes an eye guide of the Wyckoff positions. The legend is shown in the bottom left panel. The panel above — top left — shows the LDOS of the set of bands $1-3$ for the expanded lattice, with a maximum of LDOS around the position $3c$.The right column, shows from top to bottom, the LDOS of the first band and the set of bands 2 & 3 for the contracted lattice. The maximum of both are placed within the dielectrics pointing towards the $1a$ position.

is the obstruction of the atomic limit, the 2D analog of the 1D SSH topological phase.

Although from the point of view of Wannier localization (TCQ and Wilson loop analysis) both lattices present a trivial topology, the obstructed phase can emulate some topological features. Since the charge is maximally localized at the edges and corners of the unit cell, it allows for the emergence of

symmetry protected localized modes which can present robustness against certain disorder [102].

6.2 Combined breathing honeycomb lattice

In this section, we explore the topological character of different photonic crystal whose unit cell is composed by twelve dielectric rods, six in the expanded positions and six in the contracted positions.

6.2.1 Model

These new structures are defined by a 2D triangular lattice with space group *p6mm*. As we mention above, the unit cell is composed by twelve dielectric rods; six of them are placed in the contracted honeycomb positions ($\delta = -0.11$), with radius $r = 0.05a$, while the rest, with radius $r = 0.1a$, take expanded honeycomb positions ($\delta = +0.11$). To explore different phases using this configuration, we vary the dielectric constant (ε). The different structures analyzed are shown in Fig. 6.5. For the structures contained in this section, we will use rods with two concrete dielectric values. Some rods will be made of $\varepsilon = 12$ (plotted in black) and the rest $\varepsilon = 4$ (plotted in grey).

As a starting point, we set $\varepsilon = 12$ for the smaller rods located closer to the center of the unit cell, and $\varepsilon = 4$ for the bigger rods, located closer to the edges — this structure is labelled as *Trivial* in Fig. 6.5 a.1). Since the contracted rods posses a higher ε, the maximum localization of the fields is expected around them. Looking at the spectrum of this structure, we observe three sets of connected bands separated by gaps. The band dispersion is shown in Fig. 6.5 a.2), where these isolated sets of bands are plotted in different colours.

We define the next structure setting $\varepsilon = 12$ for the bigger rods placed at the edges of the unit cell, and $\varepsilon = 4$ for the smaller rods around the center. This structure is labelled as *Obstructed* in Fig. 6.5 b.1). The maximum localization of the fields is now expected around the rods in expanded positions, as they posses the highest ε. In this case, the spectrum shows two set of bands separated by gaps, one for bands 1-3 and other for bands 4-6 — plotted with different colours in Fig. 6.5 b.2).

For the last structure, we define $\varepsilon = 12$ for all the rods. We label this structure as *Fragile* in Fig. 6.5 c.1). The band structure, presented in Fig. 6.5 c.2), shows a partial gap between the two lowest energy bands, being the lowest energy

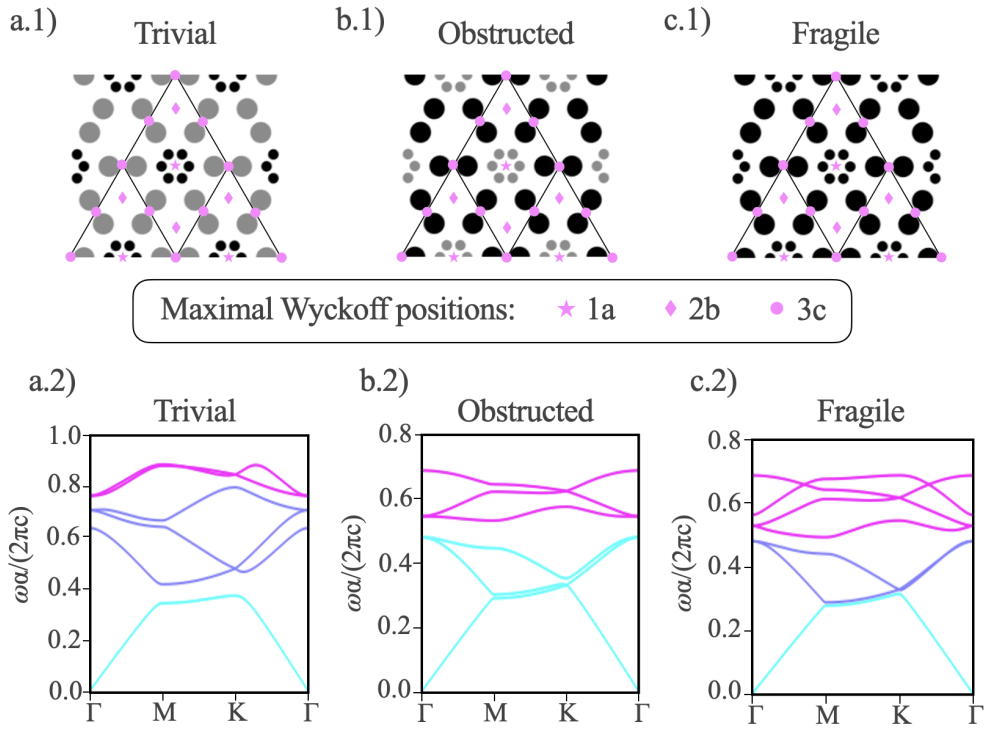

FIGURE 6.5: Top panels show different photonic crystals structures represented by four unit cells. Each unit cell is composed by six smaller dielectric rods of radius $r = 0.05a$ placed at contracted honeycomb positions and other six rods of radius $r = 0.1a$ placed at expanded honeycomb positions. Additionally, the maximal Wyckoff positions of the space group *p6mm* are labelled inset — with the correspond legend below. Setting different values of the dielectric constant (ε), black rods with $\varepsilon = 12$ and grey rods $\varepsilon = 4$, we get three different topological phases: trivial, a.1), obstructed atomic limit (OAL), b.1), and fragile, c.1). The spectrum of each phase is shown bellow. The sets of bands separated by gaps are plotted in different colours.

band fully isolated and the second band connected with the third. The set of bands 2 & 3 is separated by a full band gap from the following set of bands (bands 4-7).

In following sections, we determine the topological character of each system through Topological Quantum Chemistry, the eigenvalues of the Wilson loop operator and the LDOS calculation.

6.2.2 Trivial phase

Here, we analyze the topological character of the first structure described above — Fig. 6.5 a). In this case, we differentiate two set of connected bands: band 1 and bands $2-4$.

First, using the GT-Pack package in Mathematica, we analyze the symmetry representation of the Bloch modes at high symmetry **k**-points. The collection of all the *irreps* for each set of bands constitutes a BR. Then, we will proceed to analyze these BRs with respect to the EBRs of the space group *p6mm*. In this particular example, we can express all BRs of the structure as specific EBRs of *p6mm*, meaning that the band structure is induced from exponentially localized Wannier functions. The EBRs defining the first two sets of bands are collected in Table 6.3.

	Γ	K	M	EBR
Band 1	A_1	A_1	A_1	$(A_1 \uparrow G)_{1a}$
Bands 2-4	A_1, E_2	E, A_1	B_1, B_2, A_1	$(A_1 \uparrow G)_{3c}$

TABLE 6.3: Little group *irreps* for the set of lowest bands in the trivial structure; together with the corresponding EBR.

The EBR of the first band, $(A_1 \uparrow G)_{1a}$, indicates that such band is induced from a Wannier function maximally localized at the $1a$ Wyckoff position which transform under the A_1 *irrep*. The set of bands $2-4$, is induced from a Wannier function which transform with the same symmetry, A_1, but in this case maximally localized around the $3c$ position. The EBR which correspond to this set is $(A_1 \uparrow G)_{3c}$.

Additionally, we labelled the *irreps* in the band structure, shown in the left part of Fig. 6.6. At the right panel of Fig. 6.6 we show the density of states (DOS) of the band structure — calculated as described in Chapter 3 — and, we specify inset the EBR of each set of connected bands. Here, we observe the Van Hove singularities associated to the band structure. These singularities are related to k-points where the gradient of the bands goes to zero.

As we observed from the EBRs, the functions which induced the first band are maximally localized at the $1a$ Wyckoff position, while for bands $2-4$, they are localized at the $3c$ position. For the *p6mm* space group, these positions are located at the center or at the edge of the unit cell respectively. To support these results, we now compute the eigenvalues of the Wilson loop operator (see Fig. 6.7). For the first band the eigenvalues are constant and equal to zero. As there is no winding, the Wannier function is maximally localized which indicates a trivial character of the gap above. On the other hand, the value is related to the position where the function is placed. In this case, it correspond to the center of the unit cell.

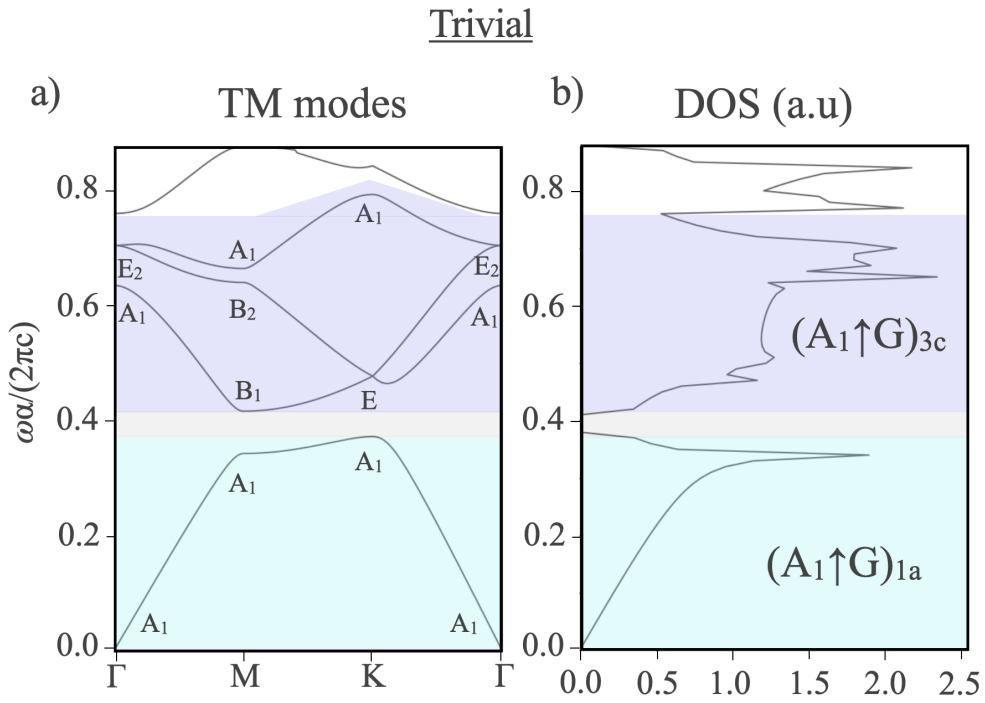

FIGURE 6.6: Symmetry analysis of the trivial phase. Panel a) shows the band structure for TM modes with the corresponding *irrep* of each Bloch mode at high symmetry **k**-points labelled inset. The color shaded area indicates different groups of connected bands. The color code is kept for in panel b), which shows the density of states (DOS) in arbitrary units. The correspond EBR of each set of bands is labelled inset.

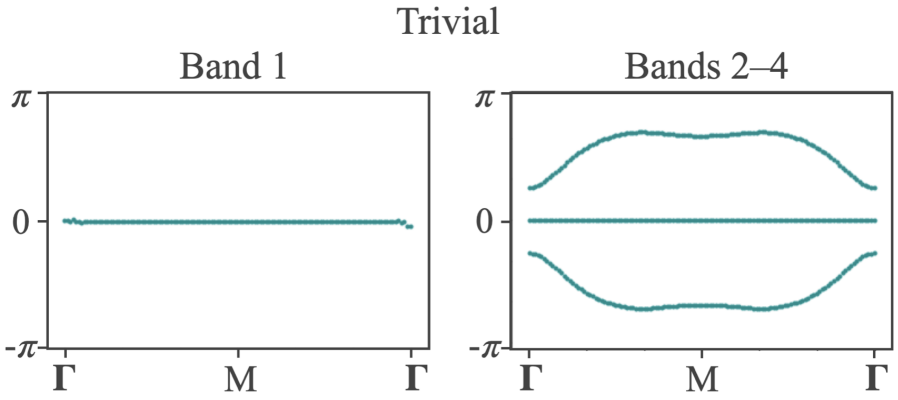

FIGURE 6.7: Wilson loop eigenvalues of the trivial phase. The Wilson loop spectra for the first band is plotted at the left side, and at the right size for the set of bands 2-4.

For the set of the bands $2-4$, we observe no winding in the spectrum of the Wilson loop operator which indicates a trivial topological character, meaning that these bands are induced from maximally localized Wannier functions.

Finally, we complete this analysis with calculations of the local density of

states (LDOS) for the different sets of bands — shown in Fig. 6.8. We perform the calculation considering $\varepsilon_{\text{cont.}} = 12$ and $\varepsilon_{\text{exp.}} = 4$ to see the actual LDOS within the unit cell. Complementary, we perform the calculation considering $\varepsilon = 0$ in Eq. 3.17 to explore the LDOS of the surrounding medium — air in our case. For clarity, the results are plotted in a larger cell formed by four unit cells where we label the Maximal Wyckoff positions — Fig. 6.8.

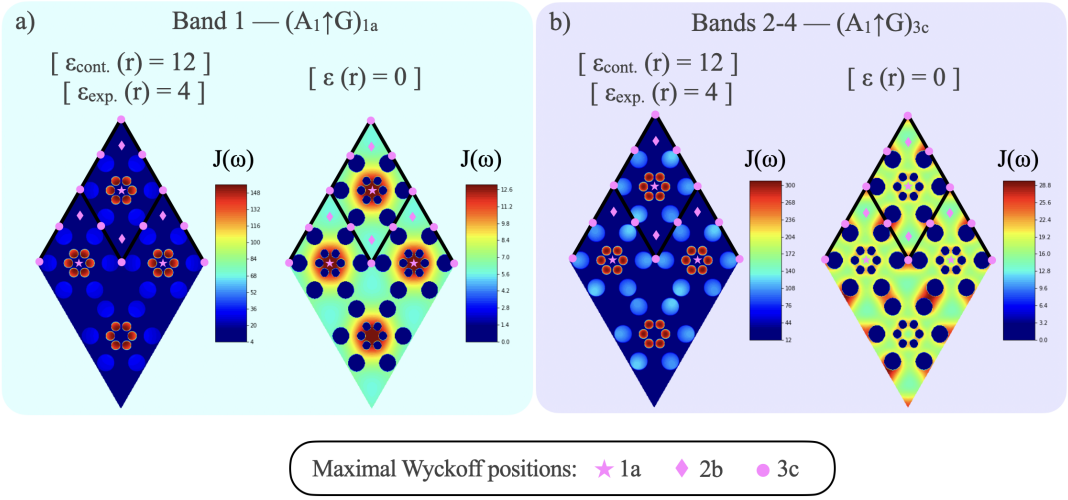

FIGURE 6.8: Transverse magnetic local density of states (LDOS) considering connected bands — labelled together with their EBR. The LDOS calculation with ($\varepsilon_{\text{cont.}} = 12, \varepsilon_{\text{exp.}} = 4$) is shown at the left side, and with $\varepsilon = 0$ at the right side. Both plotted in a supercell composed by four consecutive unit cells. Panel a) shows the LDOS of the first band which present the maximum localization around the center, the 1*a* position. Panel b) shows the LDOS of the set of bands 2-4, where the maximum is shared at the edges and corners of the unit cell, at the 3*c* position.

For the lowest band in energy — Fig. 6.8 a) — we observe that the maximum of LDOS is located inside the rods with higher ε placed at the contracted postions. Furthermore, the maximum LDOS is well localized around the center of the unit cell, the 1*a* Wyckoff position. Thus, there is a good correlation between the maximum of LDOS with the Wannier center position predicted by the EBR of the band.

For the set of bands $2-4$ — Fig. 6.8 b) — we observe again the highest LDOS inside the rods in the contracted positions. In this case, compared with the first band, we observe a higher concentration of LDOS within the rods at expanded positions. Looking at the LDOS of the medium, we observe some

concentration around the contracted rods but the maximum LDOS are located between consecutive unit cells, at the edges and corners which correspond with the 3*c* position. Although we observe the maximum LDOS concentration around the center due to the higher ε, the LDOS of the medium clearly support the prediction of TQC indicating that the Wannier center of the function that induce this set of bands is placed at the 3*c* position.

6.2.3 Obstructed phase

Next we analyze the opposite structure, the one with the rods of higher ε placed at the expanded honeycomb positions — see Fig. 6.5 b). In this case, we identify two sets of connected bands — bands $1-3$ and bands $4-6$ — that we will characterize independently. In Fig. 6.9 we show the band structure with the *irreps* at every high symmetry point. Additionally, we compute the corresponding DOS — shown at the right side of Fig. 6.9.

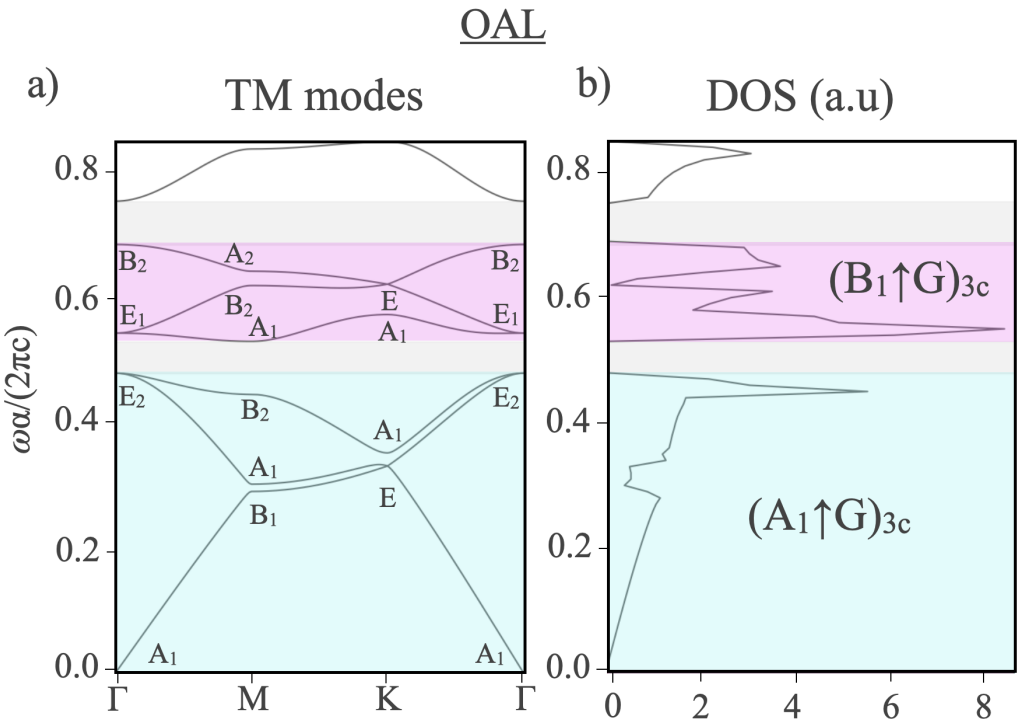

FIGURE 6.9: Symmetry analysis of the obstructed phase — OAL. Panel a) shows the band structure for TM modes with the corresponding *irrep* of each Bloch mode at high symmetry **k**-points labelled inset. The color shaded area indicates different groups of connected bands. The color code is kept for in panel b), which shows the density of states (DOS) in arbitrary units. The correspond EBR of each set of bands is labelled inset.

We can now define the band representation of each set of bands, and relate them with the EBRs of the space group *p6mm*. We summarize the results in Table 6.4.

	Γ	K	M	EBR
Bands 1-3	A_1, E_2	E, A_1	B_1, A_1, B_2	$(A_1 \uparrow G)_{3c}$
Bands 4-6	E_1, B_2	A_1, E	A_1, B_2, A_2	$(B_1 \uparrow G)_{3c}$

TABLE 6.4: Little group *irreps* for the set of lowest bands in the obstructed limit structure; together with the corresponding EBR.

The first set, composed by bands $1-3$, is induced from Wannier functions centered at the $3c$ Wyckoff position that transform under the *irrep* A_1. The Wannier function that induces the set of bands $4-6$ is centered the $3c$ position as well, but it is transformed under a different *irrep* of the space group, B_1.

We now confirm these results by looking at the Wilson loop spectrum (Fig. 6.10).

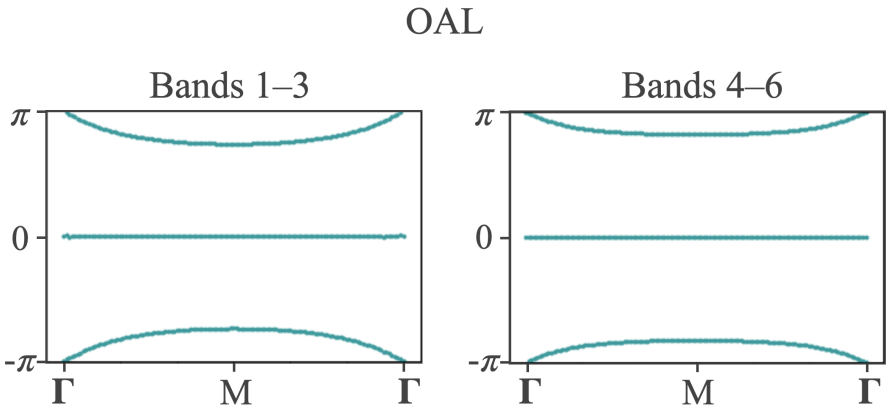

FIGURE 6.10: Spectrum of the Wilson loop operator for the sets of bands 1-3 and bands 4-6 corresponding to the obstructed phase.

For both set of bands we observe that the eigenvalues of the Wilson loop operator present no winding, indicating a trivial character. Nevertheless, the eigenvalues are located around $\pm\pi$ which indicates that the expectation value of the Wannier function is located between consecutive unit cells. Therefore, this structure is characterized as an obstructed atomic limit (OAL) phase. Despite OAL phases could present features associated to topological effects as corner and/or edge modes with some protection due to the lattice

symmetries, the protection against disorder is not as robust as for topological states.

We continue the characterization by exploring the LDOS integrated over the sets of connected bands (Fig. 6.11).

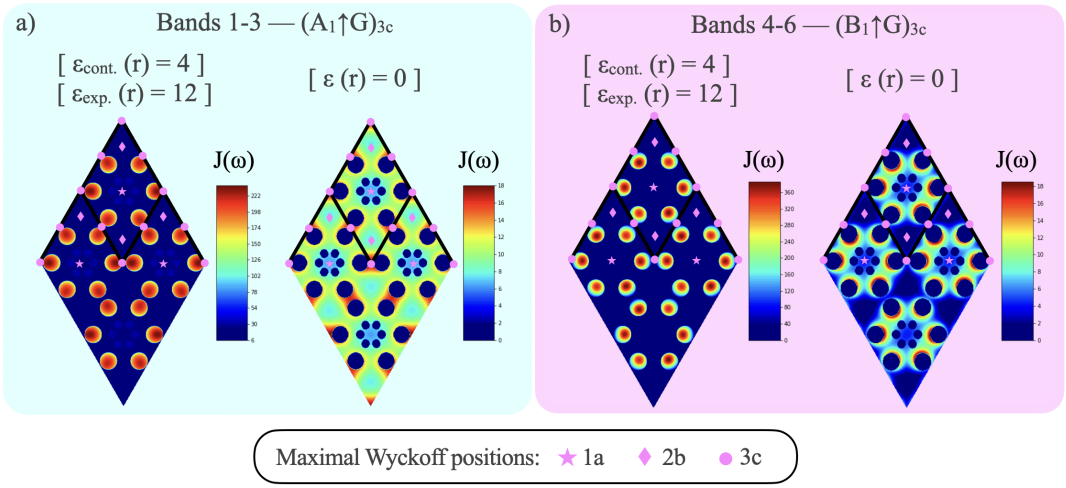

FIGURE 6.11: Transverse magnetic local density of states (LDOS) for bands separated by gaps, labelled together with the corresponding EBR. The LDOS calculation with ($\varepsilon_{\text{cont.}} = 4, \varepsilon_{\text{exp.}} = 12$) is shown at the left side, and with $\varepsilon = 0$ at the right side. Both plotted in a supercell composed by four consecutive unit cells. Panel a) shows the LDOS of the bands $1-3$ which present the maximum localization around the $3c$ position, shared at the edges and corners of the unit cell. Panel b) shows the LDOS of the set of bands $4-6$, where the maximum is placed at the rods in the expanded positions, close to the $3c$ position but oriented to the center.

The LDOS of the set of bands $1-3$, shows a clear localization at the rods with higher dielectric constant with the maximum values oriented towards the edges of the unit cell. This observation is found as well for the medium. Therefore, we observe for this bands a good correlation between the predicted position of the Wannier centers ($3c$) with the position of our maximum values of LDOS. For the set of bands $4-6$, we observe again the maximum within the rods with higher ε placed at the expanded honeycomb positions. Compared with the previous set of bands, in this case the localization inside the rods is more defined and oriented to the center of the unit cell.

6.2.4 Fragile phase

Last, we analyze the lattice composed by rods in expanded and contracted positions with $\varepsilon = 12$ — as shown in Fig. 6.5 c). For this structure, we distinguish three set of bands: the first band isolated from the next set of bands 2 & 3 by a partial gap, and the set of bands $4-7$ separated by a complete gap. We extract the EBR of each set of bands looking at their correspond band representation. Such representation is constructed computing the *irreps* of the Bloch modes at the high symmetry **k**-points — labeled inset the band structure shown in Fig. 6.12 a). We summarize the band representation

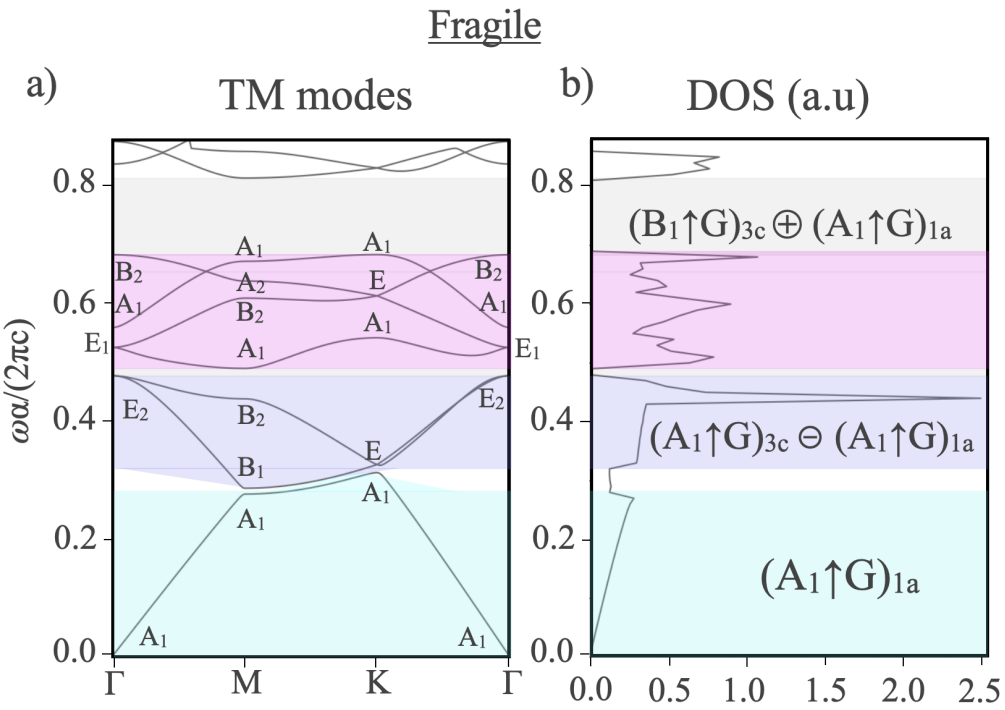

FIGURE 6.12: Symmetry analysis of the fragile phase. Panel a) shows the band structure for TM modes with the corresponding *irrep* of each Bloch mode at high symmetry **k**-points labelled inset. The color shaded area indicates different groups of connected bands. The color code is kept for in panel b), which shows the density of states (DOS) in arbitrary units. The correspond EBR of each set of bands is labelled inset. In this case the band representation of the set of bands 2 & 3 — in increasing energy order — can be expressed as a subtraction of EBRs.

of each set of connected bands in Table 6.5. We include as well their corresponding EBRs of the space group *p6mm*. For this case, we observe that the set of bands 2 & 3 can only be expressed as a subtraction of EBRs indicating a fragile topological character. The sets of band 1 and bands $4-7$, present

trivial character since their band representation can be expressed as an EBR and sum of EBRs, respectively.

	Γ	K	M	EBR
Band 1	A_1	A_1	A_1	$(A_1 \uparrow G)_{1a}$
Bands 2 & 3	E_2	E	B_1, B_2	$(A_1 \uparrow G)_{3c} \ominus (A_1 \uparrow G)_{1a}$
Bands 4-7	E_1, A_1, B_2	A_1, E, A_1	A_1, B_2, A_2, A_1	$(B_1 \uparrow G)_{3c} \oplus (A_1 \uparrow G)_{1a}$

TABLE 6.5: Little group *irreps* of the lowest bands for the structure with fragile bands. The band representation is expressed in terms of EBR of the space group *p6mm* in the last column.

In Fig. 6.12 b), we show the DOS of this structure with the corresponding EBR of each set of bands. TQC predicts that the Wannier function which induces the first band is centered in the $1a$ maximal Wyckoff position; while the sets of bands 2 & 3 and bands $4-7$, are induced from a function that transforms respectively as a subtraction or a sum of EBRs centered at $3c$ and $1a$. Therefore, we explore the eigenvalues of the Wilson loop operator — shown in Fig. 6.13 — to get information of the expectation position of the Wannier function within the unit cell.

The Wilson loop spectrum of the lowest energy band shows a constant zero value which indicates that the Wannier function associated to this band is exponentially localized at the center of the unit cell, the $1a$ Wyckoff position. For the set of bands 2 & 3, we get eigenvalues of the Wilson loop operator that wind from π to $-\pi$ and from $-\pi$ to π. This spectrum indicates that the Wannier functions that induce the bands are not exponentially localized at any position of the unit cell, indicative of non-trivial topology. As we explained in previous chapters, this is the representative spectrum of $\mathbb{Z}_2$ insulators. Fragile topology can be distinguished from a $\mathbb{Z}_2$ topological phase by adding a trivial band to the calculation. While the $\mathbb{Z}_2$ phase preserves the winding, the fragile phase becomes trivial instead — with no winding in the Wilson loop spectrum[2]. The last spectrum, corresponding to the bands $4-7$, shows values with no winding centered around $\pm\pi$ and 0, which indicates that the Wannier function is exponentially localized around the edge ($3c$ position) and the center ($1a$ position) of the unit cell.

We conclude the analysis computing the LDOS integrated over the different sets of bands, which allows to explore the correlation with the predicted positions of Wannier functions that induce each set.

[2]Note that we do not consider relevant to include this calculation of the Wilson loop spectrum for bands $1-3$ together for this case since this test was already included in Chapter 5 for bands with identical symmetry representation and topological properties.

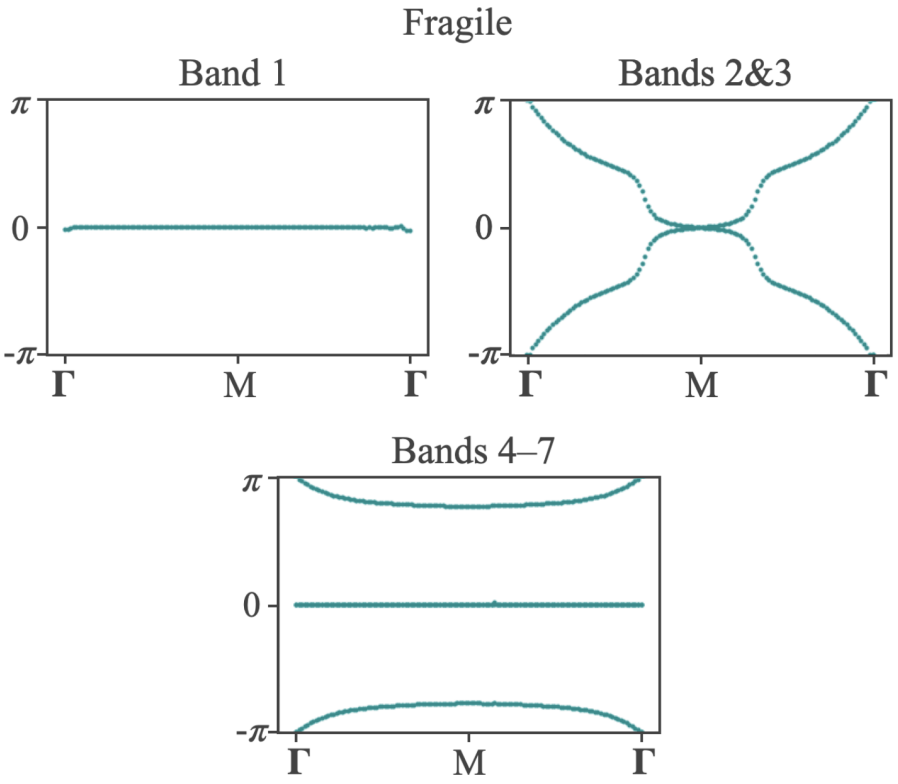

FIGURE 6.13: Wilson loop spectrum. The sets of band 1 and bands 4-7 shows no winding indicating trivial character, while the set of bands 2 & 3 shows two winding with opposite slopes which indicates fragile topology.

For the first band — Fig. 6.14 a) — we observe the maximum LDOS at the dielectric rods in contracted positions while in the medium, the maximum LDOS is concentrated around the center of the unit cell — the 1*a* position.

The LDOS for the set of bands 2 & 3 — Fig. 6.14 b) — shows higher values within the rods in expanded positions oriented to the adjacent unit cells while the lowest values are within the rods in contracted positions. The same distribution is observed for the LDOS in the medium. The LDOS of the last set of bands $4-7$ — Fig. 6.14 c) — shows the maximum values centered in the rods placed at expanded positions and lower values for those placed in the contracted positions. While the media shows a clear maximum in the center of the unit cell and around the expanded rods pointing towards the center — the 1*a* position.

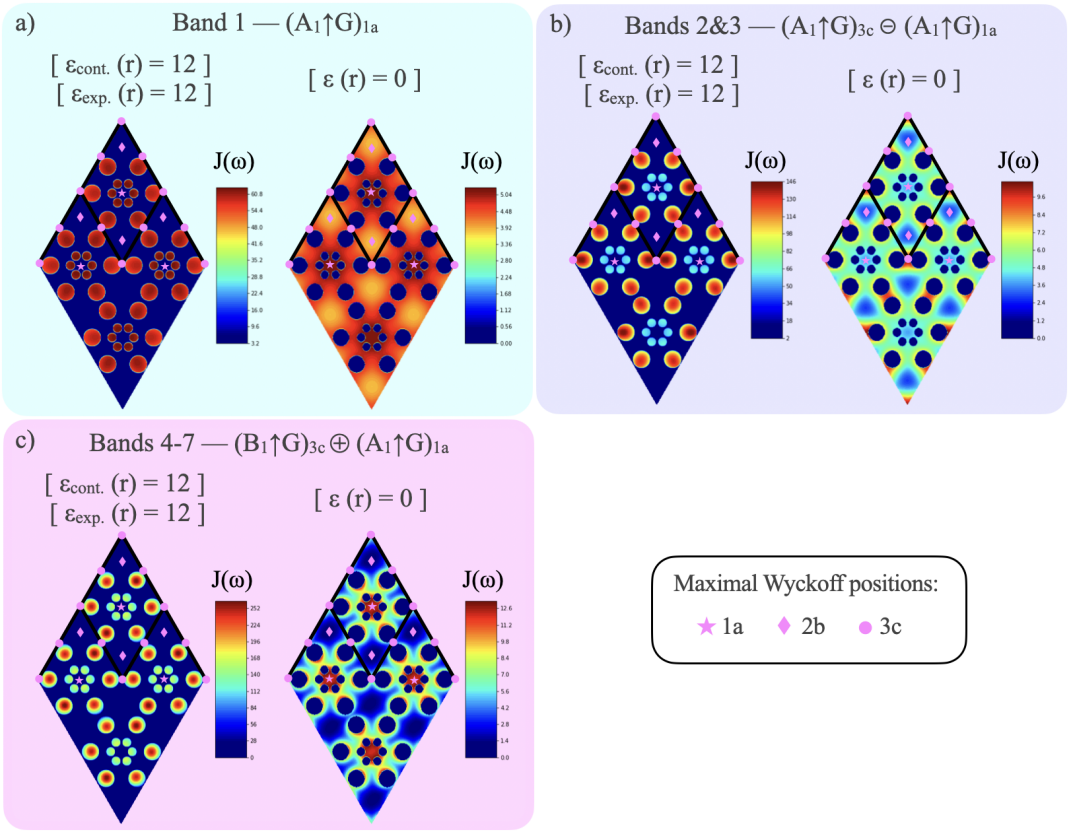

FIGURE 6.14: Transverse magnetic local density of states (LDOS) for different set of bands isolated by gaps — labelled together with the corresponding EBR. The LDOS calculation with ($\varepsilon_{\text{cont.}} = 12, \varepsilon_{\text{exp.}} = 12$) is shown at the left side, and with $\varepsilon = 0$ at the right side. Both plotted in a supercell composed by four consecutive unit cells. Panel a) shows the LDOS of the first band which present the maximum localization around the center of the unit cell, 1*a* position. Panel b) shows the LDOS of the set of bands 2 & 3 which posses fragile topology, the maximum is placed inside the rods placed at the expanded positions with shared charge between consecutive unit cells in the media. Panel c) shows the LDOS of the set of bands 4-7, where the maximum is placed at the rods in the expanded positions while in the media is mostly centered around the center of the unit cell.

7 Conclusions

This thesis focused on the topological characterization of 2D photonic crystals. The first introductory chapter was dedicated to explain in brief how the study of topological effects emerged both in electronic and photonic systems. The chapter highlighted the most relevant examples of topological phases, putting a special emphasis on classical systems. The theoretical background of the calculations used along this thesis was provided in Chapter 2. The first part of the chapter was dedicated to the description of the considerations needed to transform the macroscopic Maxwell's equations into the eigenvalue problem that describes the propagation of light within a photonic crystal. The second part of Chapter 2 introduced the theoretical expressions in the continuum limit for the physical quantities associated to the computation of topological invariants in periodic systems. These invariant quantities of interest are the Berry curvature, the Berry phase, and the Berry connection as well as the Chern and valley Chern number, and the eigenvalues of the Wilson loop operator. In the chapter, we introduced the connection between the Wilson loop operator and the position of the Wannier centers. These concepts are essential in order to understand topology within the framework of Topological Quantum Chemistry (TQC). The final part of Chapter 2 introduced the mathematical formalism necessary to calculate the photonic density of states (DOS) and local density of states (LDOS) of photonic crystal structures.

In Chapter 3, we presented the discrete expressions of the theoretical concepts shown in Chapter 2, providing a practical description of the computational methods used throughout this thesis. In the first part of the chapter, we explained how to compute the Berry phase and Berry curvature using an *ad hoc* discretization of reciprocal space, and how this quantities are essential for the numerical calculation of the Chern and valley-Chern numbers. The following numerical method described in Chapter 3 is the calculation of the Wilson loop spectrum including the numerical considerations needed to properly impose the periodicity of the photonic crystal in reciprocal space. Then, Chapter 3 continues describing how TQC can be applied to photonic crystals in order to assets the topology of photonic band structures. The last part of

the chapter focuses on the numerical calculation of the DOS and LDOS in photonic crystals. Moreover, this section introduced an integrated expression of the LDOS, which we used to visualize the location of the predicted Wannier functions by TQC in Chapter 6.

The following Chapters were focused on practical implementations of different topological photonic systems, and their analysis. Chapter 4 presents several Photonic Crystals with different topological characters: a Chern insulator, a system with valley degree of freedom, an obstructed atomic limit (OAL) system and a system hosting fragile topological bands. Here, we explained the distinctive features of the obtained results for each topological phase. Although the fragile phase and the OAL are first introduced in Chapter 4, both phases are explained in depth in the successive chapters.

Chapter 5 focused mostly on the fragile phase. Here we started by describing the symmetry group of 2D hexagonal lattices (*p6mm*) and from here, we detail necessary steps to perform a topological assessment using TQC. Beside, we complemented the analysis of fragile topology using the eigenvalues of the Wilson loop operator for an example Photonic Crystal and explored the manifestation of edge states on finite-sized super-cells combining trivial and fragile topological photonic systems.

Finally, Chapter 6 is dedicated to the exploration of the relationship between the charge concentration in real space and the predictions made by TQC. In particular, we analyzed a crystal combining two breathing honeycomb lattices. In particular, we compared the LDOS calculations to the Wannier center positions predicted by TQC. Moreover, the chapter explained the main features of OAL phase and why OAL systems can be easily confused with topological phases.

To summarize, this thesis introduced a systematic way to characterize the topology of 2D photonic crystals. We provided strategies to compute topological invariants such as the Chern number, the valley-Chern number and the eigenvalues of the Wilson loop operator. Additionally, we introduced for the first time the application of TQC to photonic crystals and we show its utility for an efficient topological characterization of photonic band structures.Finally, we established a correspondence between the LDOS distribution of sets of connected bands and the position of the Wannier centers predicted by TQC and Wilson loop spectra.

All these instruments permit to analyze the topological character of photonic

topological structures in-depth. Last but not least, this tool-set allowed us to design the first known physical implementation of a fragile topological system to that date.

A Appendix A: Green's function for photonic crystals.

As we described in section 2.1, the operator of the eigenvalue problem expressed as a function of the electric modes Eq. (2.7) is not Hermitian. Hence, it is not straightforward to investigate the completeness and orthogonality of the solutions in this form. Instead the equation can be re-written as

$$\nabla \times \mathbf{H}(r) = -i\omega\sqrt{\varepsilon(r)}\mathbf{C}(r)\,, \tag{A.1}$$

with $\mathbf{C}(r) = \sqrt{\varepsilon(r)}\mathbf{E}(r)$. This re-arrangement allows a symmetric form of vector field $\mathbf{C}(r)$ equation. Therefore, we have

$$\nabla \times \nabla \times \frac{1}{\sqrt{\varepsilon(r)}}\mathbf{C}(r) = \left(\frac{\omega}{c}\right)^2 \sqrt{\varepsilon(r)}\mathbf{C}(r)\,. \tag{A.2}$$

Finally, the electric vector field is derived in terms of a fully symmetric Hermitian operator as

$$\frac{1}{\sqrt{\varepsilon(r)}}\nabla \times \nabla \times \frac{1}{\sqrt{\varepsilon(r)}}\mathbf{C}(r) = \left(\frac{\omega}{c}\right)^2 \mathbf{C}(r)\,. \tag{A.3}$$

The operator on the left hand side, H_E, is a Hermitian operator for the electric vector field. Following the identity holds for H_E

$$\int dv\ \mathbf{E}_2^*(r) \cdot H_E[\mathbf{E}_1(r)] = \int dv\ \mathbf{E}_1(r) \cdot H_E[\mathbf{E}_2^*(r)]\,. \tag{A.4}$$

Which means that $\langle \mathbf{E}_2 |\, H_E \,| \mathbf{E}_1 \rangle = \langle \mathbf{E}_1 |\, H_E \,| \mathbf{E}_2 \rangle^*$ proving that H_E is indeed, a Hermitian operator.

Due to the periodicity of the permittivity in PCs, the formal solutions of the eigenproblem have the form of Bloch modes with a momentum in the first

BZ, that read as Eq. (2.9b).

Note that while n is an integer counting the discrete bands, as one expects from a discrete spectrum of a Hermitian operator, the $\mathbf{k}$-wavevector is a continuous variable in the BZ.

There are two types of orthogonality with this basis. On one hand, the modes of a given $\mathbf{k}$-vector at different bands are orthogonal to each other since the spectrum is discret in momentum due to the hermicity of the operator. On the other hand, in each n-band the modes with different $\mathbf{k}$-vectors are orthogonal to each other, too.

Therefore, we get

$$\int_{\mathrm{UC}} dv\, \varepsilon(\mathbf{r}) \mathbf{E}^*_{kn}(\mathbf{r}) \cdot \mathbf{E}_{k'n'}(\mathbf{r}) = \delta_{nn'}\delta(k-k')\,, \tag{A.5}$$

where the overlap integral is evaluated over the UC.

Using $\mathbf{C}_{kn}(r)$, the identity at each Bloch $\mathbf{k}$-wavevector can be spanned as

$$\int_{\mathbf{k}} d\mathbf{k} \sum_n \mathbf{C}_{kn}(r) \otimes \mathbf{C}^*_{kn}(r') + \mathbf{C}^L_{kn}(r) \otimes \mathbf{C}^{L*}_{kn}(r') = \mathbb{I}_2 \delta(r-r')\,, \tag{A.6}$$

where $\mathbb{I}_2$ indicate the identity tensor of dimension 2 and the superscript L refers to the longitudinal subspace used as basis of H_E.

Finally, in terms of the electric field we get

$$\int_{\mathbf{k}} d\mathbf{k} \sum_n \mathbf{E}_{kn}(r) \otimes \mathbf{E}^*_{kn}(r') + \mathbf{E}^L_{kn}(r) \otimes \mathbf{E}^{L*}_{kn}(r') = \mathbb{I}_2 \frac{\delta(r-r')}{\varepsilon(r)}\,. \tag{A.7}$$

From the hermitian electric field eigenproblem – Eq. (A.3) – it is clear to see that the Green's tensor $\mathbf{G}$ satisfies the following equation

$$\left[\frac{1}{\varepsilon(r)}\nabla\times\nabla\times - \left(\frac{\omega}{c}\right)^2\right]\mathbf{G}(r,r') = \mathbb{I}_2 \frac{\delta(r-r')}{\varepsilon(r)}\,. \tag{A.8}$$

Combining the last two equations – Eq. (A.7) and Eq. (A.8) – one gets the subsequent equality,

$$\left[\frac{1}{\varepsilon(r)}\nabla\times\nabla\times-\left(\frac{\omega}{c}\right)^2\right]\mathbf{G}(r,r')=\int_{\mathbf{k}}d\mathbf{k}\sum_n\mathbf{E}_{kn}(r)\otimes\mathbf{E}^*_{kn}(r')+\mathbf{E}^L_{kn}(r)\otimes\mathbf{E}^{L*}_{kn}(r')\,. \tag{A.9}$$

To find the Green's function expression, one needs to apply the following operator on both sides of Eq. (A.9),

$$L_i=\left[\frac{1}{\varepsilon(r)}\nabla\times\nabla\times-\left(\frac{\omega}{c}\right)^2\right]^{-1}, \tag{A.10}$$

where L_i only acts on $\mathbf{r}$.

On one side, from the spectral solutions of Eq. (A.3) we have

$$\frac{1}{\varepsilon(r)}\nabla\times\nabla\times\mathbf{E}_{kn}(r)=\left(\frac{\omega_{kn}}{c}\right)^2\mathbf{E}_{kn}(r)\,. \tag{A.11}$$

Therefore, we get

$$L_i[\mathbf{E}_{kn}(r)]=\frac{c^2}{\omega_{kn}^2-\omega^2}\,\mathbf{E}_{kn}(r)\,. \tag{A.12}$$

Furthermore, since the longitudinal modes are basis of the H_E subspace, the expression

$$\frac{1}{\sqrt{\varepsilon}(r)}\nabla\times\nabla\times\frac{1}{\sqrt{\varepsilon}(r)}\mathbf{C}^L_{kn}(r)=0\,, \tag{A.13}$$

is satisfied, which is equivalent to

$$\nabla\times\nabla\times\mathbf{E}^L_{kn}(r)=0\,. \tag{A.14}$$

Hence, we get

$$L_i[\mathbf{E}^L_{kn}(r)]=-\frac{c^2}{\omega^2}\mathbf{E}^L_{kn}(r)\,. \tag{A.15}$$

Finally, the Green's tensor equation, after applying L_i to the both sides, becomes

$$\mathbf{G}(r,r';\omega) = \int_{\mathbf{k}} d\mathbf{k} \sum_n \frac{c^2}{\omega_{kn}^2 - \omega^2} \mathbf{E}_{kn}(r) \otimes \mathbf{E}_{kn}^*(r') - \frac{c^2}{\omega^2} \mathbf{E}_{kn}^L(r) \otimes \mathbf{E}_{kn}^{L*}(r') \,. \tag{A.16}$$

Rearranging Eq. (A.7) we get,

$$\int_{\mathbf{k}} d\mathbf{k} \sum_n \mathbf{E}_{kn}^L(r) \otimes \mathbf{E}_{kn}^{L*}(r') = \mathbb{I}_2 \frac{\delta(r-r')}{\varepsilon(r)} - \int_{\mathbf{k}} d\mathbf{k} \sum_n \mathbf{E}_{kn}(r) \otimes \mathbf{E}_{kn}^*(r') \,. \tag{A.17}$$

Finally, by plugging Eq. (A.17) into Eq. (A.16), an analytical expression for the Green's tensor $\mathbf{G}(r,r';\omega)$ is obtained:

$$\mathbf{G}(r,r';\omega) = \int_{\mathbf{k}} d\mathbf{k} \sum_n \frac{c^2\omega_{kn}^2}{\omega^2\left(\omega_{kn}^2 - \omega^2\right)} \mathbf{E}_{kn}(r) \otimes \mathbf{E}_{kn}^*(r') - \left(\frac{c}{\omega}\right)^2 \frac{\delta(r-r')}{\varepsilon(r)} \mathbb{I}_2 \,. \tag{A.18}$$

Where the last term, is a real quantity proportional to the identity tensor $\mathbb{I}_2$.

B Appendix B: Symmetry properties of Wilson loops.

First note that our photonic crystals shown in Chapter5, have both C_2 rotation and time reversal (T) symmetries. The combined symmetry C_2T is antiunitary, and leaves all $\mathbf{k}$ points invariant. Since each projector $P(\mathbf{k})$ is C_2T invariant, the net effect of this symmetry on the Wilson loop is to take $W(\mathbf{k}_1)$ to itself. Imposing this symmetry, and recalling that it is antiunitary, we deduce that $W(\mathbf{k})$ and $W^*(\mathbf{k})$ must have the same spectrum. The phases θ_i thus come in pairs $\{\theta_i, -\theta_i\}$, or else $\theta_i = 0, \pi$. If we compute this Wilson loop for a single isolated band, it must have either $\theta = 0$ or $\theta = \pi$.

In the case of one or two occupied bands, we can determine $\{\theta_i\}$ solely from the eigenvalues of C_2 symmetry at Γ and M. To see this, let us consider first $W(0)$. Starting with the definition Eq. (3.15) and splitting the product in half, we find

$$W(0) = \langle u_{m,(0,\pi)}| \prod_{k2}^{\pi\leftarrow -\pi} P(0,k_2)|u_{n,(0,-\pi)}\rangle \tag{B.1}$$

$$= \langle u_{m,(0,\pi)}| \prod_{k2}^{\pi\leftarrow 0} P(0,k_2)|u_{\ell,(0,0)}\rangle\langle u_{\ell,(0,0)}| \prod_{k2}^{0\leftarrow -\pi} P(0,k_2)|u_{n,(0,-\pi)}\rangle \tag{B.2}$$

$$\equiv W_{\pi\leftarrow 0}(0) W_{0\leftarrow -\pi}(0) \tag{B.3}$$

Now, with C_2 symmetry we can write

$$C_2|u_{m(0,-\pi)}\rangle = |u_{n(0,pi)}\rangle \mathcal{B}_M^{nm}(C_2), \tag{B.4}$$

$$C_2|u_{m(0,0)}\rangle = |u_{n(0,0)}\rangle \mathcal{B}_\Gamma^{nm}(C_2), \tag{B.5}$$

where $\mathcal{B}_\Gamma^{mn}(C_2)$ and $\mathcal{B}_M^{mn}(C_2)$ is the matrix representations of C_2 at the Γ and M points, respectively. Inserting the identity operator C_2^2 in the expression for $W_{0\leftarrow -\pi}$ and using the invariance of the projectors, we find

$$W_{0\leftarrow -\pi}(0) = \mathcal{B}_\Gamma(C_2) W^\dagger_{\pi\leftarrow 0}(0) \mathcal{B}_M(C_2) \tag{B.6}$$

and so

$$W(0) = W_{\pi\leftarrow 0}(0)\mathcal{B}_\Gamma(C_2)W^\dagger_{\pi\leftarrow 0}(0)\mathcal{B}_M(C_2) \tag{B.7}$$

We can apply similar considerations to $W(\pi)$ to deduce

$$W(\pi) = W_{\pi\leftarrow 0}(\pi)\mathcal{B}_M(C_2)W^\dagger_{\pi\leftarrow 0}(\pi)\mathcal{B}_{M''}(C_2) \tag{B.8}$$

These expressions are particularly useful when the representation matrices $\mathcal{B}(C_2)$ are proportional to the identity matrix. This is always true in the case of one or two occupied bands for the irreps in Table 6.1. In this case, we have

$$W(0) = \text{sign}(\chi_\Gamma(C_2)\chi_M(C_2))\mathbb{I} \tag{B.9}$$

$$W(\pi) = \mathbb{I}, \tag{B.10}$$

where $\chi(C_2)$ is character of C_2 in each little group irrep, and $\mathbb{I}$ is the appropriately sized identity matrix. From this formula two observations used in the main text follow immediately:

1. For a single isolated band, the little group irreps at Γ and M have the same C_2 eigenvalues. This Wilson loop will be pinned to $\theta = 0$. This encompasses the case of the $(A_1 \uparrow G)_{1a}$ band representation observed in our fragile photonic crystal.

2. For two isolated bands with a single irrep at Γ and M, the Wilson loop at $k_1 = 0$ will be pinned to 0 if the irreps have the same C_2 eigenvalues, and will be pinned to π in the case that the irreps have opposite C_2 eigenvalues. In this latter case, the Wilson loop must wind so that $W(\pi)$ has $\theta_1 = \theta_2 = 0$. This is what occurs for the fragile topological bands.

C Appendix C: Detailed Numerical Methods

C.1 Phase Diagram

Here we describe the methods used to calculate the photonic phase diagram from the band dispersion of the structures and the Bloch-modes transformations. We first define a scan of 300 by 300 structures varying the values of the axes of the ellipses, d1 and d2, from $0.1a_0$ to $0.7a_0$. All ellipses are then placed at a distance of $a_0/3$ from the center of the triangular unit cell. Next, we use the program MIT Photonic-Bands (MPB) [73] to solve the eigenvalue problem and get the band structure and the eigenvectors at the high symmetry points (Γ, K and M). We then determine the symmetry of the Bloch functions using GTPack [88, 89], taking into account the little group of the high symmetry points. Once we have the irreps for the first three bands, the structures can be classified into trivial, fragile or OAL by symmetry. If the phase is fragile, for Γ the representations must be: A_1, E_2, and for K: A_1, E. If it is OAL, the irreps on Γ are the same but on K are inverted: E, A_1. Any other combination of irreps gives either a trivial or a gapless phase. To further refine this classification, we exclude symmetry-allowed band crossings at high symmetry points. This allows us to build the phase diagram in Fig. 5.4.

C.2 Wilson loop of Trivial and OAL phases

From the phase diagram, we picked one representative structure for each phase. Their band dispersion and real space structures are shown in Fig. 5.2.

To compute the Wilson loops, we use the discretized formula, following the algorithm of Marzari and Vanderbilt [87]. Enforcing boundary conditions to ensures that the Bloch wavefunctions are periodic in $\mathbf{k}$. Then, we numerically compute the overlap matrices along a line $k_2 \in [0, 2\pi]$ which gives the Wilson loop matrix $W(k_1)$. After the diagonalization, we take the phase of

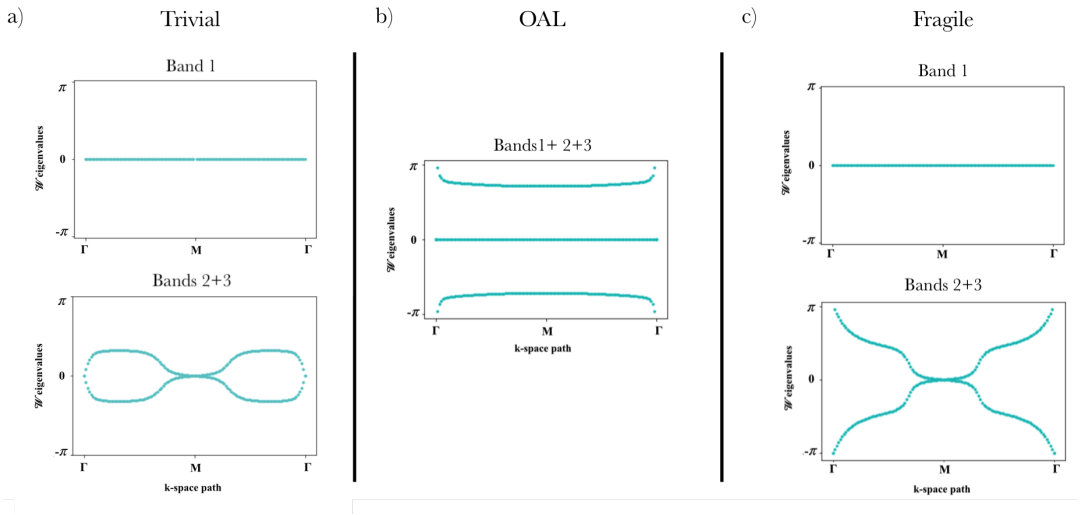

FIGURE C.1: Wilson loops for the trivial, fragile and OAL structures. (a) shows the Wilson loop for bands 1, bands 2 and 3, and bands 1,2 and 3 for the trivial structure. (b) shows the same loops for the fragile structure. (c) shows the Wilson loop for the three lowest bands in the obstructed atomic limit structure.

the eigenvalues in order to project the spectrum along k_1. In Fig. C.1 we show the Wilson loop spectra for the Trivial and OAL band structures which are induced from Wannier functions placed at $1a$ and $3c$ maximal Wyckoff positions, respectively.

Bibliography

[1] Michael Riordan and Lillian Hoddeson. *Crystal Fire: The Birth of the Information Age*. W. W. Norton, 1997.

[2] Arthur P. Ramirez and Brian Skinner. "Dawn of the topological age?" In: *Phys. Today* 73 (9 2020), p. 30. DOI: 10.1063/PT.3.4567.

[3] L. D. Landau and E. M. Lifshitz. *Statistical physics 3rd. Edition*. Oxford: Pergamon Press., 1980.

[4] L. D. Landau. In: *Zh. Eksp. Teor. Fiz.* 7 (1937), p. 19.

[5] John Cardy. *Scaling and renormalization in statistical physics, volume 5*. Cambridge university press, 1996.

[6] C.L. Kane. "Chapter 1 - Topological Band Theory and the $\mathbb{Z}_2$ Invariant". In: *Topological Insulators*. Ed. by Marcel Franz and Laurens Molenkamp. Vol. 6. Contemporary Concepts of Condensed Matter Science. Elsevier, 2013, pp. 3–34. DOI: 10.1016/B978-0-444-63314-9.00001-9.

[7] G. Dorda K. v. Klitzing and M. Pepper. "New method for high-accuracy determination of the fine-structure constant based on quantized hall resistance". In: *Phys. Rev. Lett.* 45 (1980), 494–497. DOI: 10.1103/PhysRevLett.45.494.

[8] D. J. Thouless et al. "Quantized Hall Conductance in a Two-Dimensional Periodic Potential". In: *Phys. Rev. Lett.* 49.405 (1982). DOI: 10.1103/PhysRevLett.49.405.

[9] J.D. Joannopoulos, Pierre R. Villeneuve, and Shanhui Fan. "Photonic crystals". In: *Solid State Commun.* 102.2-3 (Apr. 1997), pp. 165–173. DOI: 10.1016/s0038-1098(96)00716-8.

[10] A. B. Khanikaev and G. Shvets. "Two-dimensional topological photonics". In: *Nat. Photonics* 11 (12 2017), p. 763. DOI: 10.1038/s41566-017-0048-5.

[11] J. D. Joannopoulos. *Photonic crystals : molding the flow of light*. Princeton, N.J: Princeton University Press, 1995. ISBN: 978-0691037448.

[12] F.D.M. Haldane and S. Raghu. "Possible realization of directional optical waveguides in photonic crystals with broken time-reversal symmetry". In: *Phys. Rev. Lett.* 100.1 (2008), p. 013904. DOI: 10.1103/PhysRevLett.100.013904.

[13] M Zahid Hasan and Charles L Kane. "Colloquium: topological insulators". In: *Rev. Mod. Phys.* 82.4 (2010), p. 3045. DOI: 10.1103/RevModPhys.82.3045.

[14] Tomoki Ozawa et al. "Topological photonics". In: *Rev. Mod. Phys.* 91 (1 2019), p. 015006. DOI: 10.1103/RevModPhys.91.015006.

[15] F. D. M. Haldane. "Model for a Quantum Hall Effect without Landau Levels: Condensed-Matter Realization of the "Parity Anomaly"". In: *Phys. Rev. Lett.* 61 (18 1988), pp. 2015–2018. DOI: 10.1103/PhysRevLett.61.2015.

[16] C. L. Kane and E. J. Mele. "$\mathbb{Z}_2$ topological order and the quantum spin hall effect". In: *Phys. Rev. Lett.* 95 (2005), p. 146802. DOI: 10.1103/PhysRevLett.95.146802.

[17] C. L. Kane and E. J. Mele. "Quantum Spin Hall Effect in Graphene". In: *Phys. Rev. Lett.* 95 (22 2005), p. 226801. DOI: 10.1103/PhysRevLett.95.226801.

[18] Liang Fu. "Topological Crystalline Insulators". In: *Phys. Rev. Lett.* 106 (10 2011), p. 106802. DOI: 10.1103/PhysRevLett.106.106802.

[19] Kejie Fang, Zongfu Yu, and Shanhui Fan. "Realizing effective magnetic field for photons by controlling the phase of dynamic modulation". In: *Nat. Photonics* 6.11 (2012), p. 782. DOI: 10.1038/nphoton.2012.236.

[20] Mikael C Rechtsman et al. "Photonic Floquet topological insulators". In: *Nature* 496.7444 (2013), p. 196. DOI: 10.1038/nature12066.

[21] J. Fan A. Migdall M. Hafezi S. Mittal and J.M. Taylor. "Imaging topological edge states in silicon photonics". In: *Nat. Photonics* 7.1001 (2013). DOI: 10.1038/nphoton.2013.274.

[22] Hidekatsu Suzuura and Tsuneya Ando. "Crossover from Symplectic to Orthogonal Class in a Two-Dimensional Honeycomb Lattice". In: *Phys. Rev. Lett.* 89 (26 2002), p. 266603. DOI: 10.1103/PhysRevLett.89.266603.

[23] Kai Qian et al. "Topology of the valley-Chern effect". In: *Phys. Rev. B* 98 (15 2018), p. 155138. DOI: 10.1103/PhysRevB.98.155138.

[24] A. Kitaev. "Periodic table for topological insulators and superconductors". In: *AIP Conf. Proc.* Ed. by V. Lebedev and M. Feigel'Man.

Vol. 1134. American Institute of Physics Conference Series. May 2009, pp. 22–30. DOI: 10.1063/1.3149495.

[25] Ken Shiozaki, Masatoshi Sato, and Kiyonori Gomi. "Topological crystalline materials: General formulation, module structure, and wallpaper groups". In: *Phys. Rev. B* 95 (23 2017), p. 235425. DOI: 10.1103/PhysRevB.95.235425.

[26] Hoi Chun Po, Ashvin Vishwanath, and Haruki Watanabe. "Symmetry-based indicators of band topology in the 230 space groups". In: *Nat. Commun.* 8.1 (2017). DOI: 10.1038/s41467-017-00133-2.

[27] Barry Bradlyn et al. "Topological Quantum Chemistry". In: *Nature* 547 (2017), pp. 298–305. DOI: 10.1038/nature23268.

[28] Andreas P Schnyder et al. "Classification of topological insulators and superconductors in three spatial dimensions". In: *Phys. Rev. B* 78.19 (2008), p. 195125. DOI: 10.1103/PhysRevB.78.195125.

[29] Barry Bradlyn et al. "Disconnected elementary band representations, fragile topology, and Wilson loops as topological indices: An example on the triangular lattice". In: *Phys. Rev. B* 99.4 (2019), p. 045140. DOI: 10.1103/PhysRevLett.120.266401.

[30] W. P. Su, J. R. Schrieffer, and A. J. Heeger. "Solitons in Polyacetylene". In: *Phys. Rev. Lett.* 42 (25 1979), pp. 1698–1701. DOI: 10.1103/PhysRevLett.42.1698.

[31] W. P. Su, J. R. Schrieffer, and A. J. Heeger. "Soliton excitations in polyacetylene". In: *Phys. Rev. B* 22 (4 1980), pp. 2099–2111. DOI: 10.1103/PhysRevB.22.2099.

[32] A. J. Heeger et al. "Solitons in conducting polymers". In: *Rev. Mod. Phys.* 60 (3 1988), pp. 781–850. DOI: 10.1103/RevModPhys.60.781.

[33] Titus Neupert and Frank Schindler. "Topological Crystalline Insulators". In: *Topological Matter*. Springer International Publishing, 2018, pp. 31–61. DOI: 10.1007/978-3-319-76388-0_2.

[34] Srinivas Raghu and Frederick Duncan Michael Haldane. "Analogs of quantum-Hall-effect edge states in photonic crystals". In: *Phys. Rev. A* 78.3 (2008), p. 033834. DOI: 10.1103/PhysRevA.78.033834.

[35] Zheng Wang et al. "Reflection-Free One-Way Edge Modes in a Gyromagnetic Photonic Crystal". In: *Phys. Rev. Lett.* 100.1 (Jan. 2008), p. 013905. DOI: 10.1103/physrevlett.100.013905.

[36] Zheng Wang et al. "Observation of unidirectional backscattering-immune topological electromagnetic states". In: *Nature* 461 (2009), p. 772. DOI: 10.1038/nature08293.

[37] S. R. Pocock X. Xiao P. Arroyo Huidobro M. S. Rider S. J. Palmer and V. Giannini. "A perspective on topological nanophotonics: Current status and future challenges". In: *J. Appl. Phys.* 125 (12 2019), p. 120901. DOI: 10.1063/1.5086433.

[38] Mohammad Hafezi et al. "Robust optical delay lines with topological protection". In: *Nat. Phys.* 7.11 (2011), p. 907. DOI: 10.1038/nphys2063.

[39] Alexander B Khanikaev et al. "Photonic topological insulators". In: *Nat. Mat.* 12.3 (2013), p. 233. DOI: 10.1038/nmat3520.

[40] X. Ni S. H. Mousavi A. Z. Genack X. Cheng C. Jouvaud and A. B. Khanikaev. "Robust reconfigurable electromagnetic pathways within a photonic topological insulator". In: *Nat. Mat.* 15 (5 2016), 542–548. DOI: 10.1038/nmat4573.

[41] K. Y. Bliokh et al. "Spin–orbit interactions of light". In: *Nat. Photonics* 9.12 (2015), 796–808. DOI: 10.1038/nphoton.2015.201.

[42] Francisco J. Rodríguez-Fortuño et al. "Near-Field Interference for the Unidirectional Excitation of Electromagnetic Guided Modes". In: *Science* 340.6130 (2013), pp. 328–330. DOI: 10.1126/science.1233739.

[43] M. P. Makwana and R. V. Craster. "Designing multidirectional energy splitters and topological valley supernetworks". In: *Phys. Rev. B* 98 (23 2018), p. 235125. DOI: 10.1103/PhysRevB.98.235125.

[44] M. P. Makwana and R. V. Craster. "Geometrically navigating topological plate modes around gentle and sharp bends". In: *Phys. Rev. B* 98 (2018), p. 184105. DOI: 10.1103/PhysRevB.98.184105.

[45] Z. Fan M. Jung and G. Shvets. "Midinfrared plasmonic valleytronics in metagate-tuned graphene". In: *Phys. Rev. Lett.* 121 (2018), p. 086807. DOI: 10.1103/PhysRevLett.121.086807.

[46] J. Tian Y. Huang H. Xiang D. Han X. Wu Y. Meng and W. Wen. "Direct observation of valley-polarized topological edge states in designer surface plasmon crystals". In: *Nat. Commun.* 8 (1 2017), p. 1304. DOI: 10.1038/s41467-017-01515-2.

[47] H. Zhu Y. Wang J. W. Dong X. D. Chen and X. Zhang. "Valley photonic crystals for control of spin and topology". In: *Nat. Mat.* 16 (3 2017), 298–302. DOI: 10.1038/nmat4807.

[48] Long-Hua Wu and Xiao Hu. "Scheme for Achieving a Topological Photonic Crystal by Using Dielectric Material". In: *Phys. Rev. Lett.* 114 (22 2015), p. 223901. DOI: 10.1103/PhysRevLett.114.223901.

[49] C. Flower T. Cai H. Miyake W. DeGottardi M. Hafezi S. Barik A. Karasahin and E. Waks. "A topological quantum optics interface". In: *Science* 359 (6376 2018), 666–668. DOI: 10.1126/science.aaq0327.

[50] D. Leykam E. Melik-Gaykazyan D.-Y. Choi D. Smirnova S. Kruk and Y. Kivshar. "Third-harmonic generation in photonic topological metasurfaces". In: *Phys. Rev. Lett.* 123 (2019), p. 103901. DOI: 10.1103/PhysRevLett.123.103901.

[51] Siying Peng et al. "Probing the Band Structure of Topological Silicon Photonic Lattices in the Visible Spectrum". In: *Phys. Rev. Lett.* 122 (11 2019), p. 117401. DOI: 10.1103/PhysRevLett.122.117401.

[52] N. Kaina B. Orazbayev and R. Fleury. "Chiral waveguides for robust waveguiding at the deep subwavelength scale". In: *Phys. Rev. Applied* 10 (5 2018), p. 054069. DOI: 10.1103/PhysRevApplied.10.054069.

[53] T. Berthelot M. Fink-F. Lemoult S. Yves R. Fleury and G. Lerosey. "Crystalline metamaterials for topological properties at subwavelength scales". In: *Nat. Commun.* 8 (1 2017), p. 16023. DOI: 10.1038/ncomms16023.

[54] F. Lemoult M. Fink S. Yves R. Fleury and G. Lerosey. "Topological acoustic polaritons: robust sound manipulation at the subwavelength scale". In: *New J. Phys.* 19 (7 2017), p. 075003. DOI: 10.1088/1367-2630/aa66f8.

[55] C.-W. Chen R. Chaunsali and J. Yang. "Subwavelength and directional control of flexural waves in zone-folding induced topological plates". In: *Phys. Rev. B* 97 (2018), p. 054307. DOI: 10.1103/PhysRevB.97.054307.

[56] B. Orazbayev and R. Fleury. "Quantitative robustness analysis of topological edge modes in C_6 and valley-Hall metamaterial waveguides". In: *Nanophotonics B* 8 (8 2019), 1433 – 1441. DOI: 10.1515/nanoph-2019-0137.

[57] María Blanco de Paz et al. "Engineering fragile topology in photonic crystals: Topological quantum chemistry of light". In: *Phys. Rev. Research* 1 (3 2019), p. 032005. DOI: 10.1103/PhysRevResearch.1.032005.

[58] Jennifer Cano et al. "Topology of Disconnected Elementary Band Representations". In: *Phys. Rev. Lett.* 120 (26 2018), p. 266401. DOI: 10.1103/PhysRevLett.120.266401.

[59] Hoi Chun Po, Haruki Watanabe, and Ashvin Vishwanath. "Fragile topology and Wannier obstructions". In: *Phys. Rev. Lett.* 121.12 (2018), p. 126402. DOI: 10.1103/PhysRevLett.121.126402.

[60] Benjamin J. Wieder and B. Andrei Bernevig. *The Axion Insulator as a Pump of Fragile Topology*. 2018. arXiv: 1810.02373 [cond-mat.mes-hall].

[61] Junyeong Ahn and Bohm-Jung Yang. "Symmetry representation approach to topological invariants in $C_{2z}T$-symmetric systems". In: *Phys. Rev. B* 99 (23 2019), p. 235125. DOI: 10.1103/PhysRevB.99.235125.

[62] Adrien Bouhon, Annica M. Black-Schaffer, and Robert-Jan Slager. "Wilson loop approach to fragile topology of split elementary band representations and topological crystalline insulators with time-reversal symmetry". In: *Phys. Rev. B* 100 (19 2019), p. 195135. DOI: 10.1103/PhysRevB.100.195135.

[63] Juan L. Mañes. "Fragile phonon topology on the honeycomb lattice with time-reversal symmetry". In: *Phys. Rev. B* 102.2 (2020), p. 024307. DOI: 10.1103/PhysRevB.102.024307.

[64] Shang Liu, Ashvin Vishwanath, and Eslam Khalaf. "Shift Insulators: Rotation-Protected Two-Dimensional Topological Crystalline Insulators". In: *Phys. Rev. X* 9 (3 2019), p. 031003. DOI: 10.1103/PhysRevX.9.031003.

[65] Benjamin J. Wieder et al. "Strong and fragile topological Dirac semimetals with higher-order Fermi arcs". In: *Nat. Commun.* 11.1 (2020). DOI: 10.1038/s41467-020-14443-5.

[66] Liujun Zou et al. "Band structure of twisted bilayer graphene: Emergent symmetries, commensurate approximants, and Wannier obstructions". In: *Phys. Rev. B* 98 (8 2018), p. 085435. DOI: 10.1103/PhysRevB.98.085435.

[67] Zhida Song et al. "All Magic Angles in Twisted Bilayer Graphene are Topological". In: *Phys. Rev. Lett.* 123 (3 2019), p. 036401. DOI: 10.1103/PhysRevLett.123.036401.

[68] Tianle Wang, Nick Bultinck, and Michael P. Zaletel. "Flat-band topology of magic angle graphene on a transition metal dichalcogenide". In: *Phys. Rev. B* 102 (23 2020), p. 235146. DOI: 10.1103/PhysRevB.102.235146.

[69] Valerio Peri et al. "Experimental characterization of fragile topology in an acoustic metamaterial". In: *Science* 367.6479 (2020), pp. 797–800. DOI: 10.1126/science.aaz7654.

[70] John D. Joannopoulos et al. *Photonic Crystals: Molding the Flow of Light (Second Edition)*. 2nd. Princeton University Press, 2008.

[71] Kazuaki Sakoda. *Optical properties of photonic crystals*. Vol. 80. Springer Science & Business Media, 2004.

[72] John David Jackson. *Classical Electrodynamics-3rd ed.* ISBN: 978-3-527-41133-7. Wiley, 1998.

[73] Steven G Johnson and John D Joannopoulos. "Block-iterative frequency-domain methods for Maxwell's equations in a planewave basis". In: *Opt. Express* 8.3 (2001), pp. 173–190. DOI: 10.1364/OE.8.000173.

[74] David Vanderbilt. *Berry Phases in Electronic Structure Theory: Electric Polarization, Orbital Magnetization and Topological Insulators*. Cambridge University Press, 2018. DOI: 10.1017/9781316662205.

[75] Michael Victor Berry. "Quantal phase factors accompanying adiabatic changes". In: *Proc. R. Soc. Lond. A* 392.1802 (1984), pp. 45–57. DOI: 10.1098/rspa.1984.0023.

[76] S. Pancharatnam. "Generalized theory of interference, and its applications". In: *Proc. Indian Acad. Sci. - Sec. A* 44.5 (1956), pp. 247–262. DOI: 10.1007/BF03046050.

[77] J. Zak. "Berry's phase for energy bands in solids". In: *Phys. Rev. Lett.* 62 (1989), p. 2747. DOI: 10.1103/PhysRevLett.62.2747.

[78] Shiing-shen Chern. "Characteristic Classes of Hermitian Manifolds". In: *Ann. of Math.* 47.1 (1946), pp. 85–121. DOI: 10.2307/1969037.

[79] Motohiko Ezawa. "Topological Kirchhoff law and bulk-edge correspondence for valley Chern and spin-valley Chern numbers". In: *Phys. Rev. B* 88 (16 2013), p. 161406. DOI: 10.1103/PhysRevB.88.161406.

[80] C. J. Bradley and A. P. Cracknell. *The Mathematical Theory of Symmetry in Solids*. Oxford: Clarendon Press, 1972.

[81] L. Michel and J. Zak. "Elementary energy bands in crystals are connected". In: *Physics Reports* 341.1 (2001), pp. 377–395. DOI: 10.1016/S0370-1573(00)00093-4.

[82] Kurt Busch et al. "The photonic Wannier function approach to photonic crystal simulations: status and perspectives". In: *J. Mod. Opt.* 58.5-6 (2011), pp. 365–383. DOI: 10.1080/09500340.2010.526256.

[83] Bilbao Crystallogr. Server. *BANDREP: Band representations of the Double Space Groups*. http://www.cryst.ehu.es/cgi-bin/cryst/programs/bandrep.pl. 2017.

[84] Luis Elcoro et al. "Double crystallographic groups and their representations on the Bilbao Crystallographic Server". In: *J. Appl. Cryst.* 50.5 (2017), pp. 1457–1477. DOI: 10.1107/S1600576717011712.

[85] L. Novotny and B. Hecht. *Principles of nano-optics*. Cambridge University Press, 2012.

[86] Acadia University. *Point Group Flowchart*. http://www.acadiau.ca/~bellis/resources/symmetrygrouptheory/flowchart.html.

[87] Nicola Marzari and David Vanderbilt. "Maximally localized generalized Wannier functions for composite energy bands". In: *Phys. Rev. B* 56.20 (1997), p. 12847. DOI: 10.1103/PhysRevB.56.12847.

[88] R. Matthias Geilhufe and Wolfram Hergert. "GTPack: A Mathematica Group Theory Package for Application in Solid-State Physics and Photonics". In: *Front. Phys.* 6 (2018), p. 86. DOI: 10.3389/fphy.2018.00086.

[89] Wolfram Hergert and R. Matthias Geilhufe. *Group Theory in Solid State Physics and Photonics: Problem Solving with Mathematica*. ISBN: 978-3-527-41133-7. Wiley-VCH, 2018.

[90] Scott A. Skirlo et al. "Experimental Observation of Large Chern Numbers in Photonic Crystals". In: *Phys. Rev. Lett.* 115 (25 2015), p. 253901. DOI: 10.1103/PhysRevLett.115.253901.

[91] Tzuhsuan Ma and Gennady Shvets. "All-Si valley-Hall photonic topological insulator". In: *New J. Phys.* 18.2 (Feb. 2016), p. 025012. DOI: 10.1088/1367-2630/18/2/025012.

[92] Long-Hua Wu and Xiao Hu. "Topological Properties of Electrons in Honeycomb Lattice with Detuned Hopping Energy". In: *Sci. Rep.* 6.1 (Apr. 2016). DOI: 10.1038/srep24347.

[93] M. I. Aroyo, ed. *International Tables for Crystallography*. Vol. A. International Union of Crystallography, 2016. DOI: 10.1107/97809553602060000114.

[94] M. I. Aroyo et al. "Crystallography online: Bilbao Crystallographic Server". In: *Bulg. Chem. Commun.* 43(2) (2011), p. 183.

[95] M. I. Aroyo et al. "Bilbao Crystallographic Server: I. Databases and crystallographic computing programs". In: *Zeitschrift für Kristallographie - Crystalline Materials* 221.1 (2006), pp. 15–27. DOI: 10.1524/zkri.2006.221.1.15.

[96] M. I. Aroyo et al. "Bilbao Crystallographic Server. II. Representations of crystallographic point groups and space groups". In: *Acta Crystallographica Section A* 62.2 (2006), pp. 115–128. DOI: 10.1107/S0108767305040286.

[97] J. Zak. "Band representations of space groups". In: *Phys. Rev. B* 26 (1982), p. 3010. DOI: 10.1103/PhysRevB.26.3010.

[98] R. A. Evarestov and V. P. Smirnov. *Site Symmetry in Crystals*. Springer, 1997.

[99] Haruki Watanabe and Ling Lu. "Space Group Theory of Photonic Bands". In: *Phys. Rev. Lett.* 121 (26 2018), p. 263903. DOI: 10.1103/PhysRevLett.121.263903.

[100] A. Alexandradinata et al. "Spin-Orbit-Free Topological Insulators without Time-Reversal Symmetry". In: *Phys. Rev. Lett.* 113 (11 2014), p. 116403. DOI: 10.1103/PhysRevLett.113.116403.

[101] A. Alexandradinata, Xi Dai, and B. Andrei Bernevig. "Wilson-loop characterization of inversion-symmetric topological insulators". In: *Phys. Rev. B* 89 (15 2014), p. 155114. DOI: 10.1103/PhysRevB.89.155114.

[102] Matthew Proctor et al. "Robustness of topological corner modes in photonic crystals". In: *Phys. Rev. Research* 2 (4 2020), p. 042038. DOI: 10.1103/PhysRevResearch.2.042038.